Chair of Geology and Economic Geology

Master's Thesis

Trace Element Composition of Sphalerite from the Raibl Pb-Zn mine
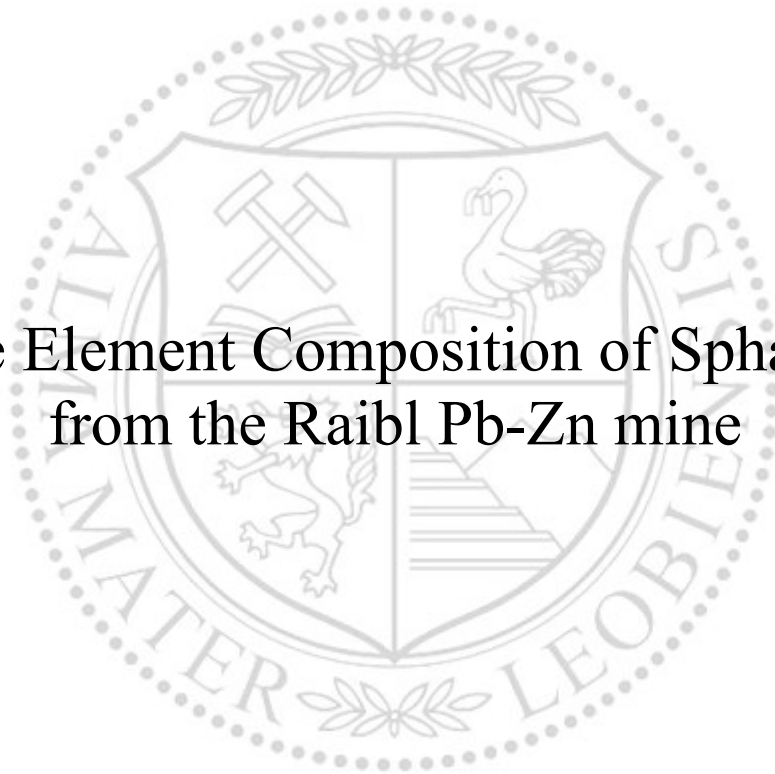
Veronika Gartner, BSc

February 2023

Vorgelegt von :

Veronika Gartner, BSc

01435212

Betreuer:

Univ.-Prof. Mag.rer.nat. Dr.mont Frank Melcher

Acknowledgments

Abstract

Raibl (Cave del Predil) in the North-East of Italy is a low-temperature carbonate-hosted lead-zinc deposit in the Southern Alps. The lead-zinc mineralization consisting mainly of sphalerite, galena and pyrite is hosted in the Ladinian Upper Schlern Dolomite. Since the 19th century sphalerite from Raibl is known to contain significant amounts of trace elements. Sphalerite from Raibl was investigated by microscopy, photography under UV-light, Raman spectroscopy, SEM and LA-ICP-MS. The results provide new data that link textural and color varieties of sphalerites to trace element compositions. For the first time a tubular ore sample was investigated by LA-ICP-MS.

Significantly high contents of iron (median = 267 $\mu g/g$, max = 6973$\mu g/g$), germanium (median = 168 $\mu g/g$; maximum = 1524 $\mu g/g$), arsenic (median = 779 $\mu g/g$; maximum = 10618 $\mu g/g$), cadmium (median = 1593 $\mu g/g$; maximum = 7640 $\mu g/g$), thallium (median = 132 $\mu g/g$; maximum = 2324 $\mu g/g$) and lead (median = 2477 $\mu g/g$; maximum = 39955 $\mu g/g$) were found in sphalerite from Raibl. Arsenic, thallium, germanium, lead, manganese and iron exhibit significant positive correlation. Cadmium is negatively correlated to arsenic, thallium, germanium, lead and manganese. Additionally, some sphalerite samples show notably elevated contents of copper, gallium, tin, antimony and mercury. The sphalerite exhibits insignificant amounts of vanadium, chromium, manganese, cobalt, nickel, selenium, molybdenum, silver, indium, tellurium, gold and bismuth.

Sphalerite from Raibl can be classified according to color (brown, red, grey, yellow and green sphalerite) or texture (colloform, agglomerated (type A and B), tubular, fern and layered sphalerite). Tubular sphalerite is part of tubes formed by primary ore. Such samples have also been found in other Alpine-type lead-zinc deposits. Fern sphalerite consists of clusters of grains resembling leaves. Based on texture, color and chemical composition, colloform, agglomerated sphalerite type B, fern and tubular sphalerite can be grouped together, whereas layered sphalerite and agglomerated sphalerite type A should be considered separately. Colloform sphalerite and agglomerated sphalerite type B show varying trace element contents depending on place of origin in the mine. Samples from the north are richer in germanium, thallium and arsenic, while samples from the south are richer in cadmium.

Considering petrography, chemical composition and temperature calculations, similar formation processes for colloform, agglomerated type B, fern and tubular sphalerite are postulated. Although several hypotheses have been proposed, the formation of tubular ore remains unknown. Fern sphalerite is an altered variation of colloform sphalerite. In contrast, layered sphalerite and agglomerated sphalerite type A likely were formed by different processes and are not linked to the other textural varieties of sphalerite.

The GGIMFis geothermometer yields an overall formation temperature of sphalerite of 88 ± 6 °C. This temperature fits well with the classification of Raibl as a low-temperature carbonate hosted Alpine type lead-zinc deposit. Layered sphalerite shows a lower formation temperature compared to the other textural varieties of sphalerite.

Raibl (Cave del Predil) im Nordosten Italiens ist eine karbonatische Niedrigtemperatur-Blei-Zink-Lagerstätte in den Südalpen. Die Blei-Zink-Mineralisation, welche hauptsächlich aus Sphalerit, Galenit und Pyrit besteht, befindet sich im ladinischen oberen Schlern Dolomit. Es ist seit dem neunzehnten Jahrhundert bekannt, dass Sphalerit aus Raibl signifikante Spurenelementgehalte aufweist. Sphalerit aus Raibl wurde mit Hilfe von Mikroskopie, Photographie unter UV-Licht, Raman Spektroskopie, REM und LA-ICP-MS untersucht. Die Ergebnisse liefern neue Daten, welche texturelle und farbliche Varietäten des Sphalerits mit Spurenelementzusammensetzungen kombinieren. Zum ersten Mal wurde eine Röhrenerzprobe mit LA-ICP-MS untersucht.

Signifikant hohe Gehalte an Eisen (Median = 267 $\mu g/g$; Maximum = 6973 $\mu g/g$), Germanium (Median = 168 $\mu g/g$; Maximum = 1524 $\mu g/g$), Arsen (Median = 779 $\mu g/g$; Maximum = 10618 $\mu g/g$), Kadmium (Median = 1593 $\mu g/g$; Maximum = 7640 $\mu g/g$), Thallium (Median = 132 $\mu g/g$; Maximum = 2324 $\mu g/g$) und Blei (Median = 2477 $\mu g/g$; Maximum = 39955 $\mu g/g$) wurden im Sphalerit gefunden. Arsen, Thallium, Germanium, Blei, Mangan und Eisen zeigen eine positive Korrelation. Kadmium korreliert negativ zu Arsen, Thallium, Germanium, Blei und Mangan. Zusätzlich wurden in manchen Sphaleritproben bedeutende Gehalte an Kupfer, Gallium, Zinn, Antimon und Quecksilber gefunden. Sphalerit aus Raibl enthält nur unbedeutende Mengen an Vanadium, Chrom, Cobalt, Nickel, Selen, Molybdän, Silber, Indium, Tellur, Gold und Bismut.

Eine Einteilung des Sphalerits kann nach Farben (braun, rot, grau, gelb und grün) oder nach Textur (kolloformer, agglomerierter (typ A und B) und lagiger Sphalerit, sowie Sphalerit als Teil von Farnerz und Röhrenerz) erfolgen. Röhrenerz zeigt sich als Röhren bestehend aus verschiedenen primären Erzen. Proben dieser Art sind auch in anderen Blei-Zink-Lagerstätten des Alpinen Typs gefunden worden. Sphalerit als Teil von Farnerz formt Ansammlungen von Körnern, welche Blättern ähneln. Basierend auf Textur, Farbe und chemischer Zusammensetzung können kolloforme, agglomerierter Sphalerite vom Typ B und Sphalerite aus dem Farn-und Röhrenerz zusammengefasst werden. Hingegen sollten lagige Sphalerite und agglomerierter Sphalerit vom Typ A gesondert bestrachtet werden. Kolloformer Sphalerit und agglomerierter Sphalerit vom Typ B zeigen auch eine Variation des Spurenelementgehalts abhängig vom Herkunftsort im Abbau. Proben aus dem Norden sind reicher an Germanium, Thallium und Arsen, während Proben aus dem Süden einen höheren Gehalt an Kadmium aufweisen.

Basierend auf Petrographie, chemischer Zusammensetzung und Temperaturberechnung werden ähnliche Bildungsprozesse für kolloforme Sphalerite, disseminierte Sphalerite vom Typ B und Sphalerite aus Farn-und Röhrenerzen vorgeschlagen. Obwohl mehrere Hypothesen vorgebracht wurden, bleibt die Bildung des Röhrenerzs ungeklärt. Farnerz ist als eine alterierte Variation des kolloformen Sphalerits anzusehen. Im Gegensatz dazu, bildeten sich lagige Sphalerite und agglomerierter Sphalerit vom Typ A wahrscheinlich durch andere Prozesse und sind nicht an andere texturelle Varietäten des Sphalerits gebunden.

Das GGIMFis Geothermometer ergibt für Sphalerit eine allgemeine Bildungstemperatur von 88±6 °C. Dies passt zur Klassifikation der Lagerstätte als karbonatische Niedrigtemperatur-Blei-Zink-Lagerstätte vom Alpinen Type. Lagiger Sphalerit zeigt eine niedrigere Bildungstemperatur als andere texturelle Varietäten des Sphalerits.

Contents

1. Introduction

Zinc-sulfide (ZnS) occurs as either cubic sphalerite, hexagonal wurtzite or trigonal matraite (Cook et al. 2009). Sphalerite is the most common of the three and serves as an economically important zinc source (Cook et al. 2009). Sphalerite has a structure similar to diamond, alternating zinc and sulfur (Bragg 1913). The mineral exhibits a face-centered cubic lattice with tetrahedrally-coordinated zinc and sulfur ions (Cook et al. 2009). It can be found in a multitude of different rocks (Fleet 2006).

Sphalerite may commonly contain other elements apart from zinc and sulfur, such as manganese, iron, cobalt, nickel, gallium, germanium, arsenic, indium, cadmium, mercury, thallium, bismuth (Stoiber 1940). The trace element composition of sphalerite is interesting for scientific purposes, as sphalerite is a refractory mineral, which preserves texture and compositions of higher formation temperatures (Craig et al. 1981). Incorporation of trace elements varies depending on mineralization temperature (Höll et al. 2007; Frenzel et al. 2016), deposit type (Frenzel et al. 2016; Ye et al. 2011) and gangue minerals surrounding the sphalerite (Pfaff et al. 2011). High indium contents have been linked to magmatically-driven hydrothermal systems, while germanium, gallium, thallium, antimony, mercury and arsenic are thought to be enriched in deposits of low-temperature and unrelated to any magmatic source (Belissont et al. 2014; Bauer et al. 2019). Molybdenum has been found in sphalerite from mesothermal deposits, manganese in high-temperature sphalerite. Tin and cadmium are not enriched in low-temperature-deposits (Stoiber 1940). Differences in composition of sphalerites and temperature data obtained by fluid inclusion analysis can be used for the calculation of a geothermometer (Frenzel et al. 2016).

Besides furthering scientific research, the trace elements of sphalerite can also be economically interesting. Indium, germanium and cadmium are regarded as by-products of the zinc production, if the concentration of these elements in sphalerite is high enough to be considered of economic interest (Gunn 2014). Germanium, especially, is needed for various application in technology (e.g. infrared systems, fiber optics, polymer catalysts, photovoltaic systems and electronic devices) and its demand is suspected to increase in the future (Licht et al. 2015; summarized by Patel and Karamalidis 2021 and references therein). The European Union considers germanium, gallium and indium critical elements, since they are economically important, but show a high risk of disruption of the supply (European Commission 2020). Trace elements occurring in sphalerite have to be observed, even if they do not serve economic purposes. In some cases they are hazardous towards the environment, for example cadmium-rich or mercury-rich sphalerites can cause significant pollution (Schwartz 2000; Álvarez-Ayuso et al. 2013; Bao et al. 2022). Furthermore, they can influence mineral processing. It is known, that iron ions negatively impact the result of sphalerite flotation (Boulton et al. 2005).

The lead-zinc deposit Raibl (Cave del Predil) is situated in the Seebachtal (Val del Rio del Lago). This valley is part of the northern Julian Alps in the province of Friuli Venezia

Giulia in the northeast of Italy. The deposit is located south of the Austrian-Italian border, 9 kilometers south of Tarvis (Fellet et al. 2011; Jicha 1951; Frangipani 2013; Göbl 1903). It has often been compared to other famous lead-zinc deposits (e.g. Bleiberg in Austria, Mežica in Slovenia).

About 150 years ago, speculations arose that varying chemical compositions of sphalerite from Raibl could influence its color (Posepny 1873). Although, trace element analyses of sphalerite from the Raibl lead-zinc deposit have been conducted already (e.g. Melcher and Onuk 2019; Henjes-Kunst 2014), this work presents additional, more extensive investigation. For the first time quantitative trace element data is linked to differently colored sphalerite and varying textures in an attempt to find distinctive trends to differentiate ore types from the Raibl mine. This will be achieved by detailed microscopic descriptions, followed by trace element measurements by laser ablation inductively coupled plasma mass spectrometry (LA-ICP-MS). Furthermore, the Raibl trace element data will be compared to similar carbonate-hosted lead-zinc deposits.

2. Background and literature overview

2.1. Trace element substitution in zinc-sulfide (ZnS)

Trace elements can be incorporated in zinc-sulfide either by substitution of ions within the crystal lattice or by nano-inclusions enclosed by the crystal (Pfaff et al. 2011). Substituted ions and nano- or micro-scale inclusions can be difficult to distinguish by conventional analytical methods such as SEM, EPMA and LA-ICP-MS (Cook et al. 2009). For trivalent and tetravalent ions the general substitution formula $(x+2y)M(I)+yM(II)+xM(III)+yM(IV) \rightleftharpoons (4-4y-2x)Zn(II)$ has been proposed for sphalerite, where M(I) = Ag, Cu; M(II) = Cu, Fe, Cd, Hg, Zn; M(III) = In, Ga, Tl, Fe; M(IV) = Ge, Sn, Mo, W and x, y = atomic proportions of M^{3+} and M^{4+}) (Johan 1988). It is assumed that M^{2+}-ions generally are placed at the zinc-site in the crystal lattice and are not present interstitially (Wright 2009).

Substitution mechanisms in sphalerite include direct substitution, coupled substitution and more complex substitution. Direct substitution mechanism can be described as $2Zn^{2+} \leftrightarrow (Fe^{2+}, Cd^{2+})$ (Belissont et al. 2014).The sulfur within sphalerite can be substituted by selenium or arsenic (Cook et al. 2009). For coupled substitutions several mechanisms have been proposed, such as $2Zn^{2+} \leftrightarrow Cu^+ + In^{3+}; 2Zn^{2+} \leftrightarrow Cu^+ + Sb^{3+}; 3Zn^{2+} \leftrightarrow Ge^{4+} + 2Ag^+; 2Zn^{2+} \leftrightarrow Cu^+ + Ga^{3+}; Sn^{4+} + 2Cu^+ \leftrightarrow 3Zn^{2+}; 3Zn^{2+} \leftrightarrow 2Cu^+ + Ge^{4+}$ and $2Zn^{2+} \leftrightarrow Ag^+ + Sb^{3+}$ (Cook et al. 2012; Belissont et al. 2014; Pring et al. 2020; Schirmer et al. 2020; C. Wei et al. 2019; Carrillo-Rosúa et al. 2008). More complex substitution mechanisms reported include $Sb^{3+} + Cu^+ + Cu^{2+} \leftrightarrow 3Zn^{2+}; 2Ge^{2+} + Ga^{3+} + 2Cu^{2+} + Cu^+ \leftrightarrow 6Zn^{2+}; 3Zn^{2+} \leftrightarrow In^{3+} + Sn^{3+} + (vacancy); Zn^{2+} \leftrightarrow Ge^{4+} + (vacancy); 2(Ag, Cu)^+ + Sn^{4+} \leftrightarrow 3Zn^{2+}$ (Carrillo-Rosúa et al. 2008; Belissont et al. 2014; Cook et al. 2015; Pring et al. 2020). Trace element composition can vary within a crystal and can be described in compositional zoning, bands or other patterns (Di Benedetto et al. 2005; Belissont et al. 2014).

Trace element content of sphalerite has been connected to different properties of ore formation. Incorporation of germanium depends on the iron content of the sphalerite and the general sulfur supply (Moh and Jager 1979). The iron content of sphalerite is reliant on lithostatic pressure and sulfur fugacity (Fleet 2006; Wright and Gale 2010). A temperature dependency has also been suggested (Lange et al. 1985; Cook 1996; Frenzel et al. 2016). Germanium content also seems to be dependent on temperature (Frenzel et al. 2016). It has been argued that the gallium-germanium-ratio is linked to the temperature of the formation fluid (Möller 1987). Copper substitution is associated with the iron-content of the sphalerite and depends on the sulfur fugacity and on the temperature (Kojima and Sugaki 1984). The incorporation of manganese and cadmium is dependent on temperature and pressure (Kullerud 1953). Trace elements in a sphalerite can be remobilized due to recrystallization caused by deformation (Cugerone et al. 2020).

Varying trace element compositions of sphalerite can also have practical applications in research. They can be utilized as a tool to discriminate ores of different deposit types (Liu et al. 2022; Hu et al. 2021).

2.1.1. Trace elements and color

Pure zinc-sulfide is colorless. However, this case is rare in nature and most sphalerite crystals show some variation in color, due to natural zinc-sulfide almost always containing trace elements to varying degrees (Kullerud 1953). Throughout literature, linking different trace element compositions to varying colors has been proposed several times. The following paragraph shows some of the attempts undertaken.

Darker and lighter sphalerite has been related to differing iron contents (Hill et al. 1985; Cugerone et al. 2018; Carrillo-Rosúa et al. 2008). Iron content of sphalerite also influences color, as it turns colorless sphalerite yellow, brown or even black (Kullerud 1953). Darker and lighter colored sphalerite has also been connected to varying germanium content in the crystal lattice (Cugerone et al. 2020). Sphalerite can change its color from white to white-yellow due to increasing cadmium content (Kubo et al. 1992). Green colored sphalerites get their color from cobalt ions substituting for zinc ions in the lattice (Rager et al. 1996). The trace element combinations of antimony and copper, as well as tin and copper, produce red color, if the sphalerite is iron-poor (Carrillo-Rosúa et al. 2008).

However, not all color variants can be explained satisfyingly and the ones mentioned above have also been questioned. Therefore a predominant cause for specific coloration of sphalerite crystals is still enigmatic.

Besides color seen in normal light, varying trace element composition can also create different colors of photoluminescence (e.g. by excitation of UV-light) or cathodoluminescence (Goni and Rémond 1969; Kuhlemann and Zeeh 1995).

2.2. Carbonate hosted lead-zinc deposits

Carbonate hosted lead-zinc deposits such as Mississippi Valley type deposits and Alpine type deposits are economically important sources for zinc, lead, barite and fluorite, but also trace elements such as germanium (Höll et al. 2007).

2.2.1. Mississippi Valley Type (MVT) ore deposits

Mississippi Valley Type deposits are epigenetic, sulfidic ore deposits which are hosted by carbonate host rocks (Paradis et al. 2007a). They are seen as discordant when considering the deposit alone, but are considered stratabound concerning the whole metallogenic district (Sangster 1996). This deposit type is often hosted in dolomite, while limestone or sandstone are less common (Anderson and Macqueen 1982; Leach and Sangster 1993). The host rock has not experienced metamorphism (Anderson and Macqueen 1982).

MVT deposits are controlled by extensional faults and associated fractures (Leach et al. 2010b; Leach et al. 2010a). This deposit type has been linked to large contractional tectonic events (Leach et al. 2001) and is not linked to igneous activity (Leach and Sangster 1993). MVT deposits are located in passive-margin tectonic settings (Leach et al. 2010a). The deposits are found at shallow depths at the edges of basins, in platform carbonate rocks near foredeeps or in foreland thrust belts (Leach and Sangster 1993). MVT deposits are found in areas of weak deformation (brittle fracture, uplift of domes, subsidence of the basin) (Sangster 1996).

MVT can show widespread distribution in an area of hundreds of square kilometers, defining ore districts (Leach et al. 1995; Leach and Taylor 2009). Most MVT deposits are of Devonian to Carboniferous age (Leach et al. 2010a). The most important periods of ore formation is Devonian-late Permian and Cretaceous-Tertiary (Leach et al. 2001).

The mineralogical composition is simple, as MVT deposits mostly consist of sphalerite, galena, pyrite, marcasite, dolomite, calcite and quartz (Leach and Sangster 1993; Sangster 1996). Fluorite and/or barite can be found as accessory minerals (Sangster 1996). Additionally celestine, gypsum, anhydrite, native sulfur and pyrrhotite have been described (Paradis et al. 2007b). Chalcopyrite, bornite and other copper-sulfides, as well as a complex suite of sulfide minerals have also been reported from some deposits (Leach et al. 1995). Various secondary minerals have been described, which can be summarized as typical calamine assemblages (Leach et al. 1995). Mineral abundances vary within in one deposit, however it can be stated, that most MVT deposits are zinc-rich compared to lead (Sangster 1996). The average zinc to lead ratio is 10:1 (Leach and Taylor 2009). Several sulfide mineral textures are possible in MVT deposits (Leach and Sangster 1993). The ore can replace the host rock or can be part of a breccia (dissolution collapse breccias, fault and sedimentary breccias) (Leach et al. 2010b). Ore can also occur as a filling of primary pore space (e.g. fossil molds) (Sangster 1996). Other textures described include fine-grained banded ore, colloform and dendritic ores, snow-on-the-roof textures, pseudo-breccia, zebra textures, rhythmites and speleothem-like sulfides (Leach et al. 2010b).

MVT deposits do not show uniform trace element compositions. Various trace elements have been found, e.g. copper, cadmium, germanium, barite, fluorine, nickel, cobalt and

silver (Leach et al. 1995; Sangster 1996). Anderson and Macqueen (1982) states that galena in MVT deposits contains low amounts in silver and sphalerite is low in iron. Fluid inclusions are commonly filled with aqueous, dense, saline fluids, in which total dissolved salts vary from 10 to 30wt.%. Some deposits also contain fluid inclusions consisting of petroleum and/or gas (Sangster 1996). Kerogen and bitumen within host rocks have also been described (Anderson and Macqueen 1982). Within deposits, alterations such as dolomitization, brecciation, host-rock dissolution/recrystalliation and dissolution/crystallization of feldspar and clay have been reported (Leach and Sangster 1993; Sangster 1996).

Ore formation can be explained by basinal brines migrating from the basin to the edge of the basin (Sverjensky 1986). The ore fluids were dense, basinal brines, which were derived from evaporated seawater (Leach and Sangster 1993; Leach et al. 2010a). Several causes of ore precipitation have been proposed (e.g. mixing of fluids, reduction of sulfates, changes of ph) (Sangster 1996). Crustal sources for metals and sulfur are assumed. The depositional temperatures were low (75 to 200°C), but higher than expected by local thermal gradients (Leach and Sangster 1993).

MVT deposits can be found worldwide (Paradis et al. 2007a). Several subtypes of MVT deposits have been described (e.g. Viburnum Trend-, Alpine-, Silesia-, Irish-, Appalachian-, and Reocin-type) (Paradis et al. 2007a; Leach et al. 2010b). MVT deposits can be grouped with other deposit types under the name sediment-hosted base-metal deposits (Paradis et al. 2007a). It is assumed, that approximately 25% of the world's lead and zinc resources are found in MVT deposits (Paradis et al. 2007a). This deposit type is also a source for gallium, germanium, barite and fluorite, as well as in some cases silver, copper, cadmium and indium (Paradis 2015; Leach and Taylor 2009).

2.2.2. Alpine-type (APT) / Bleiberg type lead-zinc ore deposits

More than 200 lead-zinc occurences or deposits were recorded within Triassic Alpine carbonates (Höll et al. 2007; Schroll 1996). They are found in Carnian carbonates and shales, as well as Anisian carbonates and Upper Ladinian sequences (Höll et al. 2007; Schroll 2005; Brigo et al. 1977). Ore structures and paleogeographic patterns can be correlated (Brigo et al. 1977). The economically most interesting ore deposits are located near the Periadriatic Lineament (Schroll 1996).

APT deposits consist of sphalerite and galena. The lead to zinc ratio of this deposit type varies between 1 and 1/20 (Schroll 2005). Additionally iron sulfides (Schroll 2005; Schroll 1996), as well as other sulfide minerals in minor amounts have been described (Schroll 1996). In Mežica wulfenite ore of economic quantities was discovered and mined (Schroll 1996). The gangue minerals consist of calcite, dolomite, fluorite, barite and quartz in varying proportions (Schroll 1996). Textures and geochemical properties differ in deposits found in Carnian and Anisian host rocks (Schroll 2005). The mineralization is stratabound, in some parts stratiform (Brigo et al. 1977). Both stratiform mineralization and discordant mineralization have been described (Schroll 1996).

Geochemically, the APT deposits were characterized by sulfur isotope compositions, lead isotope compositions and trace elements. The Alpine type is characterized by isotopically

light sulfide sulfur, probably produced via bacteriogenic reduction (Schroll and Rantitsch 2005). Relics of bacteria were found in ore samples of this deposit type (Kucha et al. 2001; Kucha et al. 2010). An additional source for sulfur may be epigenetic hydrothermal fluids (Schroll and Rantitsch 2005) or thermal sulfate reduction (Schroll 2005). A homogenous lead isotope composition is distinctive for this deposit type (Köppel and Schroll 1985; Schroll 2005). It is suspected that the source of the lead were old lower crustal rocks (Köppel 1983). It is argued that metals and sulfur were transported in different fluids (Henjes-Kunst 2014).

The Bleiberg Type is characterized by its deficiency in the elements of the iron group (Cerny 1989b; Schroll 1983). It is extremely poor in silver, copper and chalcophile elements such as mercury, indium, tin, antimony, bismuth. In contrast this deposit type is enriched in cadmium, arsenic, germanium and thallium (Schroll 1983; Schroll 2005; Brigo et al. 1977). The ratio of gallium to germanium is below 1 (Schroll 2005). The ratio of arsenic to thallium is at approximately 3 (Schroll 1996). High F-and Ba contents in the deposits are reported (Cerny 1989b). Sphalerites are poor in iron (Schroll 2005). Galena shows higher silver content than sphalerite, but is considered silver-poor, it can also contain arsenic, thallium and antimony as trace elements (Schroll 1996; Brigo et al. 1977).

APT ores were formed by saline fluids (Schroll 2005). Ore-forming fluids are considered non-magmatic, based on research conducted in Mežica (Dolenec et al. 1983). The ores were deposited at relatively low temperatures (Schroll 1983). For the Bleiberg type the temperature has been given as not higher than 200°C, the calculations were based on germanium-gallium ratios of sphalerites (Schroll 1996). Mineralization is facies-controlled (Cerny 1989b).

APT is linked to basin developments and geological events. APT deposits are influenced by their thermal history due to burial and Alpine orogeny (Schroll 2005). A link to large extensional events has been suggested (Muchez et al. 2005). APT deposits are sometimes compared to Irish type deposits (Schroll 2005). Some authors argue that APT deposits should be considered a variation of the MVT deposits (Zeeh et al. 1998). Different properties of MVT and APT deposits are summarized in table 2.1.

MVT deposits	APT deposits
low temperature mineralization	low temperature mineralization
carbonate host rock	carbonate host rock
Sphalerite, galena and iron-sulfides	sphalerite, galena and iron-sulfides
Higher contents of Cu, Co, Ni, Ag	Poor in Cu, Co, Ni, Ag
Contain F and Ba	Contain F and Ba
Compressional tectonics	Extensional tectonics
Epigenetic	Epigenetic and Syngenetic

Table 2.1.: Comparison of MVT and APT deposits; compiled after Leach and Sangster (1993), Leach et al. (1995), Sangster (1996), Leach et al. (2001), Paradis et al. (2007a), Höll et al. (2007), Schroll (2005) Cerny (1989b), Schroll (1983), Brigo et al. (1977), Muchez et al. (2005)

2.2.3. Classification of the Raibl deposit

Raibl is part of a middle Triassic metallogenetic province, which is located in the south-eastern part of the Alps (Cerny 1989a; Brigo et al. 1977).The genesis of the deposit is still debated. Raibl is considered either of epigenetic origin (Cerny 1989a) or both epi- and syngenetic (Brigo and Omenetto 1978), since a mineralization at the contact of the Dolomia Metallifera and the Raibl Group was considered syngenetic (Brigo and Omenetto 1978; Schulz 1964). It has been suggested that there is no causal relationship between the formation of the carbonate host rock and the mineralization in Raibl (Hein and Schneider 1983), which could be an indicator for an epigenetic origin. It is ascertained, that after the genesis, the deposit experienced brittle deformation (Brigo and Omenetto 1978). The Raibl deposit is not linked to a volcanic center and there are no connections to Triassic magmatism (Brusca et al. 1981).

The classification of the Raibl deposit is not without controversy. Some authors consider it an MVT-Deposit (Jicha 1951; Zeeh and Bechstädt 1994), others attribute it to the Alpine type/Bleiberg Type (Schroll and Prochaska 2004; Cerny 1989b). Raibl was already compared with Bleiberg in 1873 (Posepny 1873) and later also to Salafossa and Mežica (Omenetto 1980; Tornquist 1931). Bleiberg, Mežica, Raibl have been used to define the APT deposit (e.g Schroll 1996).

3. Geological setting

3.1. Regional geology

The Julian Alps are part of the Southern Alps (Froitzheim et al. 2008), which belong to the Alpine-Balkan-Carpathian-Dinaridic orogenic system (Schmid et al. 2008). Raibl is situated south of the Neogene dextral transpressive Gail and Fella-Sava lines; the first one is part of the Insubric fault system (Periadriatic Lineament) (Doglioni 1988). The Periadriatic lineament is considered the northern and western border of the Southern Alps (Schmid et al. 1989). In the south the Po and Venetian plains limit the Southern Alps (Castellarin et al. 1992). The Southern Alps are considered a south-vergent thrust and fold belt (Castellarin et al. 1992). These parts of the Alps are nearly devoid of any metamorphic overprint (Froitzheim et al. 2008). A simplified map showing the position of the Raibl deposit within the Southern Alps can be seen in figure 3.1.

The Southern Alps comprises a Paleozoic lower crustal unit and a Carboniferous to Permian upper crustal basement, which are both overlain by Late Paleozoic to Neogene volcanic and sedimentary cover rocks (Schmid et al. 2004). Tectonically it can be separated into the western Lombardic-Giudicaric fold and thrust belt and the eastern South Alpine units of the Carnian Alps, Julian Alps and Dolomites (Froitzheim et al. 2008). The Southern Alps were derived from the Apulian continent (Schmid et al. 2004) and were formed, when basement and cover rocks thrusted onto the foreland of the Adriatic continent and the Dinarides during the Neogene (Schmid et al. 2020).
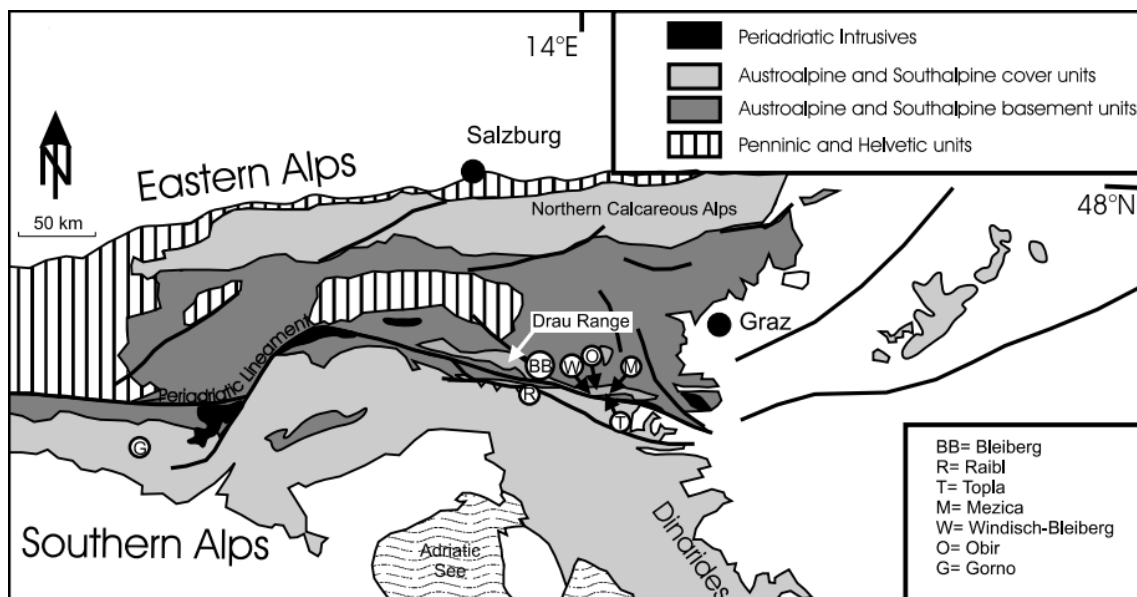
Figure 3.1.: Simplified map showing part the Easter and Southern Alps, modified from Schroll and Rantitsch (2005)

3.2. Local geology of the deposit
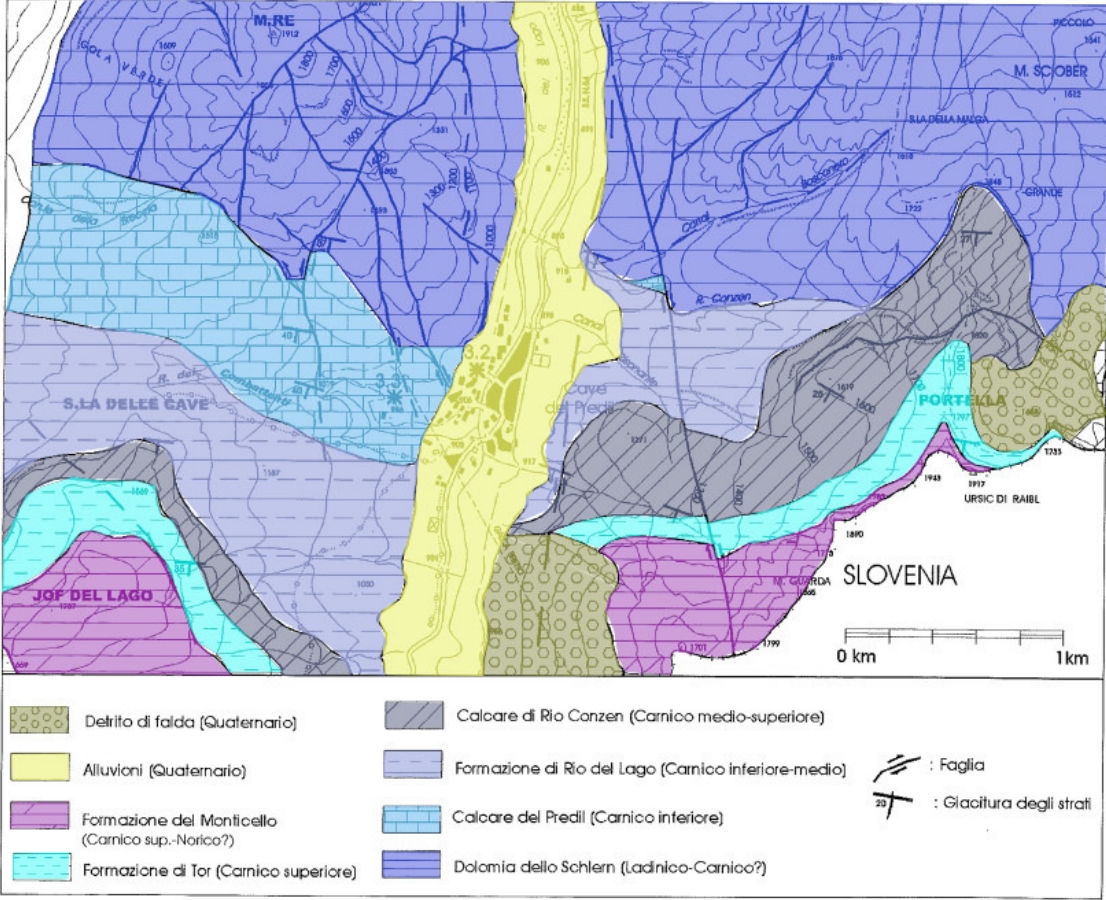
Figure 3.2.: Geological Map of the area surrounding Raibl, modified from De Marco et al. (2000)

The deposit of Raibl is situated at the eastern edge of the Carnian Valbruna-Raibl basin, which is considered trending W-E (Brigo and Omenetto 1978; Lieberman 1978). This basin formed due to synsedimentary, tectonic activities at the Ladinian-Carnian boundary (Lieberman 1978). Several N-S-trending sinistral strike-slip faults can be found within the Raibl valley (Doglioni 1988). This is significant since the Raibl mineralizations are often bound to faults showing N-S-direction (see section 4.3). A geologic map of the area surrounding Raibl can be seen in figure 3.2.

3.2.1. Pre-Ladinian and Ladinian Stratigraphy in the area of the deposit
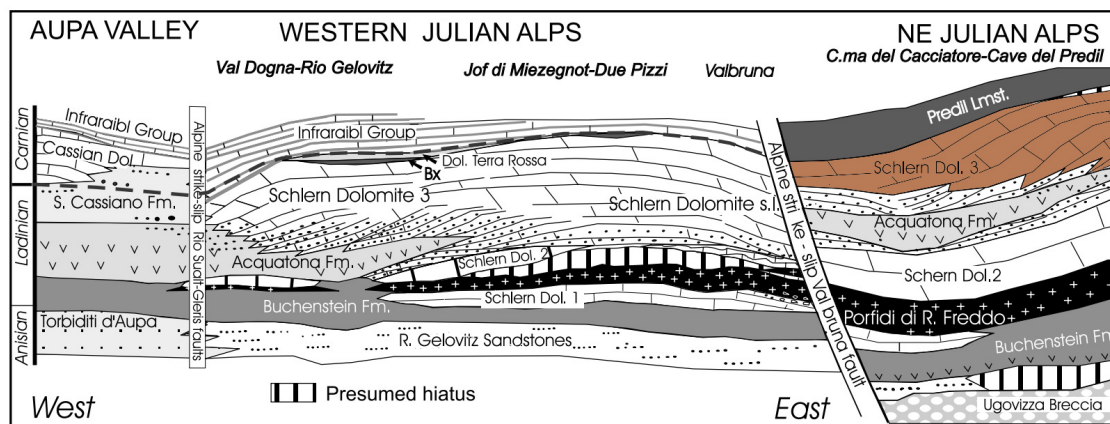
Figure 3.3.: Ladinian stratigraphy of the Julian Alps and the Aupa Valley, modified from Jadoul et al. (2002), the ore bearing Schlern dolomite found in Raibl is marked in brown

The base of the Triassic stratigraphy in this area forms the Scythian Werfen Formation containing sandstones, marls, siltstones, calcarenites and limestones (Cerny 1989b; Carulli 2006; Assereto et al. 1968). The overlying Anisian Ugovizza Breccia consists of coarse breccias and conglomerates (Jadoul et al. 2002; Assereto et al. 1968). The Lower Ladinian Buchenstein Formation (also known as Livinallongo Formation) contains limestones, calcarenites and volcanoclastics (Jadoul et al. 2002; Assereto et al. 1968). The Lower Ladinian porfidi di rio freddo (Kaltwasser Formation; Vulcaniti di Rio Freddo) consist of conglomerates, tuffaceous sandstones, volcaniclastics and volcanites (Jadoul et al. 2002; Cerny 1989b; Assereto et al. 1968). The Early - Late Ladinian Schlern Formation in the Southern Alps consists of calcarenites, calcirudites, megabreccias, (dolomitic) limestones, dolostones (Jadoul et al. 2002). This formation is also known as Schlern Dolomite, Dolomia dello Schlern and Sciliar Dolomite (De Zanche et al. 2000). In Raibl it is locally called Dolomia Metallifera (metal-bearing dolomite) (Brigo and Omenetto 1978). The formation corresponds to the Wetterstein Formation of the Eastern Alps (Cerny 1989b). The Schlern Dolomite in Raibl is further divided into an upper and a lower Schlern Dolomite, separated by the Late Ladinian Acquatona Formation, also named (Pseudo-)Buchenstein and Pseudolivinallongo (Brigo and Omenetto 1978; Jadoul et al. 2002). The Acquatona Formation is described as green marly layers containing pyrite, dark bituminous limestones, green tuffaceous sandstones and tuffites (Brigo and Omenetto 1978). The Schlern Formation is overlain by the Carnian Raibl Group (Brigo and Omenetto 1978). The succession of formations between the Uggovizza Breccia and the Calcare del Predil formation (Predil limestone) can be seen in figure 3.3.

The lead-zinc mineralization of Raibl is spatially linked to the Upper Dolomia Metallifera between the Buchenstein and the contatto scisti (definition see below) (Brigo and Omenetto 1978). The mineralization is limited by the Rinnengraben-Bärenklamm and Fallbach tectonic lines (Brigo et al. 1977). A fault map of the area can be seen in figure 4.2. The spatial distribution of the mineralization is considered corresponding to the extensions of the lower section of the Carnian Calcare del Predil formation (Brigo et al. 1977).

3.2.2. Carnian stratigraphy in the area of the deposit - the Raibl Group

The Carnian stratigraphy of the Raibl area consists of different formations of the Raibl Group, which can be seen in figure 3.4. The Raibl Group contains the Calcare del Predil Formation (in figure 3.4 displayed as Fischschiefer), the Rio del Lago Formation, the Calcare di Rio Conzen Formation, the Tor Formation, the Portella dolomite and the Carnitza Formation. The Tor Formation, the Portella dolomite and the Carnitza Formation are displayed as Torer Schichten (i.e. Beds of Tor) in figure 3.4. The exact borders of the Rio del Lago Formation and the Calcare di Rio Conzen Formation is unfortunately not visible in figure 3.4. Organic matter is widespread within the Raibl Group (De Marco et al. 2000). The Raibl Group is famous for fossils of marine organisms found in various formations pertaining to this group (De Zanche et al. 2000).

The Calcare del Predil Formation (also known under the name Predil Limestone) is described as dark, highly bituminous marls and dolomites (Brigo and Omenetto 1978; De Zanche et al. 2000). Lighter dolomites have also been reported (De Marco et al. 2000). The rocks are well stratified (Brigo and Omenetto 1978). The Calcare del Predil formation is renowned for its fish fossils, additionally remains from invertebrates and plants have also been described (Tintori 1992; De Marco et al. 2000). The contact between the Dolomia Metallifera and the Calcare del Predil Formation, called contatto scisti, was marked by breccia within the mine (Brigo and Omenetto 1978).

The Rio del Lago Formation (other name: Formazione di Rio di Lago) contains marls, limestones, as well as argillaceous limestones (De Marco et al. 2000; De Zanche et al. 2000). Remains of bivalves have been reported (De Marco et al. 2000). The Calcare di Rio Conzen Formation (also known as Conzen Formation) consists of dolomite and limestone, as well as pelites (De Zanche et al. 2000). Foraminifers and large bivalves have been found within the formation (e.g. Megalodonts) (De Marco et al. 2000; De Zanche et al. 2000). The Tor Formation (also known as Torer Schichten in older literature or Formazione di Tor) consists of dolomite, (marly) limestone, siltstones and (silty) marls. Calcarenites can also be found (De Marco et al. 2000; De Zanche et al. 2000). The Portella dolomite and the Carnitza Formation (dolomitic limestones) form the top of the Raibl Group (De Zanche et al. 2000). The Carnitza Formation may correspond to the Monticelli Formation in some areas (De Zanche et al. 2000). The Raibl Group is overlain by the Carnian-Norian Main Dolomite (Dolomia Principale, Hauptdolomit), which builds the top of the mountains near Raibl (De Zanche et al. 2000). Additionally to everything mentioned above, Quaternary and glacier deposits have been identified in the Raibl area (Calligaris et al. 2017).

Series

Marl

Upper

Limestone
Layer

Lower Marl Series

Fisch-
schiefer

Ladinian
Dolomite

Main Dolomite

Torer Schichten

Limestone Series

Stratigraphic Column of the Raibl Group

L E G E N D

Aufschluß unterbrochen (Fallstücke)
polymikte Quarzsandsteine
sandig
Tonmergel, Mergeltone
Kalkmergel, Mergel
Mergelkalke
Dolomite
mergelige Kalke

Oolithe
Onkolithe
Lumachellen
sandige Kalke
knollige Kalke
Hornsteine
Camgite
resedimentierte Pellets
kalkige Stromatolithe
dolomitische
ungebankte Dolomite
gebankte Kalke
ungebankte

Figure 3.4.: Carnian stratigraphy of Raibl (Cave del Predil), modified after Schulz 1970; Oolithe=ooliths, Onkolithe=oncolites, Lumachellen=coquina, sandige Kalke=sandy limestone, knollige Kalke=nodular limestone, Hornsteine=cherts, resedimentierte Pellets = redeposited pellets, kalkige Stromatolithe = calcareous stromatolites, dolomitisch = dolomitic, ungebankte Dolomite=unbedded dolomites, gebankte Kalke=bedded limestone, mergelige Kalke/Mergelkalke = Limestones with varying marl content, Mergel=marl, Ton-mergel/Mergelton = marly clays with varying limestone content, sandy=sandig, polymikte Quarzsandsteine = polymict quartz sandstone, quarzsandiger Mergel = marl containing quartz sands, Aufschluß unterbrochen (Fallstücke) = outcrop discontinued

4. General features of the Raibl ore deposit

4.1. Location of the mine

The village of Raibl (Cave del Predil) is located approximately 9km south of Tarvis (Tarvisio)(46.4425°, 13.571389° in WGS84) in the province of Friuli Venezia Giulia, northern Italy (figure 4.1). The town itself is situated at an altitude of 899m in the Seebachtal (Valle del Rio del Lago), which is the upstream part of the Gailitz valley. The Raibl lead-zinc deposit is located north of the Raibl settlement, in the Kleiner Königsberg (Piccolo Monte Re) (Göbl 1903; Frangipani 2013).
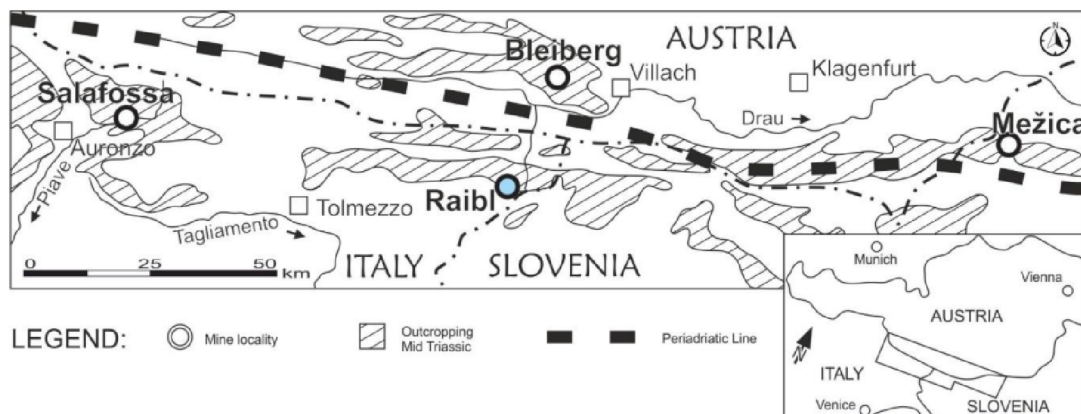
Figure 4.1.: Location of Raibl and three other lead-zinc deposits (Bleiberg, Mežica and Salafossa), from Barago et al. (2021), originally from Brigo et al. (1977)

4.2. History of the mine

The Raibl deposit is known since antiquity. Mining operations started in the 14th century or perhaps even earlier (Barago et al. 2021; Jicha 1951; Kraus 1913). In the 19th century traces of fire-setting, as well as signs indicating hammer and pick work, were found at the mine location. These were interpreted as indications for medieval mining (Kraus 1913; Posepny 1873).

Mining first started as surface mining and later changed to underground mining (Barago et al. 2021). It has been suggested that production started with galena and transformation products of sphalerite. Therefore it is assumed that at first production concentrated on the areas near the surface and the parts of the mine, which were rich in lead (Kraus 1913; Posepny 1875). For the 16th century exists documentation for production of lead, calamine and a mineral substance, which was probably goslarite (Posepny 1875).

During the early onset of mining, the mine did not have one owner but several owners (Kraus 1913). During the second half of the 18th century, the Austrian state started buying portions of the mine (Posepny 1873), however in the 19th century the mine was still divided in two parts - a state run (called Ärar) and a privately run (called either Struggl after the owner Cyprian Struggl or Gewerksschaftsanteil). The private part was later bought by the Counts of Henckel von Donnersmark (Di Colbertaldo 1951; Göbl 1903). The parceling of the mine led to fewer scientific publications concerning the privately operated part of the mine, for example the maps of (Göbl 1903) only show the statal part of the mine in detail. On the 8th of January 1910 a sinkhole suddenly developed due to the inrush of water and rock material in the subsurface. This lead to the destruction of a hospital above ground and the death of seven people (Anonymus 1910). During World War I, the mine of Raibl was considered strategic for war (Pucher 2016).

After World War I, the deposit became possession of the Italian state (Frangipani 2013; Di Colbertaldo 1951). The Società Anonima Miniere Cave del Predil (Soc. An. Miniere Cave del Predil) was responsible for mining in Raibl after 1923 (Di Colbertaldo 1948a). Production finally ended in 1991(Petrini et al. 2016).

It is estimated, that about 1.5 million tons of lead and zinc were produced from the Raibl mine (Cerny 1989a). Products from the mine were not only used for metal production, but also for paint (ocher for yellow paints) (Göbl 1903; Posepny 1873). Approximately 120 kilometers of tunnels at an area of 2.5km^2 with a height difference of 1000m had been excavated (Frangipani 2013).

Between 2008 and 2009 drainage machinery was shut down, which caused flooding in the lower parts of the mine (Petrini et al. 2016). Today the mine is used as a touristic attraction (Petrini et al. 2016).

4.2.1. Environmental concerns

The first reports of efflorescences on old dump sites date back to the 19th century (Posepny 1875). In the same text it is stated that meadows in vicinity of sphalerite and calamine outcrops were considered unsuitable for animal husbandry. This area therefore gained the name "Böses Gras" (Bad Grass)(Posepny 1873).

Environmental concerns arose in the years following the decommission of the mine, as it was revealed that until 1952 the processing unit's wastewater had been disposed (unfiltered and untreated) into the nearby river. Treatment of slurries in impoundments started only in the 1970s (Barago et al. 2021; Fellet et al. 2011; Fellet et al. 2012). In 2010 elevated thallium concentrations were found in surface water near the mine site ($5 - 30\mu g/l$), which exceeded the legal thresholds of Italy ($2\mu g/l$) (Petrini et al. 2016). Since heavy metals can be used by some plants, scientific attention also turned to the flora surrounding Raibl. A special type of violet (Viola tricolor) was found in the vicinity of the deposit which tolerates soil with high heavy metal contents (Lausi and Cusma Velari 1986). Furthermore, the flowering plant Thlaspi rotundifolium spp. cepaeifolium was discovered. It can contain up to 2% zinc and 1% lead. This plant was seen growing on soils above the Raibl deposit and along the river Schlitza due to contamination by mine

debris (Baker et al. 1988).

4.3. Geology of the Raibl mine

The Raibl mine has, for a long time, been divided into a sulfidic ore part and calamine part. This partition is clear in the east of the mine, but different ore types can coexist in other areas of the mine. Generally, the calamine is nearer to the surface than the sulfides (Göbl 1903; Cotta 1863; Kraus 1913). A map of the Raib mine can be seen in figure 4.3.

The mineralization is bound to fault systems, but can deviate a bit from the main mineralizing faults (Jicha 1951). The mineralization itself has been described as vein-like or as veinlets (Cerny 1989b), but also as columnar stocks (Omenetto 1980), as well as minor occurences of stratiform ores at the contatto scisti (Brigo et al. 1977).

Different fault systems have been described in the Raibl mine, e.g. Abendblatt system, Morgenblatt system, Luschari system, Rauschenbachblatt system, Vincenzi-Aloisi-Josefi-System/Vincenci-Aloisi-Blatt system (Posepny 1873; Kraus 1913). They are considered syngenetic to the deposition of the Carnian Raibl Group (Brigo et al. 1977). The faults have been classified as tear faults (Jicha 1951). The fault planes, named "Blatt" in older literature concerning the deposit, are sometimes polished, others contain fault gouge. Two different sets of slickenslides have been described. Fault-associated breccias can be found within the mine (Göbl 1903; Kraus 1913; Posepny 1873). Faults in N-S-direction (Abendblatt, Morgenblatt, Struggl, Aloisi and Fallbach) and in NE-direction (Rinnengraben-Bärenklamm), as well as in NNW to NW-direction (Abendschlag, Vincenzi), have been described. These north-trending faults exhibit an easterly dip direction (Brigo and Omenetto 1978; Di Colbertaldo 1951; Omenetto 1980; Göbl 1903) (figure 4.2). The faults show varying displacement in the mine, where even the ore bodies are sometimes offset along faults (Posepny 1873). At the surface, these underground fault structures are evident as ravines (Posepny 1873; Kraus 1913; Göbl 1903). Presumably the faults within the deposit do not belong to one, but several different generations of tectonic activity (Posepny 1873; Di Colbertaldo 1948a).
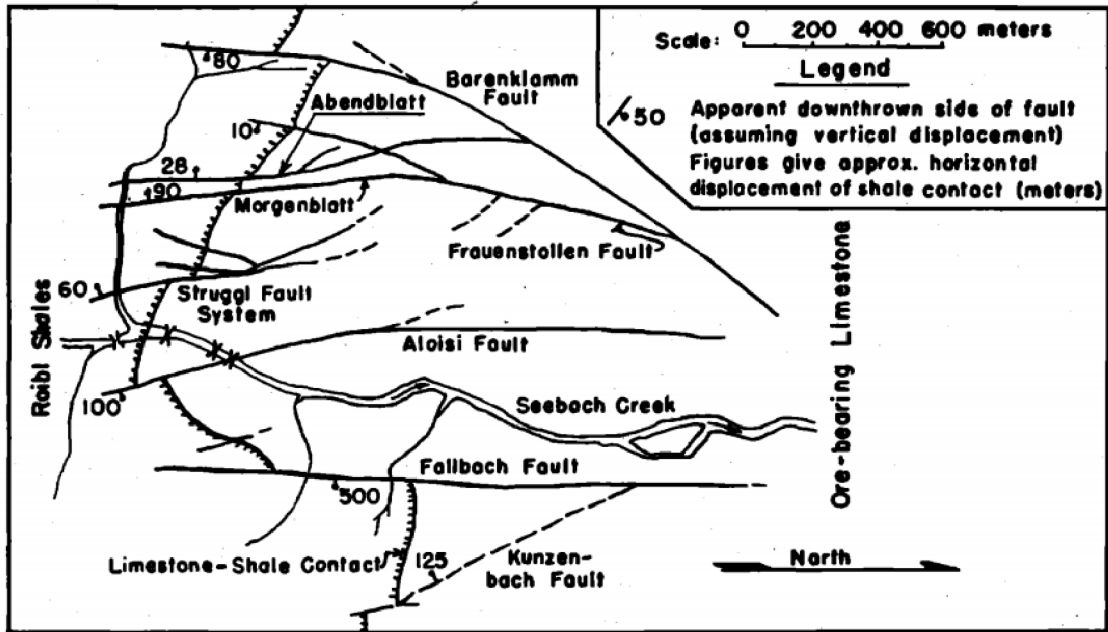
Figure 4.2.: Map of the faults present in Raibl, from Jicha (1951)
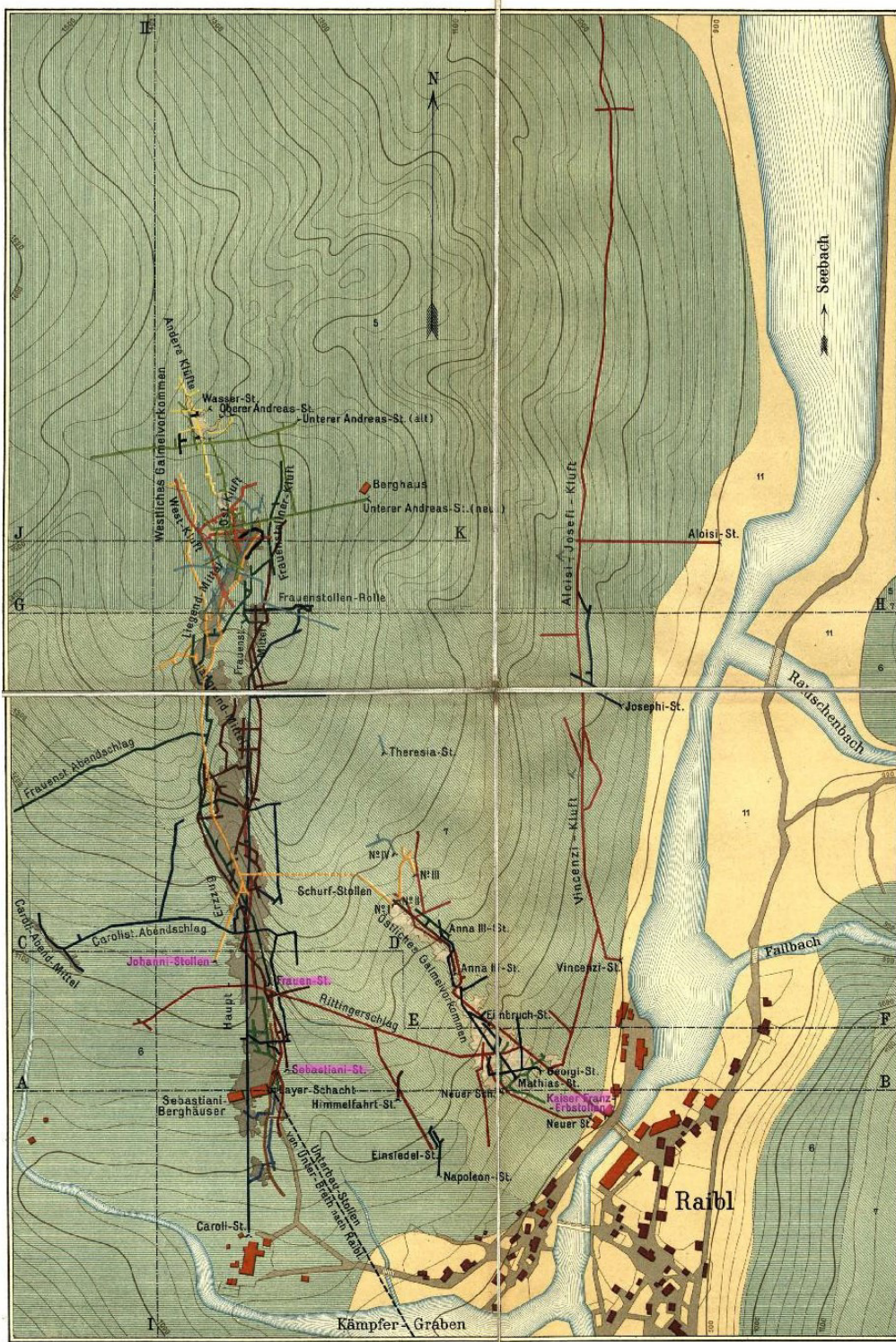
Figure 4.3.: Map of the Raibl mine in 1903, from Göbl (1903), places of origin of the samples used in the study have been marked pink, if present in the map

4.3.1. Sulfidic ore

The sulfide ore is hosted by dolomite (Göbl 1903; Posepny 1873). The thickness of the individual ore bodies vary between 30 and 70m, at a a strike length of approximately 50 to 140m (Göbl 1903). Attempts were undertaken in former times to classify ore by using the ratio of lead to zinc. This ratio was 1:5 (Cerny 1989b; Omenetto 1980; Brigo et al. 1977) or 1:4 (Jicha 1951) for the Raibl deposit. The deposit has an average zinc content of 4% (Fornaro 1985).

Ore minerals

The most prevalent ore minerals are galena and zinc-sulfides (sphalerite/wurtzite). Additionally iron-sulfides (pyrite/marcasite) can be found (Jicha 1951; Kraus 1913).

Sphalerite   The mineral is described as fine-crystalline, compact and massive (Posepny 1873). Sphalerite is mostly present in the mine as schalenblende (colloform sphalerite, sometimes also named Granatblende) (Jicha 1951;Posepny 1873; Cotta 1863). Banded textures are also possible (Göbl 1903). Sphaleritic stalactites have also been described in the deposit. (Kraus 1913).

A remarkable feature of sphalerite from Raibl is its diversity in color. Known are varieties in brown, black, red, yellow, grey and colorless (Posepny 1873; Göbl 1903; Di Colbertaldo 1951; Jicha 1951). Several authors tried to define trends of color within the deposit. Red sphalerite can be found in the north of the deposit, colloform sphalerite in the center, crystalline varieties and yellow varieties in the south. However, strict borders cannot be defined (Di Colbertaldo 1950; Cerny 1989a).

Galena   Galena shows different textures in the deposit. It can occur as cubes or octahedrons, hexahedrons with blunt corners, crusts and vein fillings and as bands. Disseminated and massive ore have also been described. (Jicha 1951; Posepny 1873; Göbl 1903; Cotta 1863). The galena content varies throughout the mine (Göbl 1903; Tornquist 1931).

Pyrite and marcasite   The iron-sulfides of the deposit can be classified as crystalline pyrite in the south of the deposit, colloidal pyrite in the center of the deposit, whitish pyrite with radial structures and sometimes sulfur-poor colloidal pyrite in the center and the north, crystalline marcasite in the center and the north (Di Colbertaldo 1954). Idiomorphic marcasite crystals have been found in the Struggl fault (Di Colbertaldo 1954). It should be mentioned that Di Colbertaldo (1954) noted that the distinction between pyrite and marcasite could not always be made successfully. Marcasite occurs as fine crystalline, fibrous aggregates or small massive parts, often near the hanging wall (Posepny 1873). The aggregates can have a mammillary texture. The mineral is first brass-colored, but changes to brown after being exposed to fresh air. Marcasite is often associated with the red colloform sphalerite and often occurs in the northern part of the deposit (Di Colbertaldo 1954). Marcasite, that forms an outer rim to the colloform sphalerite by imitating its form has also been described (Kraus 1913). The pyrite-marcasite mixture "melnikovite" has also been described in the Raibl deposit (Brigo and Omenetto 1978; Brigo et al. 1977).

Secondary minerals and accessory minerals Occurrences of pyrrhotite, chalcopyrite, arsenopyrite and cinnabarite have been documented in the mine (Jicha 1951; Kraus 1913). Alteration products of chalcopyrite, such as malachite stalagmites, have also been described (Kraus 1913). Fluorite can occur as filling between sulfides or as inclusions in dolomite (Jicha 1951). Crocoite was supposedly found on one single sample from Raibl (Kraus 1913), however, given the lack of a chromium source needed for mineral formation and evidence coming only from one sample, this identification remains dubious. Besides the ocher in the calamine section (see section 4.3.2 below), a black to brown, lustrous powdery substance has been found in the sulfide part of Raibl. It has been described as a mixture of calcium-carbonate, iron-carbonate and magnesium-carbonate, as well as pyrite and clay. The texture of the loose material seen on surfaces is compared to fern (Göbl 1903).

Ore textures containing more than one mineral

A special ore texture is the "Schiefererz" - layered dolomite intercalated with galena and sphalerite (Göbl 1903). There is also ore breccia, containing colloform sphalerite and other ores as fragments, which are cemented with dolomite (Posepny 1873). There are also galena textures which have been compared to lettering (Schrifterz - columnar texture of galena surrounded by sphalerite or other minerals) or moss (Mooserz) (Posepny 1873; Cotta 1863; Göbl 1903).

Röhrenerze (tubular ore) Röhrenerz or Röhrlerz (tubular ore) is a special ore type of Raibl. Since they are rare, these ores do not have any economic value (Göbl 1903). Tubular ore was first only found at two locations in the mine - in the deeper sections of the Struggl part and at the Johanni level (Posepny 1873; Pošepny 1887). Later this ore type was also found in the "Grotte" (grotto), a natural cavity found at the Johanni Level in 1892 (Göbl 1903) and in an undefined place within the main mineralization (Haupterzzug, colonna principale)(Di Colbertaldo and Feruglio 1963). Within the "Grotte" the tubular ore was situated atop of ochre and calamine. The tubes were surrounded by clay and mud (Göbl 1903).

The texture can be described as galena tubes (figure 4.4). They are either filled by an earthy substance or hollow. Some of them were found isolated, others intergrown with their surrounding material. The tubes are between 10.5 and 16 cm long, or even smaller. Isolated tubes can be ten times as long as wide. They show a diameter of 5 to 20mm. It has been suggested, that some tubes could be even longer, since in some cases complete tubes have not been examined, only fragments (Pošepny 1887; Posepny 1873).

Figure 4.4.: Sketch showing galena in tubular form, modified after Posepny (1873)

The tubes can be vertical, but can also cross each other. They sometimes influence each others growth direction when intersecting (Morlot 1850; Posepny 1873)(figure 4.5). Both straight and spiral or distorted tubes have been described (Posepny 1873; Göbl 1903). The end of a tube can be a trihedral pyramid or blunt with only one plane (Posepny 1873). In some cases one end of the tube is funnel-shaped. In rare cases cerussite-druses were found in these funnels (Posepny 1873). The tubes have a four-sided or six-sided cross section, however, other forms (e.g. round, oval and biconvex) have also been found (Pošepny 1887; Göbl 1903). Figure 4.6 shows a rounded cross section of a tubular ore.
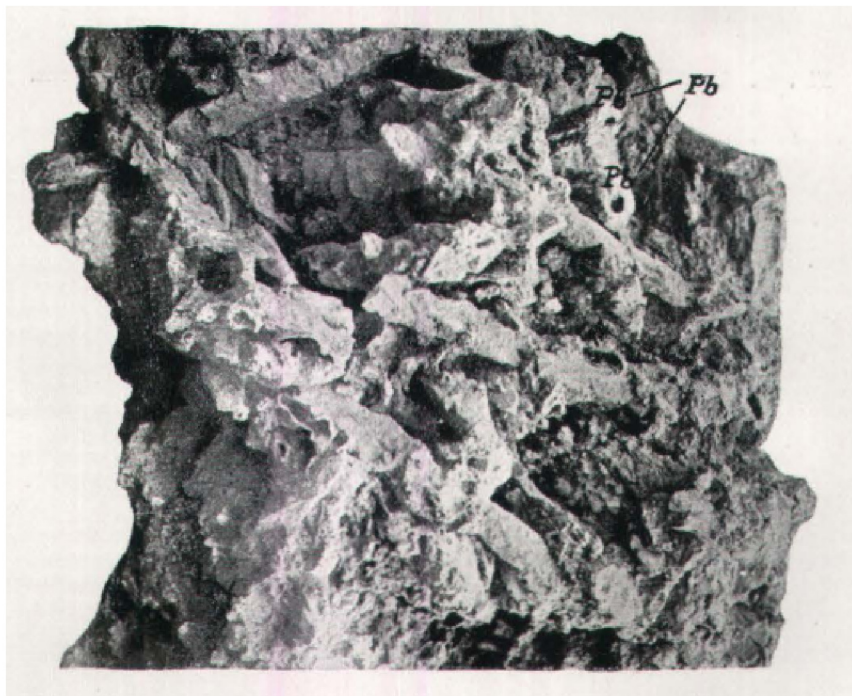
Figure 4.5.: Black-and-white photograph of several intersecting tubes, Pb stands for galena, from Kraus (1913)
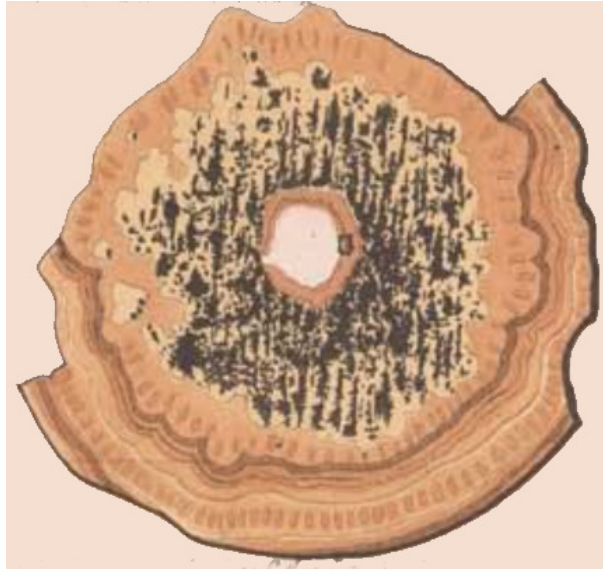
Figure 4.6.: Central part of a tubular ore, modified after Pospny (1873)

	minerals in the center	minerals surrounding the core	minerals at the rim
variety 1	white unknown mineral	pyrite/galena, followed by sphalerite (various types)	red, radially fibrous sphalerite
variety 2	white unknown mineral	pyrite/galena, followed by alternating pyrite and sphalerite	reddish-brownish sphalerite
variety 3	galena	yellow sphalerite/pyrite	grey sphalerite
variety 4	dolomite	pyrite/galena or galena	reddish-brownish sphalerite

Table 4.1.: Varieties of mineral assemblages found in tubular ores; compiled after Posepny (1873) and Posepny (1887)

Several mineral assemblages in the tubes have been described, which are summarized in table 4.1. Generally galena is nearer to the center of the tubes, while sphalerite forms the rims (Posepny 1873; Pošepny 1887). Examples of compositions of tubular ore can be seen in the figures 4.7, 4.8 and 4.9. In some cases the pyrite is intergrown with the galena, in some cases they are in separate bands. The galena building these tubes shows banding (Posepny 1873). In some cases the tubes were surrounded by cellular calcite or cellular smithsonite filled with a powder containing carbonates, ocher and sulfur-containing minerals. In other cases the tubes were ingrown in sphalerites (Posepny 1873). An outer covering of the tubes made out of cerussite were found in the "Grotte" (Göbl 1903).
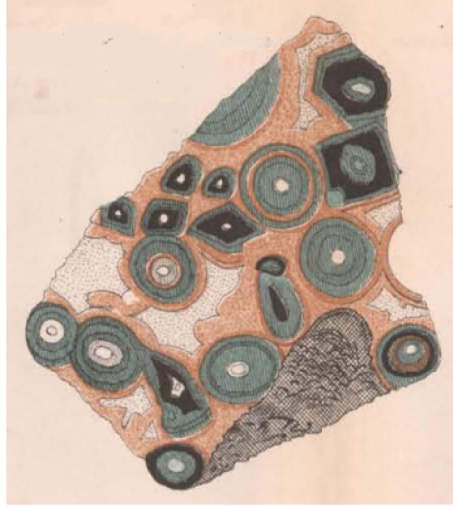
Figure 4.7.: Assemblage of different tubes, locality unknown, modified after Posepny (1873)

Figure 4.8.: Assemblage of different tubes, found at Johanni level, from Posepny (1873)

Figure 4.9.: Assemblage of different tubes, found in the Struggl part of the mine, modified after Posepny (1873)

In the past the generation of this ore type was attributed to stalactitic formation in cavities (Posepny 1873) or fossils (Di Colbertaldo and Feruglio 1963). A definite explanation for these growth were not found (Pošepny 1887; Göbl 1903; Cotta 1863).

Gangue minerals and host rock

The main gangue minerals are calcite, dolomite and barite (Jicha 1951). Dolomite and calcite showing foliation and layered textures have been described within the massive

dolomite, with galena and sphalerite along the bedding planes (Göbl 1903). Quartz has been described as a rare component of the gangue (Tornquist 1931).

Dolomite Dolomite occurs as dark grey dolomite, light grey dolomite and cellular dolomite, as well as a dolomite type that is characterized by containing veinlets (Göbl 1903). A dolomite type called "Lithodendron-Dolomite" has also been described (Göbl 1903)(figure 4.10). Layered dolomite (Dolomitschiefer) occurs with fine-grained to fine-crystalline layers, showing grey to black colors and is described as having a bituminous smell upon breaking. This rock type hardly contains ore (Posepny 1873). Larger cavities and druses have been found in the dolomite (Posepny 1873).
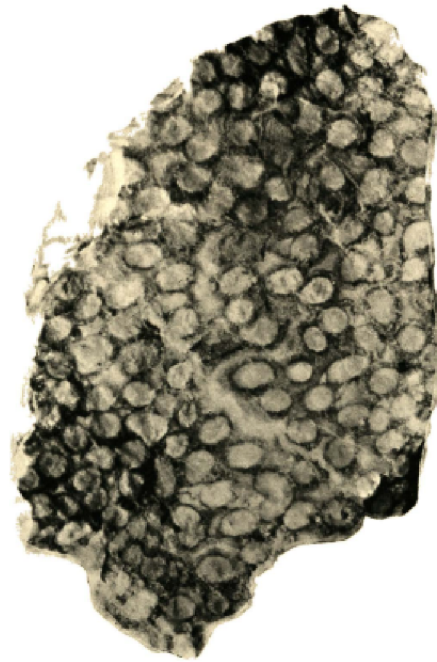
Figure 4.10.: Drawing depicting "Lithodendron-Dolomite", from Barbara-Mittel (part of Hangendmittel), 15m over Sebastiani Level, picture from Göbl (1903)

Barite Barite occurs as acicular crystals in bundles, tabular crystals or in massive form. It is linked to either sphalerite or dolomite (Jicha 1951; Posepny 1873; Kraus 1913). (Cotta 1863) also mentions lead-rich barite.

Limestone Layered limestone (Kalkschiefer), exhibiting marly, sandy and bituminous layers have been described, however they seem to be rare in the sulfidic part of the mine. They are the only calcitic host rocks for the sulfide ore, as most sulfidic ore is bound to dolomites (Posepny 1873).

Fossils The 19th century literature mentions, that fossils were found within the mineralized rocks. They were identified at that time as Natica, Orthoceras, Lithodendron and unspecified bivalves (Posepny 1873). Given that these fossils are rare, they were found in the uppermost part of the mineralized rocks and the exact stratigraphy of the Southern Alps was not fully established yet, it remains unsure if these fossils really were part of the

Dolomia Metallifera or actually belong to the lowermost parts of the Raibl Formation, which is known to contain fossils (see section 3.2).

Organic matter Bitumen inclusions in dolomite have been reported (Jicha 1951; Posepny 1873). In one place (Lobkovitz-Schlag), a gas leak (H_2S) was recorded (Posepny 1873).

4.3.2. Calamine ore

The calamine deposit is hosted within limestone (Posepny 1873). Calamine in Raibl consists mainly of hydrozincite, smithsonite and to a lesser extent hemimorphite. The calamine composition varies throughout the mine (Göbl 1903). There are also mentions of reddish calamine, which gets its color from ironoxide. This part of the deposit also contains limonite and willemite. Clays showing different colors and a iron hydroxide-ocher, with varying zinc content called "Moth" exhibiting different colors (yellow, red, black), have also been reported (Posepny 1873; Göbl 1903; Kraus 1913).

Sphalerite is not present in this part of the mine (Göbl 1903), although the colloform sphalerite texture (concentric textures) remains in some parts of the calamine as a pseudomorphosis (Kraus 1913; Posepny 1873). Layered limestone and calcareous schist intercalated with thin layers of ocher and calamine have been found, this has been interpreted as analogue to the "Schiefererz" in the sulfide part (Göbl 1903).

Galena can still be found in the calamine part and an unidentified alteration of galena is only visible as a loss in its crystal luster (Kraus 1913). Dendritic galena in calamine has been described, however it only occurs in the western part of the calamine deposit and is seen as rare (Göbl 1903)(figure 4.11).
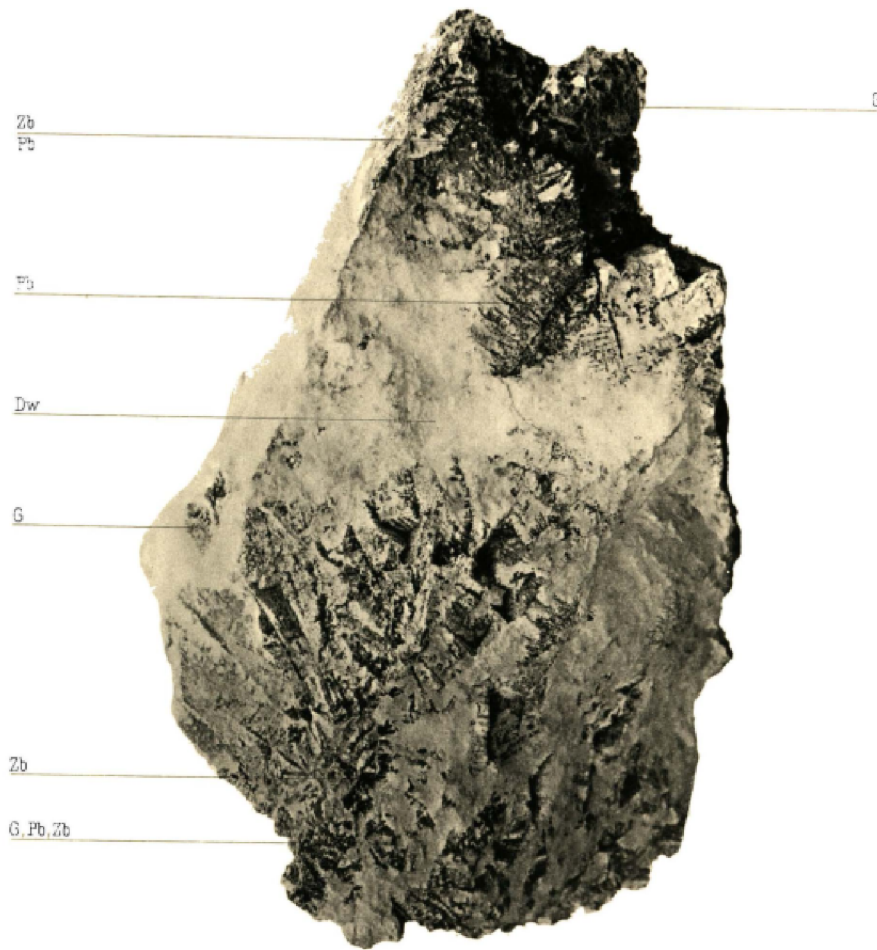
Figure 4.11.: Drawing depicting calamine with dendritic galena, from the western Calamine Deposit, found at Westkluft/7. Johanni-Firstenlauf, picture from Göbl (1903) (G-calamine, Zb-sphalerite, Pb-galena, Dw-white dolomite)

The calamine part of the mine is strongly associated with cavities and joints (Posepny 1873; Kossmat 1903; Göbl 1903). An extremely cavity rich-form of calamine (cellular calamine) is also described (analogue to the cellular dolomite, figure 4.12) (Kraus 1913; Kossmat 1903). In addition, calamine stalactites have also been described (Kraus 1913).
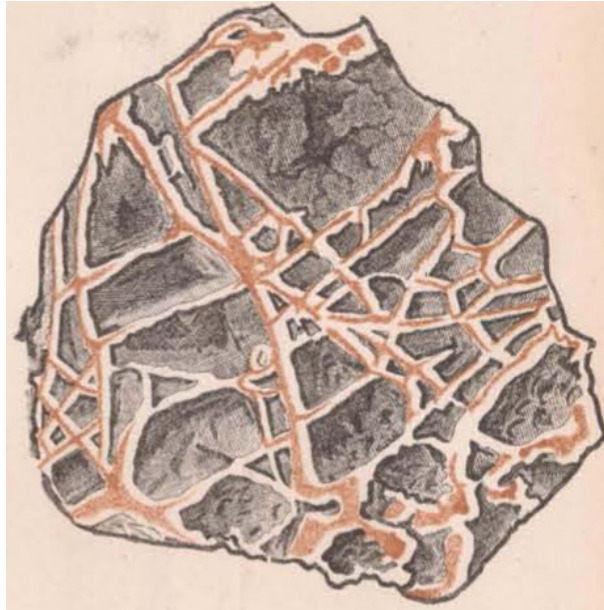
Figure 4.12.: Sketch showing cellular calamine, modified after Pospny (1873)

Calamine ore is seen as an alteration product of the sulfidic sphalerite into zinc-carbonates, zinc silicates and hydroxides due to the influence of meteoric water (Göbl 1903). In-situ calamine, as well as transported calamine have been described (Kraus 1913). In literature, the calamine part of the Raibl deposit is further divided into a limonite-rich upper oxidation zone, containing limonite, hydrozincite, melanterite, gypsum, goslarite, bianchite, anglesite, cerussite and wulfenite; and a lower carbonate-rich enrichment zone comprising cellular smithsonite and hydrozincite (Di Colbertaldo 1951; Brigo et al. 1977). Calamine can also occur as veins in the dolomitic sulfide part of the mine, which sometimes makes neatly separating the two types of deposits difficult in the mine (Göbl 1903). Different types of calamine ore have also been described in the "Grotte", a natural cavity at the Johanni Level (Göbl 1903).

Other minerals

Raibl is also the type locality for bianchite, which has been found in the efflorescence on mine walls in the superficial part of the mine (Vitriolwand) (Andreatta 1930; Anthony et al. 1990).

Host rock

The calamine part mostly shows limestone as its host rock (Posepny 1873). Limestone can appear as dark limestone, dolomitic limestone, black dolomitic limestone, light grey limestone with or without white veins and white greasy limestone (Göbl 1903). Within the calamine deposit limestone with black veins can be found (Göbl 1903). Cellular limestone has also been mentioned and compared to cellular calamine (Posepny 1873). Large cavities have been found in the limestone (Posepny 1873).

Other minerals and substances

A recent formation is "Haldenhärte". It is described as a cemented breccia or conglomerate consisting of fragments from the heap dumps of former mining operations or simply as

cemented rubble containing calamine (Göbl 1903; Posepny 1873). Haldenhärte was found in galleries near the surface of the valley (Göbl 1903; Posepny 1873).

4.3.3. Age of the Raibl mineralization

The host carbonates have been deposited during the late Ladinian (Jadoul et al. 2002). The lead-zinc sulfide mineralization itself is difficult to date and no exact data is available for the Raibl mine. The main mineralization is considered post-Triassic to Alpine Age (Brigo and Omenetto 1978). Jicha (1951) interprets the mineralization as Tertiary. Late Triassic to Early Jurassic age has also been proposed based on petrographic research, analysis of the connection between ores and faults, as well as carbonate cement stratigraphy conducted on similar deposits (Leach et al. 2003). An age of late Oligocene to early Miocene has been suggested, however, this result was not reached by dating methods, but by comparison of similar Alpine deposits (Di Colbertaldo 1948b). A minor part of the mineralization at the contact of Dolomia Metallifera and Raibl Group was considered syngenetic and of Triassic Age (Brigo and Omenetto 1978). Concerning the tectonic structures it has been suggested that they were active since the Upper Ladinian to the Alpidian times or until recently (Cerny 1989b).

4.3.4. Geochemistry of the deposit

In the 19th century speculations arose that varying iron and cadmium content of the sphalerite could be linked to its diverse colors (Posepny 1873). In 1913, an analysis of the colloform sphalerite detected thallium (Kraus 1913). Arsenic has also been found in sphalerite from Raibl (Tornquist 1931). Zinc ores from Raibl have elevated germanium contents (Cerny 1989a). A germanium content between 400 and 450ppm for the zinc ores was reported (Cerny 1989b). The red colloform sphalerite is exceptionally germanium-rich (400-1000ppm germanium)(Cerny 1989b). It has been also suspected, that red sphalerite contains higher amounts of iron (Jicha 1951). A more comprehensive geochemcial analysis of sphalerite from Raibl showed remarkable contents of manganese, iron, nickel, cadmium, thallium, germanium, arsenic and antimony (Schroll 1954). Another chemical analysis of sphalerite from Raibl in 1960 showed significant contents of manganese, cadmium, thallium, germanium, arsenic and minor contents of other elements (Hegemann 1960). Sphalerites from Raibl can contain up to 4000ppm of cadmium (Brigo and Cerrato 1994). The ratio of germanium to gallium was reported as 50, while the ratio of arsenic to thallium as 3 (Schroll 1996).

Pyrite may contain elevated thallium contents (Petrini et al. 2016). Arsenic-containing pyrite has also been described (Tornquist 1931). Iron-sulfides of this deposit do not contain any germanium or cadmium (Brigo and Cerrato 1994).

The deposit does not contain significant amounts of silver or copper (Göbl 1903; Cerny 1989a; Ebner et al. 1999). It has been reported several times, that galena contains low amounts of silver or no silver at all (Göbl 1903; Tornquist 1931; Schroll 1954; Schroll 1955; Omenetto 1980). It also lacks germanium and cadmium (Brigo and Cerrato 1994) However, Tornquist (1931) reports galena from Raibl containing copper and arsenic. High arsenic and antimony contents have been found in galena from Raibl (Schroll 1955; Schroll 1954). Minor thallium contents in galena have also been reported (Brigo et al. 1977).

Thallium-rich jordanite has also been found (Brigo and Cerrato 1994)

The deposit of Raibl in its entirety is enriched in arsenic, antimony and thallium (Schroll 1983). Brigo and Cerrato (1994) divide the mine by geochemistry into three sections (figure 4.13). In the northern part, higher contents of germanium, thallium and arsenic were found, while the cadmium content was decreased. In the southern part, increased contents of cadmium and to a minor degree gallium and antimony were reported, while contents of germanium, arsenic and thallium were lower. The transition zone showed intermediate values (Brigo and Cerrato 1994). No fluorine enrichment could be detected within the deposit (Hein and Schneider 1983).
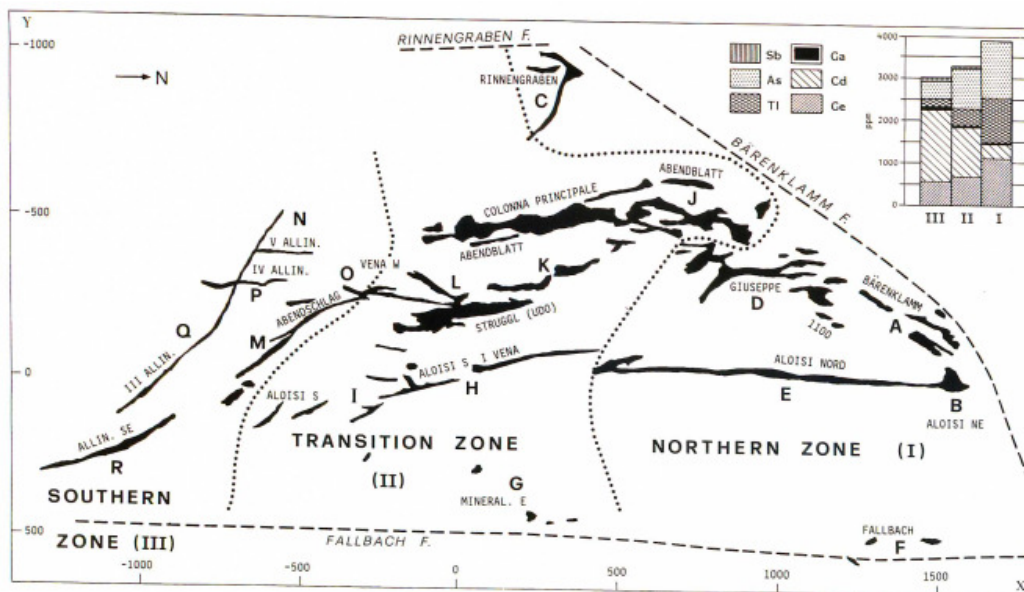
Figure 4.13.: Distribution of orebodies in Raibl and division into different areas by geochemistry after Brigo and Cerrato (1994), dashed lines represent faults, dotted lines borders between areas

Sulfur isotopes found in sulfides vary within the deposit. In the south $\delta^{34}S$ is slightly negative (-6.43 to -14.43 ‰), in the north highly negative (-21.71 to -25.60 ‰)(Cerny 1989b). The highest sulfur isotope values were found in recrystallized ores, the lowest in red sphalerite and melnikovite-pyrite assemblages (Brigo et al. 1977). It has been argued that the sulfur isotope variation found in the Raibl deposit indicates a low-temperature deposition and a multi-phase development of the deposit (Brigo et al. 1977).

5. Materials and Methods

5.1. Sample Material

In this study, 19 ore samples from the Raibl mine were examined. Since the mine is inaccessible now, the study solely relies on historical samples, which were kindly provided by the Chair of Geology and Economic Geology (Montanuniversität Leoben). As can be seen in the sample list in table 5.1, some samples are of unsure origin. A map showing the position of some of the known locations can be seen in figure 5.1. Combining older descriptions of the mine and microscopical examination, some samples can be linked to possible locations in the mine (see Discussion). The samples were prepared as polished sections at the Chair of Geology and Economic Geology.

Sample ID	Location of origin	No. of spot analysis
R-10	Danieli-Bau, Morgenblatt	25
R-16	Contact of ore-bearing dolomite and Raibl Group	35
R-17A	Sebastianistollen	23
R-17B	Sebastianistollen	0
R-20	Kalkschieferzone, Südschlagmittel	0
R-21	Kalkschieferzone, Südschlagmittel	14
R-24	Sebastianistollen	24
R-27	unknown	14
R-28	unknown	18
R-29	unknown	19
R-32	Sebastianistollen	21
R-36	unknown	7
R-40	Johannilauf	44
R-45	Franz-Sohlenlauf	36
R-49	Franz-Sohlenlauf	20
R-59	Franz-Erbstollen	54
R-63A	Frauen-Johannistollen	29
R-63B	Frauen-Johannistollen	0
R-67	unknown	48
RoeA	Frauen-Johannistollen	23
RoeB	Frauen-Johannistollen	0
Röhrenerz	unknown	0
total		454

Table 5.1.: List of samples that were used in this study and number of successful spot analyses on sphalerite done by LA-ICP-MS (A and B mark sections that were cut from the same sample)
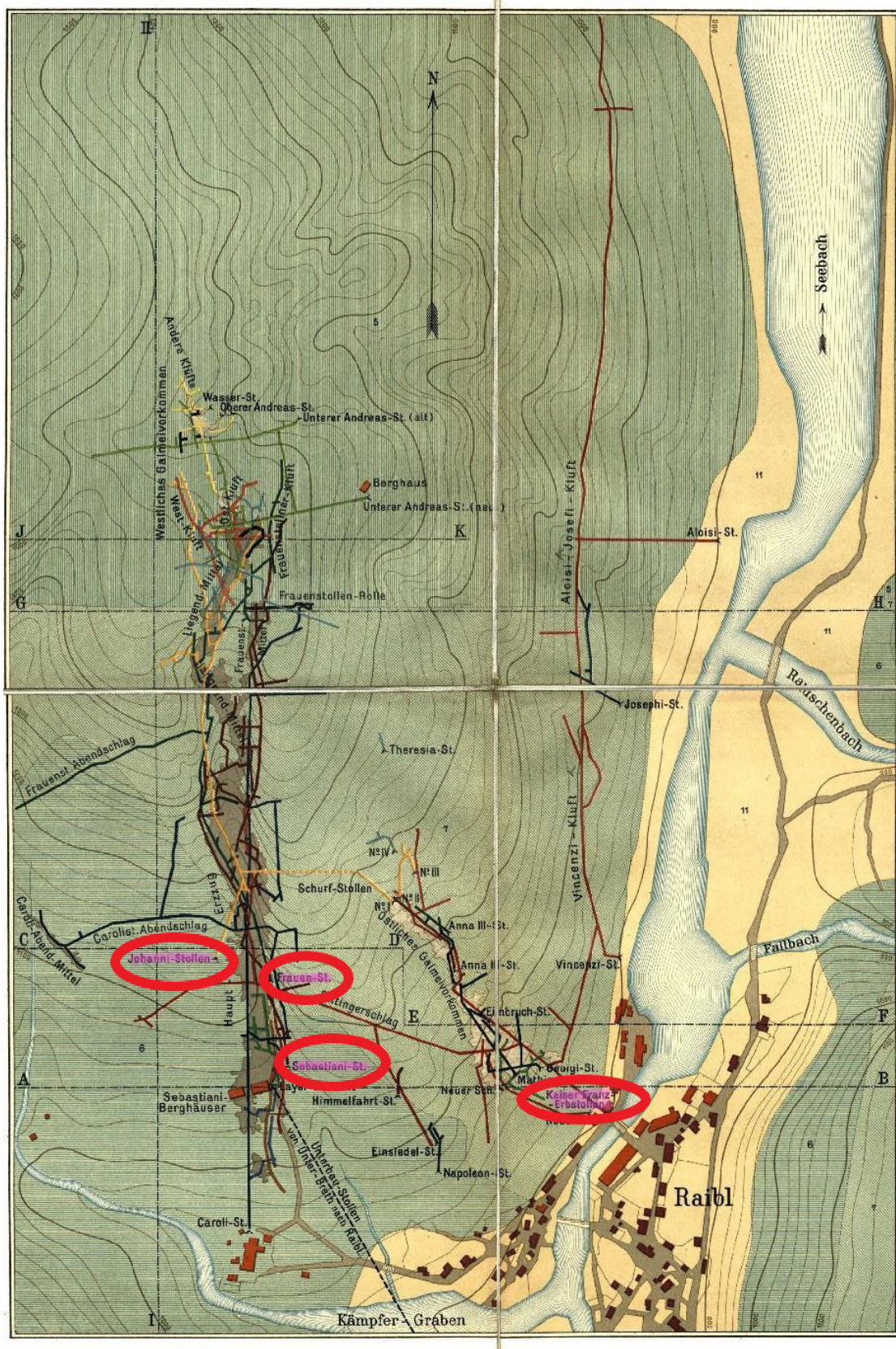
Figure 5.1.: Map of the Raibl mine in 1903, from Göbl (1903), places of origin of the samples used in the study have been marked, if present in the map

5.2. Optical Microscopy and UV light photography

All samples were studied and photographed by reflected light and ring light using the Keyence VHX 6000 digital microscope at the Chair of Geology and Economic Geology (Montanuniversität Leoben) with the intent to document, distinguish and identify minerals, colors and textures. Additionally, to further distinguish different types of sphalerite, the samples were photographed under UV-light by Dr. Aleš Šoster at the Department of Geology (University of Ljubljana). For the UV-light a UV-8S/L (Franz Krantz) ultraviolet (UV) lamp was used, which holds two 8-watt short ($\lambda = 254nm$) and long wavelengths ($\lambda = 365nm$) emitters.

5.3. Scanning electron microscopy (SEM)

Further, mineral identification and determination of element composition of the samples was conducted using the Zeiss Evo MA 10 SEM coupled with a Bruker Quantax EDX detector at the Chair of Geology and Economic Geology (Montanuniversität Leoben). SEM was a useful tool to determine zoning within the sphalerite textures and inclusions of other minerals within the ore.

5.4. Raman spectroscopy

Samples R-21, R-59, R-63A and RoeA were examined with Raman spectroscopy to distinguish the types of zinc-sulfide (sphalerite or wurtzite) and iron-sulfide (pyrite or marcasite). The sample Röhrenerz was examined to identify its mineral content. The Horiba LabRAM HR Evolution, which is part of the Raman-TERS-AFM laboratory at the Chair of Resource Mineralogy (Montanuniversität Leoben), was used for mineral identification. The strength of the laser was decreased to 1% by utilizing a filter to minimize the destruction of the mineral. Evaluation of spectra was conducted using the program CrystalSleuth, which is based on the RRUFF database (Laetsch and Downs 2006).

5.5. Laser ablation- induced coupled plasma - mass spectrometry (LA-ICP-MS) analyses

LA-ICP-MS was used for in-situ quantitative trace element spot analyses of sphalerite. The number of successful measurements of each sample can be seen in table 5.1. If two sections were cut from the same sample, only one was used for LA-ICP-MS analyses. Additionally, spot analyses were performed on pyrites found in sample R-27, of whom seven were successful. The measurements were conducted by an ESI NWR213 Nd:YAG laser ablation system linked to an Agilent 8800 triple quadrupole ICP-MS, at the Department of Applied Geosciences and Geophysics, Montanuniversität Leoben, Austria. The analyzed masses were ^{34}S, ^{51}V, ^{52}Cr, ^{55}Mn, ^{57}Fe, ^{59}Co, ^{60}Ni, ^{63}Cu, ^{65}Cu, ^{66}Zn, ^{67}Zn, ^{71}Ga, ^{72}Ge, ^{73}Ge, ^{74}Ge, ^{75}As, ^{82}Se, ^{95}Mo, ^{107}Ag, ^{111}Cd, ^{115}In, ^{118}Sn, ^{121}Sb, ^{125}Te, ^{197}Au, ^{201}Hg, ^{205}Tl, ^{208}Pb and ^{209}Bi. Furthermore, ^{24}Mg, ^{27}Al, ^{28}Si, ^{43}Ca and ^{135}Ba were not quantified, but observed during analysis, as to identify possible gangue mineral inclusions within the measured spot. Although ^{74}Ge is considered the most conveniant germanium mass when analyzing sphalerites (Belissont et al. 2014), ^{72}Ge and ^{73}Ge were also analyzed in order

to reduce a possible polyatomic interference of argon-sulfur compounds with germanium isotopes. To obtain satisfactory results, a spot size of 50 μm was applied. The laser was set to a fluency of 2-3J/cm^2 with a repetition rate of 10Hz. The set up works with helium as a carrier gas, exhibiting a flow rate of 0,75l/min. Background values are acquired for 30 seconds before ablation, while the laser warms up, succeeded by 60 seconds of laser ablation data acquisition of the chosen spots. Before every analysis a 30 second wash-out sequence was conducted.

For both sphalerite and pyrite S was used as the internal standard. Additionally, the reference material MUL-ZnS1 (sphalerite matrix-matched reference material, in the form of a sintered pressed powder pellet)(Onuk et al. 2017) was utilized as an external standard. Since MUL-ZnS1 cannot be used to quantify tellurium, gold and mercury isotopes, another external standard (MASS-1) (Wilson et al. 2002) was needed to quantify these elements. In order to amend instrumental drift and to ensure a satisfactory quality of the measurements, analyses of the two reference materials mentioned above were conducted periodically every 20 spots.

Data reduction was executed by the software Iolite 4 (Paton et al. 2011). Limits of detection was obtained by the Howell method, the calculations necessary were done by the Iolite software mentioned above. In additon to spot analyses, LA-ICP-MS was used to produce two element maps of sphalerite textures. These were obtained employing 25 μm line scans, while applying a scan speed of 10$\mu m/s$. The processing of the generated data was done by the "Imaging" application provided by the Iolite 4 software.

5.6. Statistics and diagrams

A correlation matrix was calculated using the complete data set obtained by the LA-ICP-MS spot analyses conducted on sphalerite. For the correlation calculations only elements with more than 70% of data above detection limit were used (arsenic, thallium, germanium, lead, manganese, iron, cadmium, mercury, antimony and silver). If a data set included concentrations below detection limit, half of the detection limit was used instead. To calculate the correlation matrix the function "cor" from the R package "StatDA" was utilized, using the Spearman method. To plot the results the function "corrplot" from the R package "corrplot" (T. Wei and Simko 2021) was used.

For the robust log-transformed principal factor analysis only element data from colloform sphalerite that had less than 50% values below detection limit was used. Values below detection limit were replaced by half of the detection limit. If data was missing, it was replaced by the median value of the data set of the respective color of the sphalerite. A robust covariance matrix was calculated by using the function "covMcd" from the R package "robustbase", for rescaling the function "scale" was used. The principal factor analysis was performed using the function "pfa" from the R package "StatDA". To plot the factor loadings from the loadings matrix the function "loadplot" from the R package "StatDA" was used.

The correlation matrix diagram and the plot showing factor loadings derived from the factor analysis were generated by using R packages. All other diagrams were drawn by using the program OriginPro.

5.7. Ore forming temperature calculations

Using the amounts of gallium, germanium, iron, manganese and indium found in the crystal lattice to calculate the precipitation temperature of sphalerite was proposed Frenzel et al. 2016; Frenzel et al. 2017. This geothermometer was utilized in this study in attempt of calculating the precipitation temperatures of the sphalerite found in Raibl. The following formulas (Frenzel et al. 2016; Frenzel et al. 2017) were used:

$$PC1^* = ln(\frac{C_{Ga}^{0.22} \cdot C_{Ge}^{0.22}}{C_{Fe}^{0.37} \cdot C_{Mn}^{0.20} \cdot C_{In}^{0.11}})$$

$$T(°C) = -(54.4 \pm 7.3) \cdot PC1^* + (208 \pm 10)$$

Note: Concentrations of gallium, germanium, indium and manganese are given in $\frac{mg}{kg}$ and the concentration of iron is given in wt.%. Data sets with missing values were not used for this calculations, values below detection limit were replaced by half of the detection limit.

6. Results

6.1. Mineralogy of primary ore samples from Raibl

The primary ore minerals found in the samples are sphalerite and galena. Sphalerite shows five color varieties (brown, red, yellow, green and grey). The textural varieties are described below (see section 6.2). Pyrite could be identified as additional primary ore mineral. Although the existence of wurtzite and marcasite within the Raibl deposit has been reported in literature before (e.g. Jicha 1951), only sphalerite and pyrite could be identified in the samples using microscopy and Raman spectroscopy. Wurtzite or marcasite was not found. The Raman spectra of the measured sphalerite, a comparison spectrum of sphalerite provided by the RRUFF database and a comparison spectrum of wurtzite also provided by the RRUFF database can be seen in figure 6.1. The measured spectrum differs significantly from the wurtzite spectrum. Based off our limited sample set and data set, we cannot completely discredit the presence of wurtzite and marcasite in the Raibl deposit.
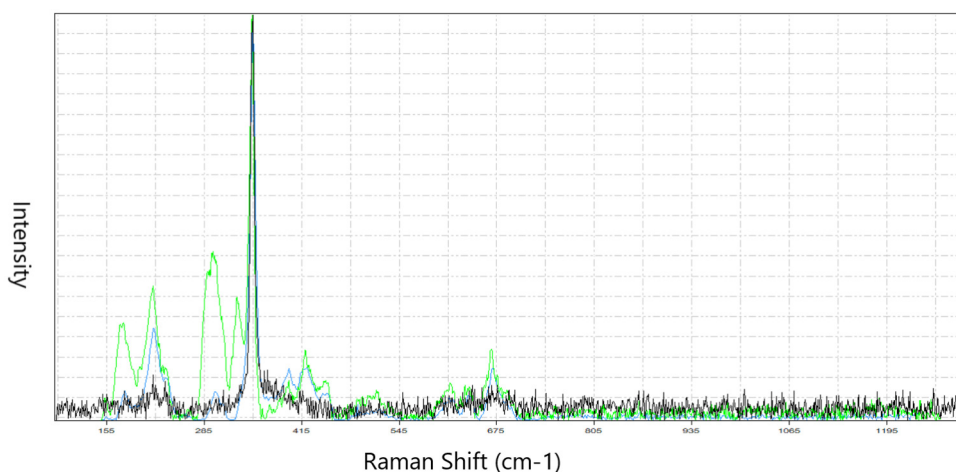
Figure 6.1.: Raman spectra of sphalerite and wurtzite; in black - measured spectrum; in blue - spectrum of sphalerite proposed by CrystalSleuth (RRUFF identification code: R040136; calculated fit: 87%); in green - spectrum of wurtzite proposed by CrystalSleuth (RRUFF identification code: R060181; calculated fit: 72%)

Secondary ore minerals are less common in the samples. Zinc-carbonate (smithsonite), lead-sulfate (anglesite), lead-carbonate (cerussite) could be distinguished. A potential zinc-sulfate was found, but its identification remains doubtful.

The gangue consists of mostly dolomite, which is sometimes accompanied by barite. Quartz was found as gangue mineral in two samples. Calcite is rare.

6.2. Description of textures

6.2.1. Colloform sphalerite

Sphalerite occurs in the form of schalenblende (colloform sphalerite) in most samples. Schalenblende is commonly considered a mixture of sulfides, mostly sphalerite, showing reniform and botryoidal textures. The sphalerite is cryptocrystalline and appears as fine rhythmic bands resembling shells, giving schalenblende (shell sphalerite) its name (c.f. Posepny (1873); Schroll (1953b)). The bands can appear in direct succession, but gaps of gangue minerals between the bands are also possible. The bands can vary in width but also in color. Both continuously straight and irregular bands can be found.

In the colloform samples examined in the present study, bands of sphalerite exhibiting lighter colors (yellow, light brown, beige) can be seen as the early phase of sphalerite. If excited by UV-light these sphalerites show yellow, orange and brown colors. The next sphalerite phase is present as dark colored bands (red, shades of dark brown). After excitation with UV-light, this sphalerite phase exhibits yellow, light brown, dark brown and black colors. Both light and dark sphalerite are partially replaced by galena bands or strings of euhedral to subhedral galena grains. In some cases, galena was also remobilized after deposition (figure 6.3). A third sphalerite phase showing varying green shades is associated with the galena. After excitation wit UV-light green sphalerite shows different shades of brown and yellow. The three phases of sphalerite can be seen in figure 6.2.
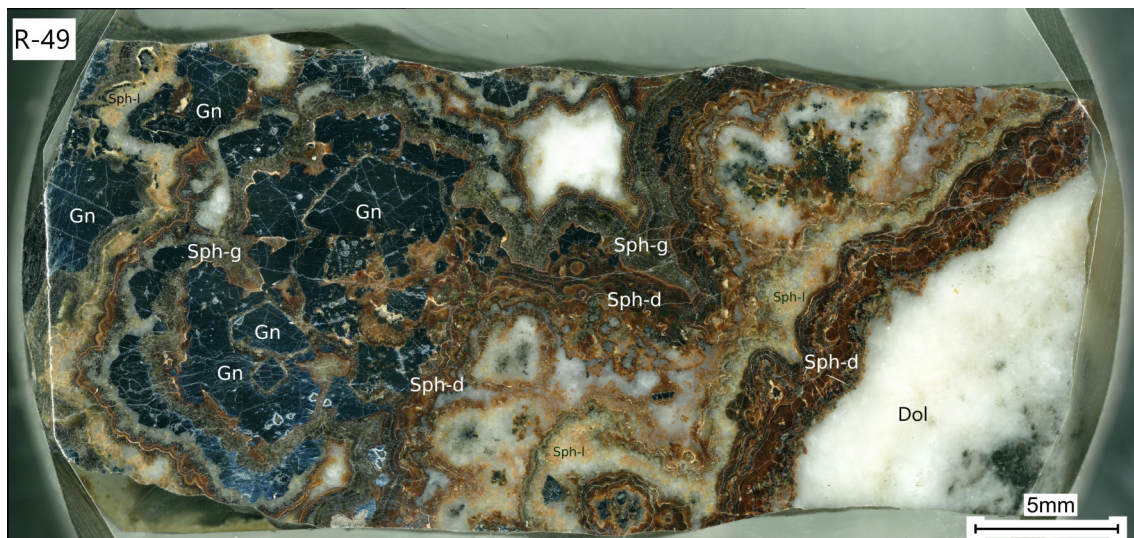
Figure 6.2.: Sample R-49 showing the three color varieties of colloform sphalerite; sph-l=light colored sphalerite; sph-d=dark colored sphalerite; sph-g = green sphalerite

Pyrite occurs as the outermost bands of colloform sphalerite textures or is associated with the first two phases of sphalerite. Pyrite is also overgrown by galena. Sometimes pyrite is missing completely from a sample.

Barite forms the last phase, appearing as tabular or bundled grains separating sphalerite bands. Smithsonite sometimes appears as veins, cutting through all types of sphalerites (figure 6.4).
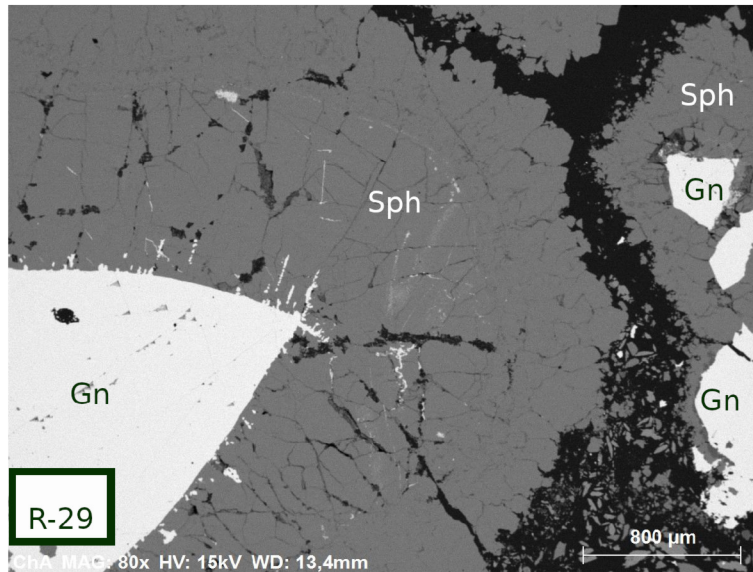
Figure 6.3.: Lead mobilisates in sphalerite; Back-scattered Electron detector (BSE) image
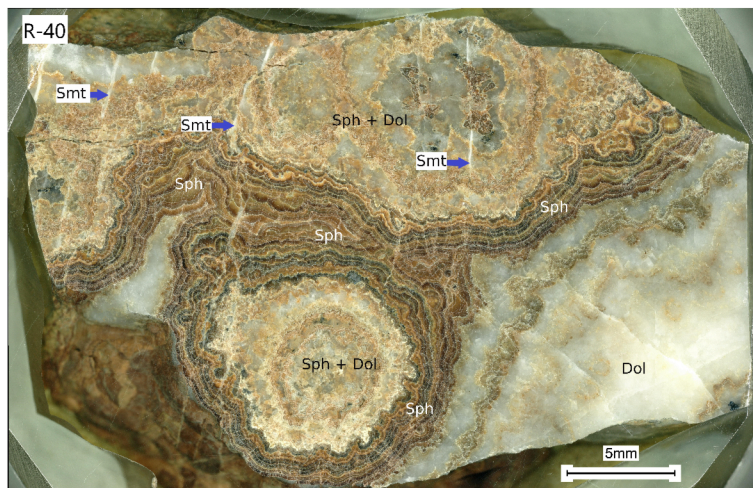
Figure 6.4.: Smithsonite veins cutting through sphalerite are marked with blue arrows

Some colloform samples show only part of the mineral succession. Sample R-59 contains only a few galena grain and the green sphalerite is completely missing. The sample is dominated by bands showing different shades of brown and large barite grains breaking up the succession of sphalerite bands (figure 6.5).

Figure 6.5.: Sample R59, showing sphalerite bands of varying shades of brown, separated by large barite grains

Sample 63A also shows colloform textures, but differs from the other colloform samples. The first phase is a light grey sphalerite, followed by a dark brown and reddish brown sphalerite band. These sphalerites are overgrown by dendritic galena grains. The reddish brown sphalerite is followed by green, yellow and finally dark brown sphalerite bands (figure 6.6). Green sphalerite sometimes blends into yellow sphalerite. The outer dark brown sphalerite is succeeded by a final pyrite band.

Figure 6.6.: Sample R-63A, grey sphalerite is marked with blue arrows

Sometimes the colloform sphalerite is brecciated. Sample R-16 is a breccia showing dark clasts of ore (colloform sphalerite, galena, pyrite) and dark clasts of other minerals (fluorite, fluorapatite, sphalerite, pyrite, barite, dolomite) in a white matrix consisting of dolomite, barite and calcite (figure 6.7). In sample R-29, the colloform sphalerite clasts are surrounded by a matrix consisting of dolomite, barite, galena and grey sphalerite. The grey sphalerite turns into a bright yellow, if excited by UV-light.
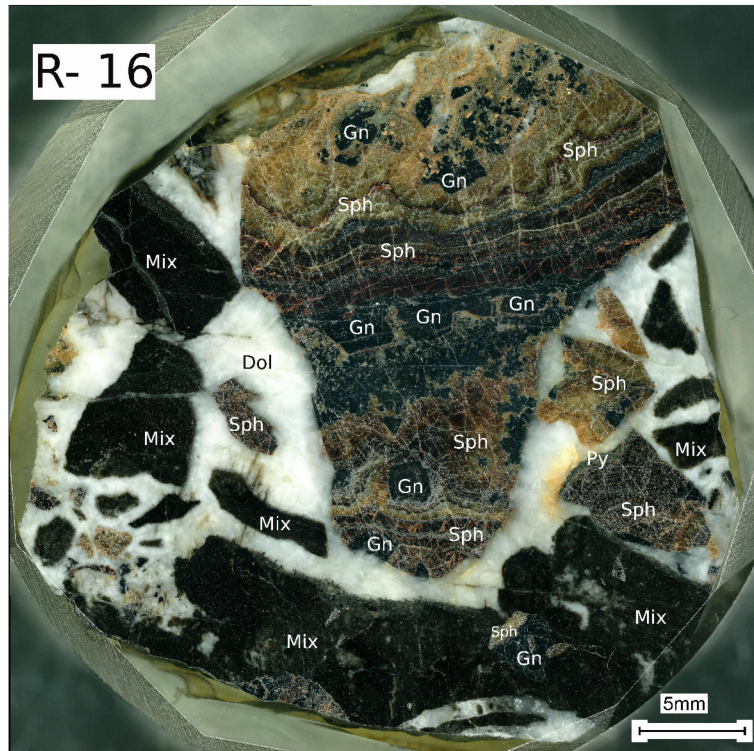
Figure 6.7.: Sample R-16, breccia containing clasts of ore (marked with respective minerals abbreviations) and clasts consisting of a mixture of various minerals (marked as mix) in a white matrix consisting of dolomite, barite and calcite

Sphalerite and barite may occur as alternating concentric circles within the light-brown sphalerite color variety in some samples (e.g. sample R-16; figure 6.8). In other cases, porous bands or rings occur that contain grains of an unidentified mineral, which could be zinc-sulfate (e.g. sample 17A; figure 6.9). It is possible that the porous structures were previously filled with this zinc-sulfate, which may have been destroyed during preparation of the sample due to its softness and water solubility.
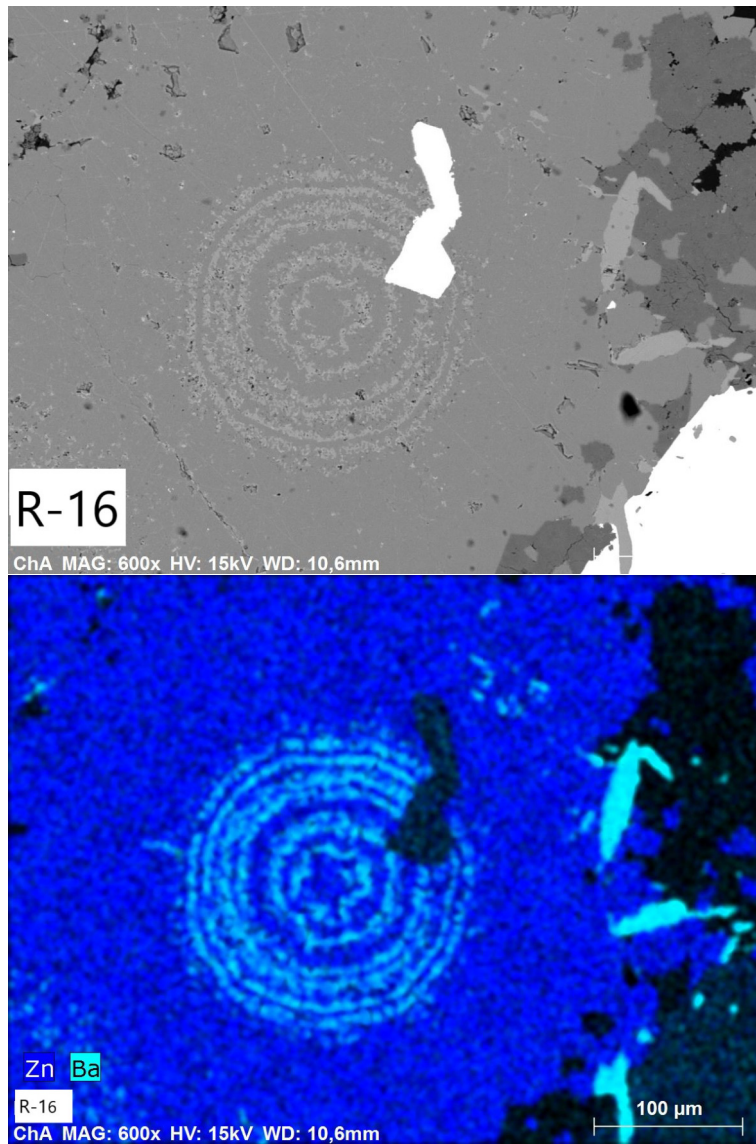
Figure 6.8.: Concentric circles of alternating sphalerite and barite in sample R-16; top: BSE image; bottom: SEM-EDS element distribution map showing the distribution of zinc and barium in the same section of the sample
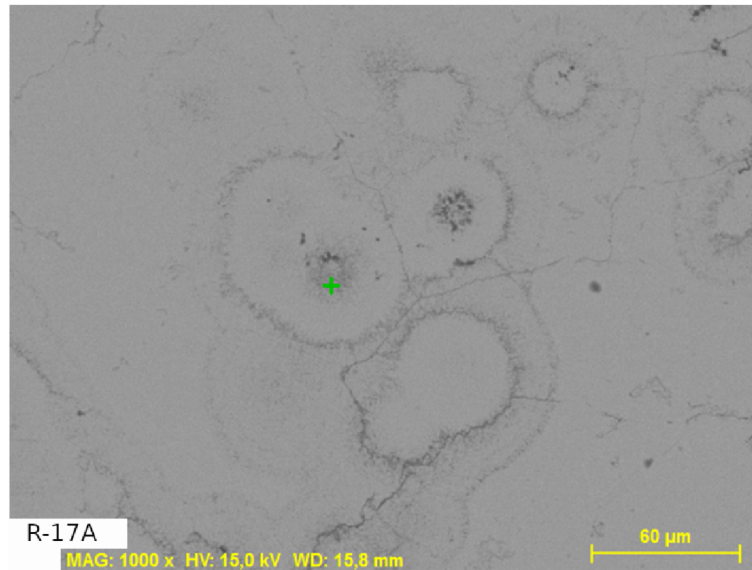
Figure 6.9.: Location of a possible zinc-sulfate; identification doubtful; BSE image

Apart from the zinc-carbonate smithsonite, other alteration minerals such as the lead-carbonate cerussite and the lead-sulfate anglesite can also occur in colloform samples. Accessory grains of calcite are found in some samples.

6.2.2. Agglomerated sphalerite

Some sphalerites do not form bands, but occur as individual, sometimes rounded grains which are densely packed. Two types of this agglomerated sphalerite (type A and B) were found in the samples used in the present study.

Agglomerated sphalerite - type A

Grey anhedral sphalerite is overgrown by anhedral to subhedral pyrite (figure 6.10 C) and galena. Both pyrite and galena sometimes form bands in the host rock. These bands may have been banded sphalerite textures before, that were replaced by pyrite and galena (figure 6.10 A). The pyrite shows colorful tarnish and intricate zoning. The sphalerite of this textural variety is often significantly porous. If it is excited by UV light, it shows variations of black, dark brown or orange (figure 6.10 B). The gangue consists of quartz and barite. This textural variety of sphalerite is not accompanied by any other type.
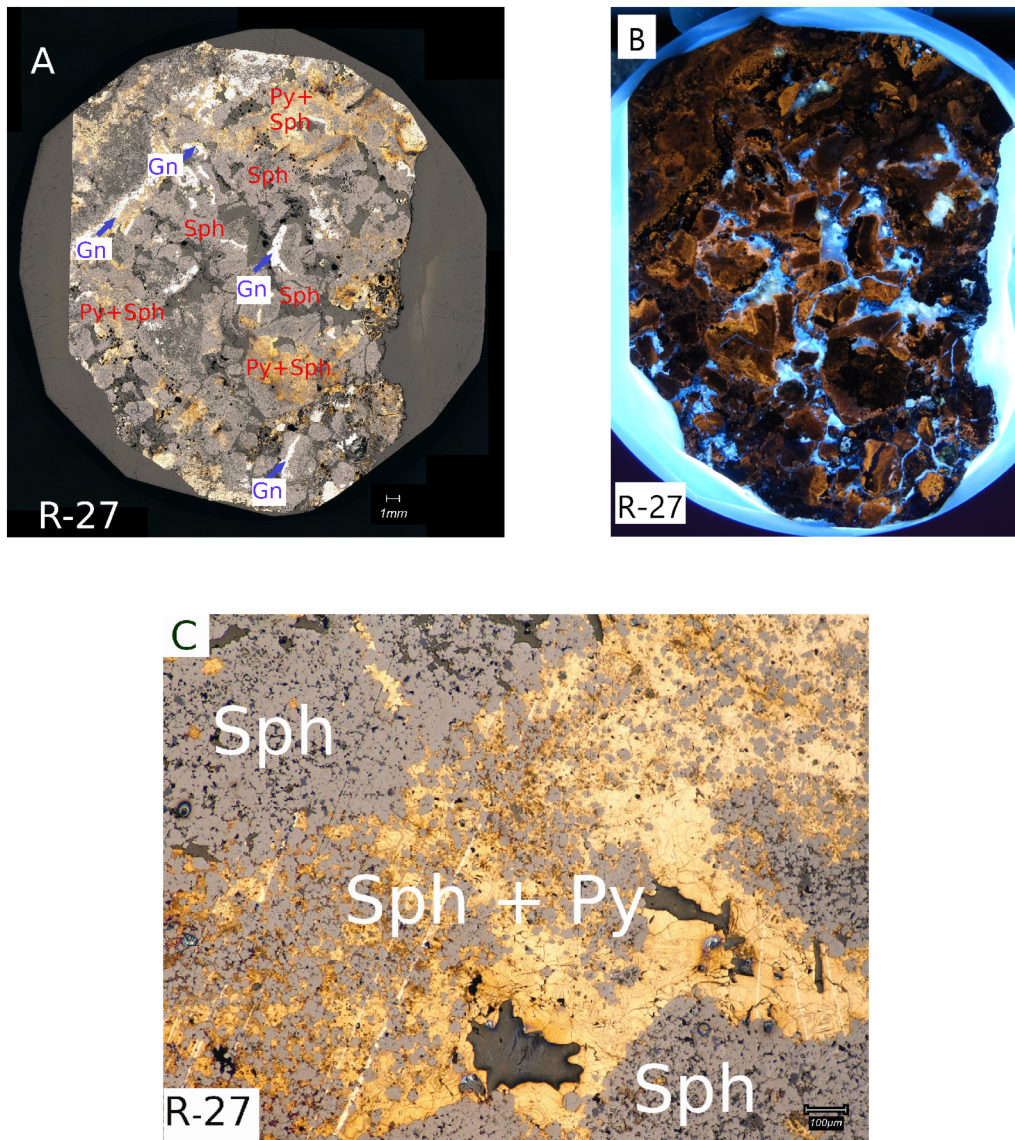
Figure 6.10.: Sample R-27; A: the whole sample R-27 under reflected light, some galena and pyrite bands are marked with blue arrows; B: the same sample under UV-light, sphalerite exhibits black, dark brown and orange colors; C: pyrite overgrows porous sphalerite, zoning within the pyrite and several LA-ICP-MS spots are visible

Agglomerated sphalerite - type B

Agglomerated sphalerite type B resembles colloform sphalerite in color. Rounded sphalerite grains exhibiting light and dark brown colors are overgrown by anhedral galena. If excited by UV-light, light brown sphalerite shows yellow and reddish brown colors, whereas darker varieties of brown sphalerite exhibit dark brown colors. The sphalerite grains can form band-like structures differentiated by color, however, grains within these bands are still visible, unlike in colloform textures (figure 6.11). Galena can also form bands (figure 6.11). Galena grains can be accompanied by green sphalerite, which diffusely overgrows brown sphalerite. Green sphalerite shows dark brown colors, if excited by UV-light. Sometimes single sphalerite grains show colloform textures (figure 6.12). Pyrite is missing completely from this textural variety. The gangue consists of dolomite and barite.
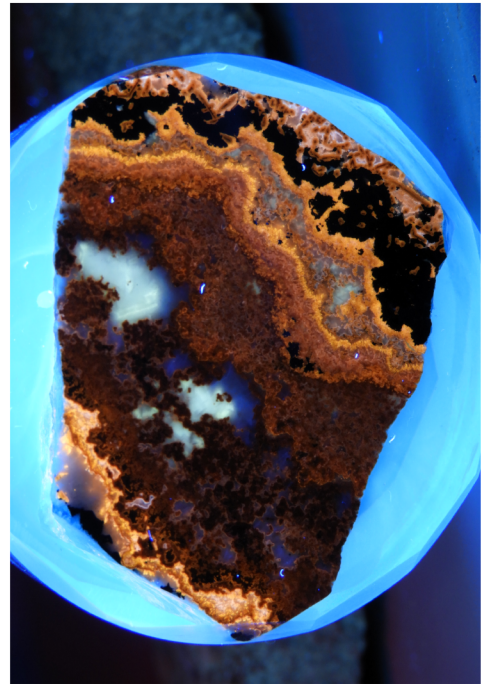
Figure 6.11.: Sample R-32, showing agglomerated sphalerite textures, but also band-like structures of sphalerite and galena (left: normal colors, right: colors after excitation with UV-light)

Figure 6.12.: Sphalerite grains with colloform textures, partially replaced by barite; galena is present as small elongated grains

The sphalerite grains are often intergrown with barite, partially replacing the colloform texture found in sphalerite grains partially (figure 6.12). Additionally, concentric rings can occur in light brown sphalerite. They consist of alternating sphalerite and barite rings, surrounding a small galena grain in the center (figure 6.13).
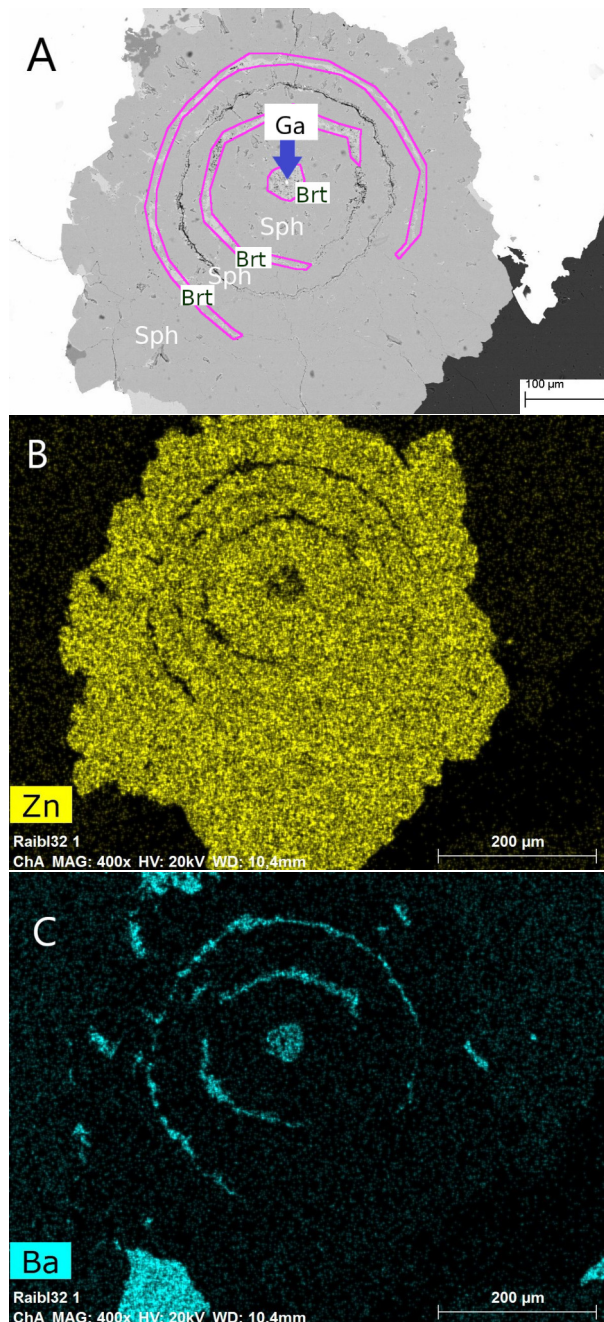
Figure 6.13.: Concentric rings of sphalerite and barite, surrounding a galena grain; A: BSE image, barite is encircled in pink, the galena grain in the center is marked by a blue arrow; B: SEM-EDS element distribution map showing the distribution of zinc in the same section of the sample; C: SEM-EDS element distribution map showing the distribution of barium in the same section of the sample

Unlike agglomerated sphalerite type A, this textural variety can occur next to colloform varieties of sphalerite (figure 6.14). This may indicate a genetic relation of these textural varieties.
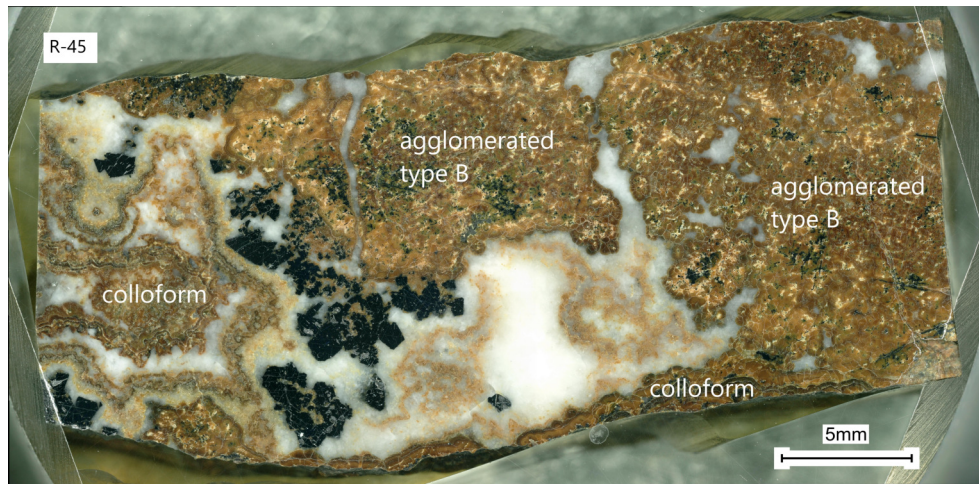
Figure 6.14.: Agglomerated textures (type B) and colloform textures can occur together

6.2.3. Tubular ore

Macroscopically, tubular ore differs from colloform ore, however, microscopically some similarities can be seen. Compared to samples containing colloform sphalerite, galena is more abundant in the tubular samples and its subhedral grains form rings if the sample is observed two-dimensionally (figure 6.15). These rings form the galena tubes in the three-dimensional sample. The interior of the rings, the tube filling in the three-dimensional sample, consists of porous light brown sphalerite intergrown with dolomite and sometimes barite.
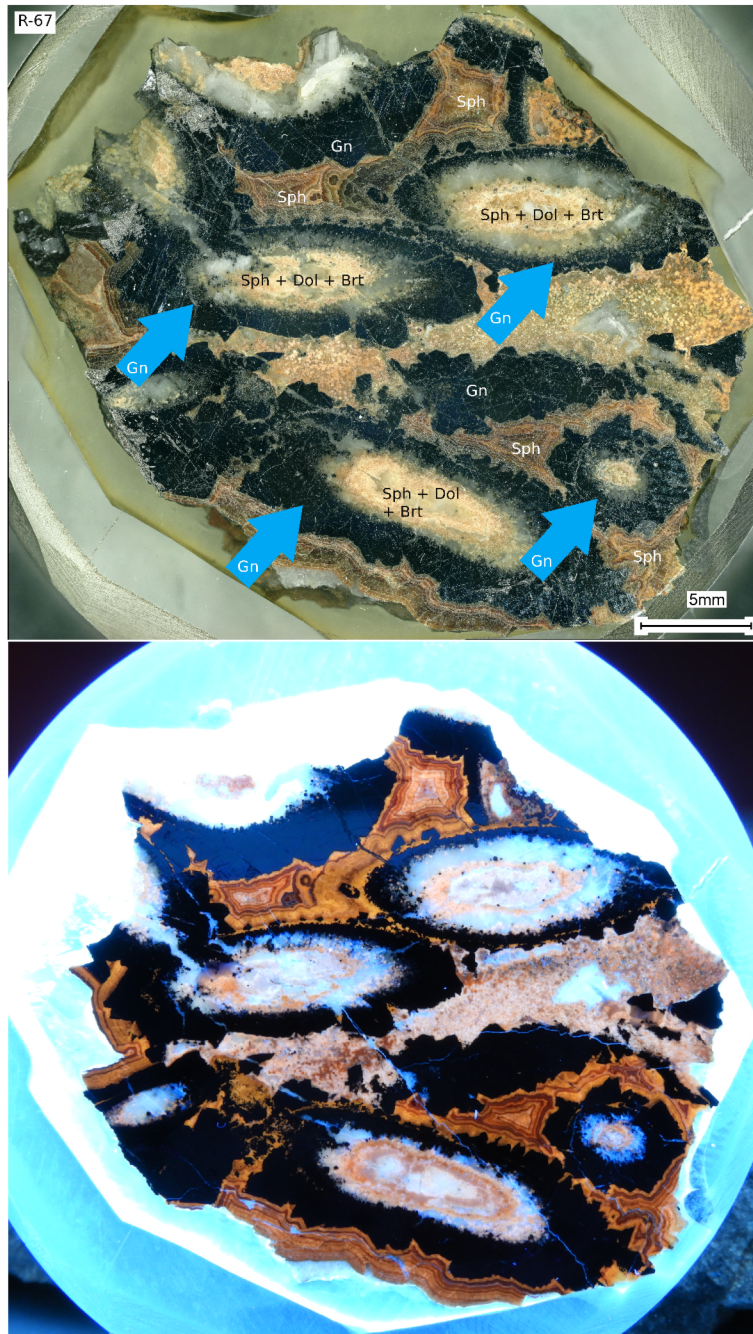
Figure 6.15.: Tubular ore; top: picture taken with normal light, rings of galena are marked with blue arrows; bottom: picture taken under UV-light

Tubular ore samples show a similar pattern of mineral succession as colloform sphalerite. The light brown and yellow colored sphalerite in the interior of the tube, as well as the dark brown banded sphalerite outside the galena tube are overgrown by galena. Galena is associated with banded dark green sphalerite, which could be interpreted as a sign of alteration (figure 6.15). Pyrite occurs in two generations. The earlier generation forms euhedral to subhedral grains, which sometimes are present as globular, slightly colloform grains (figure 6.16). This pyrite generation sometimes coexists with the light sphalerite, but is overgrown by the light sphalerite, as well as the galena, in some cases. The later pyrite generation occurs as a vein that cuts through the earlier galena and sphalerite. The last phase of mineralization are secondary minerals which were formed by alteration of the

primary ore. Anglesite, cerussite and smithsonite were found in tubular ore samples as alteration rims or crack fillings. This succession pattern cannot be observed in its entirety in all samples.
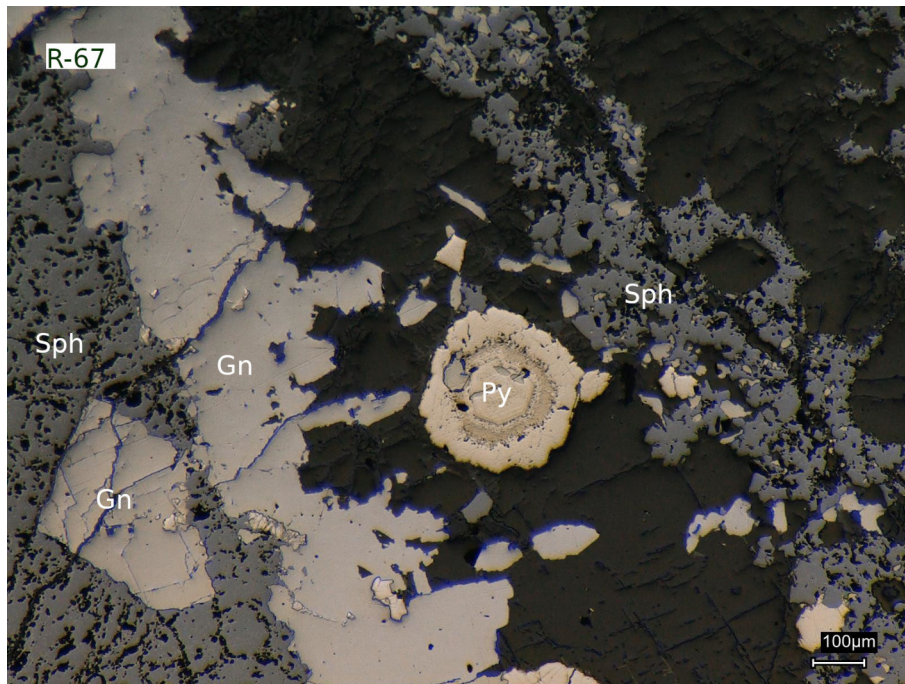
Figure 6.16.: Globular pyrite grain exhibiting colloform textures

Under UV-light, the light brown sphalerite shows white, beige and light orange colors. The dark brown and dark green exhibits different shades of brown and orange, if excited by UV-light.

Tubular ore shows concentric cavities within the light-brown sphalerite. These cavities may have been filled by an unknown mineral lost due to the preparation method. Some rings have been partially replaced by galena (figure 6.17).
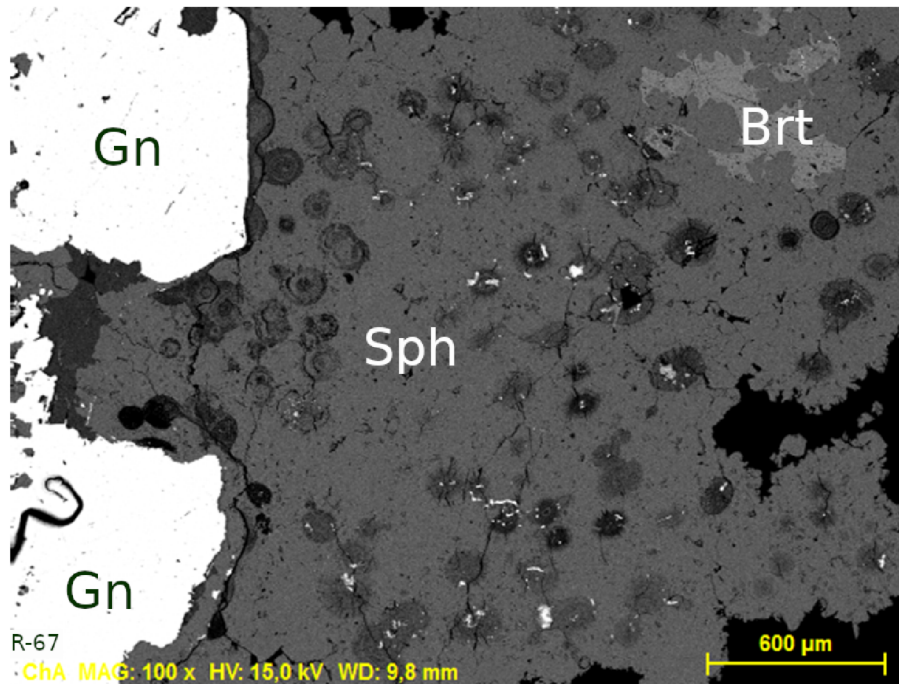
Figure 6.17.: Concentric circles within the light sphalerite, partially filled by galena; sample R-67; BSE image

6.2.4. Layered ore

Layers of ore minerals intercalated with layers of gangue define this texture (figure 6.18). The host rock consists of quartz and dolomitic layers. The dolomitic layers are partially replaced by galena, which is subsequently replaced by pyrite. Both ore minerals are overgrown by sphalerite, which occurs in the sample in two different forms.

Grey sphalerite is present in the samples as anhedral, rounded grains, sometimes exhibiting a greenish tint. If excited by UV light this sphalerite shows beige-brown luminescence colors. The sphalerite grains form layers, in which they are associated with barite, dolomite and larger quartz grains (marked in figure 6.18 as 4 and 11). But grey sphalerite is also found in and near dolomitic or baritic veins within the quartz layers (marked in figure 6.18 as 2 and 10) and overgrowing other sulfide ore minerals (galena, pyrite)(seen in figure 6.18 as number 12). The brown sphalerite band/layer occurs at the contact between the barite-dolomite layer and the quartz layer (marked in figure 6.18 as 9). The sphalerite itself occurs as tabular grains, within the barite-dolomite layer. The color ranges from light to greenish brown. Under UV light this sphalerite shows yellow-brown luminescence.

One dark layer consists of a mixture of dolomite and quartz with agglomerated fluorapatite, sphalerite and pyrite (marked in figure 6.18 as 1). Additionally, calcite was found in veins in quartz. Fluorite, an unidentified zinc-sulfate, unidentified iron-oxide phase and an unidentified phase bearing aluminum and silicon were found as accessory minerals. The phase containing aluminum and silicon may be kaolinite.
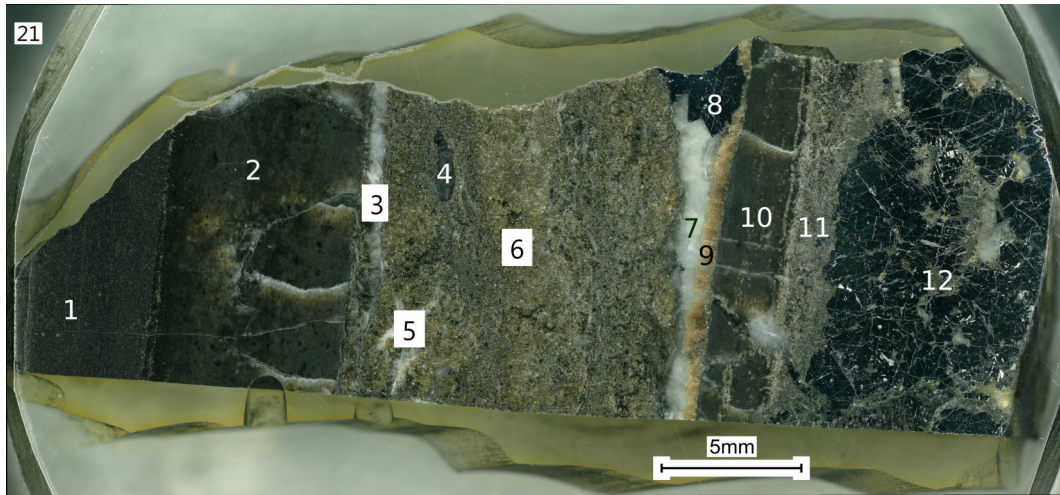
Figure 6.18.: Sample R-21, layered ore; 1: dark layer consisting of dolomite, quartz, sphalerite, pyrite, fluorapatite; 2: quartz with veins; 3: barite; 4: quartz; 5: barite; 6: grey sphalerite; 7: mixture of dolomite and barite; 8: galena; 9: brown sphalerite; 10: quartz with veins; 11: grey sphalerite; 12: grey sphalerite, galena and pyrite

6.2.5. Fern ore

Dark brown, rounded sphalerite, which encompasses subhedral to anhedral galena overgrowing the sphalerite, gives this type its iconic look resembling fern leaves growing on a white background. Under UV light this sphalerite shows a dark brown luminescence. In some sphalerite grains a slight banding can be noticed. Galena can also occur on its own as "dendritic" grains. The sphalerite shows significant alteration to light brown smithsonite at its margins (figure 6.19 A), in some cases the sphalerite has been completely turned into smithsonite (figure 6.19 B), while the galena in the middle remains. SEM analysis revealed that the sphalerite shows a significant number of rounded holes.

Smithsonite also exhibits pseudomorphosis, as it sometimes seems to imitate the banded texture of the sphalerite it replaced (figure 6.19 C). The galena seems to be mostly unaltered, sometimes exhibiting holes. The gangue consists of grey, subhedral to anhedral dolomite clasts in a white anhedral smithsonite matrix. Red streaks within the white smithsonite were found to contain small amounts of iron. Calcite can occur as an accessory mineral.
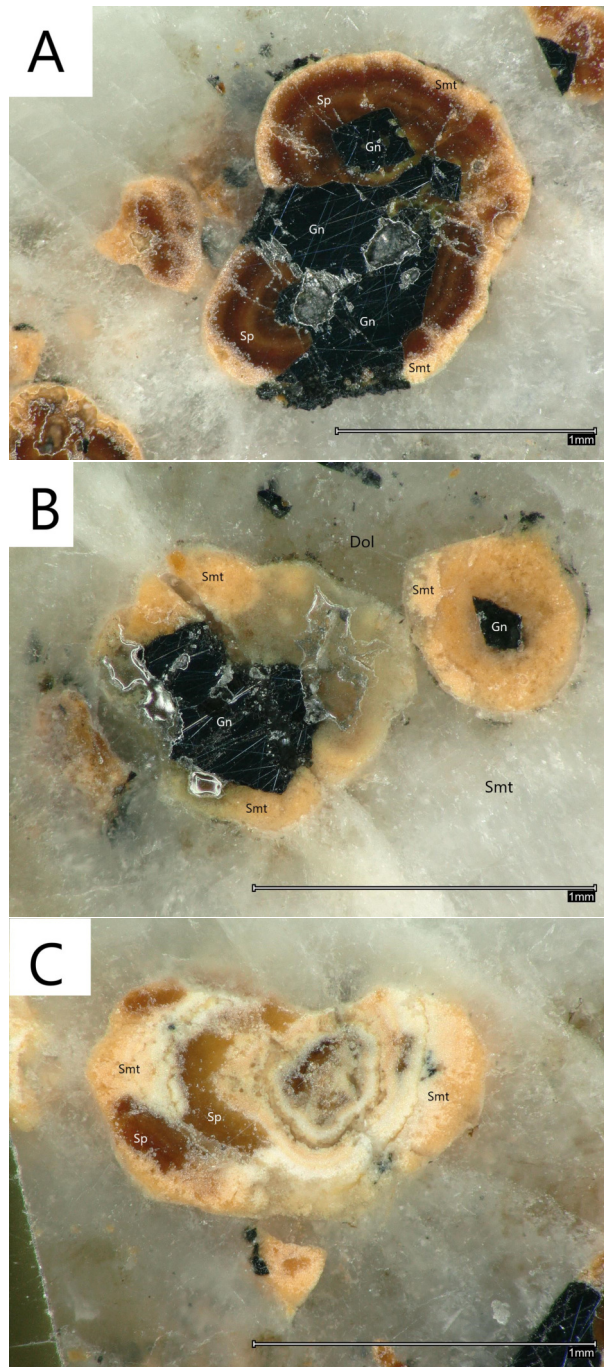
Figure 6.19.: Sections of the sample R-36; progressive alteration of sphalerite to smithsonite - A: Minor alteration of sphalerite to smithsonite along rims; B: complete replacement of sphalerite by smithsonite; C: pseudomorphosis, smithsonite exhibits similar structures to colloform sphalerite

6.2.6. Summary of petrographic characteristics

The properties of each textural type of sphalerite described in section 6.2 are summarized in the table 6.1.

texture	color	UV luminescence color	associated minerals	gangue	samples
colloform	light brown, yellow	yellow, orange, brown	galena	dolomite, barite	R-10, R-16, R-17A/B, R-24, R-28, R-40, R-45, R-49, R-59, R-63A/B
	dark brown, reddish brown	yellow, light brown, dark brown, black	galena, pyrite	dolomite, barite	R-10, R-16, R-17A/B, R-24, R-28, R-29, R-40, R-45, R-49, R-59, R-63A/B
	green	brown, yellow	galena	dolomite, barite	R-10, R-16, R-17A/B, R-24, R-28, R-29, R-40, R-49, R-59, R-63A/B
agglomerated (type A)	grey	black, dark brown, orange	galena, pyrite	barite, quartz	R-27
agglomerated (type B)	light brown	yellow, reddish brown	galena	dolomite, barite	R-32, R-45
	dark brown	dark brown	galena	dolomite, brown	R-32, R-45
	green	dark brown	galena	dolomite, barite	R-45
tubular	light brown	white, beige, light orange	galena, pyrite	dolomite, barite	R-67, RoeA
	dark brown	brown, orange	galena	dolomite, barite	R-67, RoeA
	dark green	brown, orange	galena	dolomite, barite	R-67
layered	greenish grey	beige-brown	galena, pyrite	quartz, dolomite, barite	R-21
	light brown, greenish brown	yellow brown		quartz, dolomite, barite	R-20, R21
fern ore	dark brown	dark brown	galena, smithsonite	dolomite, smithsonite	R-36

Table 6.1.: Petrographic characteristics of the sphalerite textures described in section 6.2

6.3. Chemistry of sphalerite from the Raibl deposit

LA-ICP-MS analyses reveal that sphalerite contains significant amounts of iron (median of 267ppm), germanium (median of 168ppm), arsenic (median of 799ppm), cadmium (median of 1593ppm), thallium (median of 132ppm) and lead (median of 2477ppm) (for the statistical parameters of the whole data set see table 6.2). Additionally, manganese, copper, gallium, selenium, tin, antimony, mercury have been found in various samples. Vanadium, chromium, cobalt, molybdenum, silver, indium, tellurium, gold and bismuth are found in insignificant concentrations or were below detection limit. Iron, germanium, arsenic, cadmium, antimony, thallium and lead contents vary significantly between samples (tables 6.3, 6.4 and 6.5). Manganese, copper, gallium, silver, tin, mercury, selenium, vanadium, chromium, cobalt, molybdenum, indium, tellurium, gold and bismuth contents remain relatively stable within the data set showing some outliers (tables 6.3, 6.4 and 6.5).

Element	Min	Max	Med	Mean	Q10	Q90	S.D.	%> LOD
V	0.02	3.12	0.07	0.15	0.03	0.17	0.44	10.6
Cr	0.41	4.07	0.90	1.05	0.54	1.54	0.66	8.15
Mn	0.53	13.4	5.66	7.63	1.16	15.1	9.78	95.8
Fe	33.4	6973	267	498	88.3	1191	722	96.0
Co	0.02	16.4	0.10	0.48	0.04	0.21	2.46	9.69
Ni	0.23	4.83	1.07	1.60	0.67	3.26	1.21	7.05
Cu	0.52	321	3.84	33.7	1.10	133	71.6	26.9
Ga	0.04	89.9	0.50	3.04	0.16	5.15	10.3	32.6
Ge	6.32	1524	168	246	25.4	575	263	100
As	4.49	10618	799	1492	57.1	3599	1935	99.8
Se	3.61	15.3	6.55	7.61	4.76	13.8	3.28	8.37
Mo	0.08	3.33	0.21	0.66	0.13	1.39	0.98	2.42
Ag	0.29	6.96	0.46	0.64	0.38	0.78	0.81	82.2
Cd	277	7640	1593	2027	646	4203	1438	100
In	0.03	0.06	0.05	0.05	0.04	0.06	0.01	2.42
Sn	0.75	20.2	5.62	5.30	1.85	8.19	2.55	69.2
Sb	0.06	1536	11.1	85.3	0.33	275	180	94.9
Te	0.19	0.19	0.19	0.19	0.19	0.19	0.19	0.22
Au	0.00	0.00	n.a.	n.a.	n.a.	n.a.	n.a.	0.00
Hg	5.23	108	13.0	14.9	7.17	22.6	10.1	97.6
Tl	1.75	2324	132	266	16.5	622	367	99.6
Pb	62	39955	2477	3429	501	7110	3909	97.4
Bi	0.01	0.05	0.01	0.02	0.01	0.03	0.01	3.08

Table 6.2.: Statistical parameters for the complete LA-ICP-MS data set of sphalerite from Raibl (N=454), Min=Minimum, Max=Maximum, Med=Median, Mean=Arithmetic mean, Q10 and Q90 = tenth and ninetieth percentile, S.D. = Standard Deviation, %> LOD = percentage of values above load of detection, n.a.=not applicable due to missing data; numbers are given in $\mu g/g$

sample		V	Cr	Mn	Fe	Co	Ni	Cu	Ga	Ge	As	Se	Mo	Ag	Cd	In	Sn	Sb	Te	Au	Hg	Tl	Pb	Bi
R-10	min	0.03	0.49	1.06	73.5	0.03	0.31	0.90	0.07	21.3	36.1	5.05	0.13	0.36	1368	0.00	1.31	2.91	0.00	0.00	10.4	13.0	466	0.01
(N=25)	max	0.11	0.92	21.1	492	0.05	0.66	22.5	0.26	309	1549	8.99	0.13	0.78	5182	0.00	2.56	48.7	0.00	0.00	35.5	277	4591	0.01
	med	0.06	0.54	2.36	182	0.04	0.48	1.62	0.13	113	429	5.81	0.13	0.43	2234	n.a.	1.73	16.4	n.a.	n.a.	19.7	60.7	2397	0.01
	mean	0.06	0.65	6.28	190	0.04	0.48	4.23	0.15	122	477	6.62	0.13	0.48	2615	n.a.	1.73	20.7	n.a.	n.a.	21.0	85.0	2103	0.01
	S.D.	0.03	0.24	6.68	113	0.01	0.25	6.83	0.07	82.4	415	2.09	n.a.	0.11	1075	n.a.	0.37	14.4	n.a.	n.a.	7.15	76.9	1187	0.00
	%> LOD	28.0	12.0	76.0	96.0	28.0	8.00	68.0	24.0	100	100	12.0	4.00	100	100	0.00	40.0	96.0	0.00	0.00	96.0	100	92.0	12.0
R-16	min	0.05	0.62	1.02	75.8	0.10	0.80	1.16	0.19	9.89	22.6	5.29	0.08	0.36	277	0.04	4.37	23.1	0.00	0.00	5.69	8.37	362	0.00
(N=35)	max	0.08	1.06	58.5	3564	16.4	1.83	13.5	89.9	1524	10618	7.57	0.13	1.07	7640	0.06	7.45	1536	0.00	0.00	14.6	2324	39955	0.00
	med	0.06	0.77	5.79	1046	0.13	0.83	4.71	3.38	494	2111	7.15	0.11	0.52	2899	0.05	5.65	477	n.a.	n.a.	8.95	275	6457	n.a.
	mean	0.06	0.79	15.3	1073	4.19	1.05	5.78	11.8	558	3729	6.84	0.11	0.59	2807	0.05	5.90	493	n.a.	n.a.	9.92	680	8042	n.a.
	S.D.	0.02	0.15	17.9	981	8.14	0.38	4.31	21.6	516	3893	0.90	0.04	0.19	2035	0.01	0.78	313	n.a.	n.a.	2.37	790	8936	n.a.
	%> LOD	5.71	20.0	100	97.1	11.4	20.0	45.7	80.0	100	100	14.3	5.71	94.3	100	5.71	100	100	0.00	0.00	100	100	100	0.00
R-17A	min	0.00	1.12	1.24	69.6	0.00	0.00	0.00	0.20	13.9	51.2	0.00	0.00	0.32	1279	0.00	3.49	0.63	0.00	0.00	7.02	15.3	406	0.00
(N=23)	max	0.00	1.12	11.6	1419	0.00	0.00	0.00	9.75	678	3957	0.00	0.00	0.53	5081	0.00	9.42	23.5	0.00	0.00	16.2	628	6811	0.00
	med	n.a.	1.12	5.15	257	n.a.	n.a.	n.a.	0.86	99.7	391	n.a.	n.a.	0.45	2112	n.a.	4.98	6.99	n.a.	n.a.	9.36	91.3	1307	n.a.
	mean	n.a.	1.12	4.96	316	n.a.	n.a.	n.a.	1.88	171	888	n.a.	n.a.	0.44	2208	n.a.	5.65	9.61	n.a.	n.a.	9.77	164	2180	n.a.
	S.D.	n.a.	n.a.	3.28	292	n.a.	n.a.	n.a.	2.77	178	985	n.a.	n.a.	0.07	896	n.a.	2.07	7.48	n.a.	n.a.	1.92	156	1738	n.a.
	%> LOD	0.00	4.35	95.7	100	0.00	0.00	0.00	69.6	100	100	0.00	0.00	56.5	100	0.00	43.5	95.7	0.00	0.00	100	100	100	0.00
R-21	min	0.05	0.00	0.06	45.8	0.00	0.00	1.03	0.16	6.32	9.68	0.00	0.00	0.42	3967	0.00	0.00	28.3	0.00	0.00	11.2	2.13	180	0.00
(N=14)	max	0.28	0.00	1.54	104	0.00	0.00	4.32	1.52	78.5	67.6	0.00	0.00	0.69	7062	0.00	0.00	230	0.00	0.00	33.7	19.0	1004	0.00
	med	0.09	n.a.	1.06	54.4	n.a.	n.a.	1.91	0.49	21.3	25.8	n.a.	n.a.	0.51	4927	n.a.	n.a.	59.5	n.a.	n.a.	13.2	10.4	595	n.a.
	mean	0.12	n.a.	1.02	62.8	n.a.	n.a.	2.17	0.61	30.5	27.7	n.a.	n.a.	0.52	5222	n.a.	n.a.	104	n.a.	n.a.	16.3	10.5	584	n.a.
	S.D.	0.07	n.a.	0.27	19.0	n.a.	n.a.	1.05	0.39	25.6	16.2	n.a.	n.a.	0.08	950	n.a.	n.a.	79.1	n.a.	n.a.	6.80	4.71	300	n.a.
	%> LOD	57.1	0.00	85.7	78.6	0.00	0.00	71.4	78.6	100	100	0.00	0.00	100	100	0.00	0.00	71.4	0.00	0.00	92.9	85.7	100	0.00
R-24	min	0.07	0.72	0.53	33.4	0.04	0.23	1.66	0.05	15.1	33.6	6.48	0.20	0.29	686	0.00	0.75	0.89	0.00	0.00	9.96	8.96	224	0.01
(N=24)	max	0.07	0.89	7.28	1292	0.14	1.30	3.75	0.06	453	2779	7.71	0.21	0.49	6312	0.00	2.30	871	0.00	0.00	22.1	554	4294	0.01
	med	0.07	0.77	2.00	184	0.06	0.96	2.09	0.05	55.6	198	6.62	0.20	0.41	1258	n.a.	1.53	4.78	n.a.	n.a.	13.2	48.8	812	0.01
	mean	0.07	0.79	2.92	417	0.07	0.87	2.44	0.05	144	759	6.94	0.20	0.41	1706	n.a.	1.45	58.1	n.a.	n.a.	14.4	158	1734	0.01
	S.D.	n.a.	0.07	2.18	440	0.04	0.49	0.81	0.00	165	1048	0.67	0.00	0.05	1255	n.a.	0.49	190	n.a.	n.a.	3.21	204	1581	n.a.
	%> LOD	4.17	16.7	100	87.5	20.8	16.7	29.1	8.33	100	100	12.5	8.33	100	100	0.00	62.5	95.8	0.00	0.00	100	100	91.7	4.17
R-27	min	3.12	0.89	3.89	337	0.06	0.77	0.94	0.23	50.5	161	3.82	0.35	0.40	2207	0.00	1.18	30.7	0.00	0.00	17.7	27.7	702	0.01
(N=14)	max	3.12	4.07	8.59	1854	0.31	4.83	8.40	1.36	121	546	7.72	3.33	0.56	4247	0.00	1.70	83.9	0.00	0.00	29.7	122	2934	0.02
	med	3.12	1.42	6.12	842	0.16	2.90	2.87	0.37	83.7	313	5.78	1.20	0.47	2829	n.a.	1.61	46.5	n.a.	n.a.	24.0	61.9	1462	0.01
	mean	3.12	1.76	5.99	937	0.17	2.71	3.45	0.44	84.4	366	5.75	1.52	0.47	2986	n.a.	1.54	50.1	n.a.	n.a.	24.1	66.3	1543	0.01
	S.D.	n.a.	1.08	1.64	429	0.07	1.26	1.89	0.29	22.5	124	1.27	1.28	0.05	567	n.a.	0.18	15.6	n.a.	n.a.	3.96	25.4	643	0.00
	%> LOD	7.14	57.1	100	92.9	92.9	85.7	92.9	92.9	100	92.9	42.9	28.6	92.9	100	0.00	64.3	100	0.00	0.00	100	100	85.7	28.6

Table 6.3.: Minimum and maximum values of the elements, as well as median, mean, standard deviations found in the samples; additionally the percentage of values above detection limit (%> LOD); n.a.=not applicable due to missing data

sample		V	Cr	Mn	Fe	Co	Ni	Cu	Ga	Ge	As	Se	Mo	Ag	Cd	In	Sn	Sb	Te	Au	Hg	Tl	Pb	Bi
R-28	min	0.17	0.73	2.22	87.7	0.07	0.87	0.52	0.14	25.5	87.4	4.02	0.00	0.36	1170	0.00	4.10	22.8	0.00	0.00	10.9	16.4	262	0.01
(N=18)	max	0.28	0.73	19.7	607	0.19	0.87	26.4	5.84	233	1575	8.88	0.00	0.66	3283	0.00	9.31	550	0.00	0.00	38.5	200	3148	0.01
	med	0.23	0.73	7.68	248	0.10	0.87	6.98	0.60	152	746	5.66	n.a.	0.46	1877	n.a.	6.22	114	n.a.	n.a.	16.3	108	2157	0.01
	mean	0.23	0.73	8.74	278	0.12	0.87	9.90	1.28	140	763	6.19	n.a.	0.48	2096	n.a.	6.22	167	n.a.	n.a.	17.8	99.0	1862	0.01
	S.D.	0.08	n.a.	5.60	135	0.05	n.a.	8.87	1.89	75.3	530	2.47	n.a.	0.10	782	n.a.	1.73	163	n.a.	n.a.	6.24	62.8	1025	0.00
	%> LOD	11.1	5.56	94.4	77.8	27.8	5.56	55.6	72.2	100	100	16.7	0.00	100	100	0.00	94.4	100	0.00	0.00	94.4	100	94.4	11.1
R-29	min	0.04	0.00	1.40	79.2	0.18	0.00	19.0	0.36	8.89	13.9	5.85	0.00	0.63	558	0.00	0.00	26.7	0.00	0.00	10.4	3.72	206	0.02
(N=19)	max	0.09	0.00	131	6973	0.22	0.00	321	5.55	833	7394	10.5	0.00	6.96	4216	0.00	0.00	348	0.00	0.00	20.7	1307	12654	0.05
	med	0.06	n.a.	8.46	160	0.19	n.a.	191	2.01	211	1024	8.17	n.a.	3.43	2365	n.a.	n.a.	206	n.a.	n.a.	15.3	170	3143	0.04
	mean	0.06	n.a.	14.8	553	0.20	n.a.	172	2.26	207	1268	8.17	n.a.	3.46	2507	n.a.	n.a.	180	n.a.	n.a.	15.6	220	3741	0.04
	S.D.	0.03	n.a.	30.2	1604	0.22	n.a.	97.9	1.47	185	1625	3.29	n.a.	2.10	1030	n.a.	n.a.	2.2	n.a.	n.a.	2.66	291	3610	0.01
	%> LOD	10.5	0.00	89.5	94.7	15.8	0.00	100	100	100	100	10.5	0.00	94.7	100	0.00	0.00	100	0.00	0.00	100	100	89.5	15.8
R-32	min	0.06	0.00	0.56	64.1	0.00	0.00	0.00	0.00	9.48	27.9	0.00	0.00	0.33	566	0.00	4.57	0.53	0.00	0.00	5.62	10.2	222	0.00
(N=21)	max	0.22	0.00	15.8	1405	0.00	0.00	0.00	0.00	274	2368	0.00	0.00	0.53	6656	0.00	9.16	108	0.00	0.00	11.6	563	4291	0.00
	med	0.09	n.a.	4.74	167	n.a.	n.a.	n.a.	n.a.	98.3	691	n.a.	n.a.	0.44	1936	n.a.	5.91	21.7	n.a.	n.a.	7.18	167	1717	n.a.
	mean	0.11	n.a.	5.18	286	n.a.	n.a.	n.a.	n.a.	110	816	n.a.	n.a.	0.43	2120	n.a.	6.14	28.4	n.a.	n.a.	7.38	204	1799	n.a.
	S.D.	0.07	n.a.	4.19	310	n.a.	n.a.	n.a.	n.a.	86.9	780	n.a.	n.a.	0.06	1351	n.a.	1.14	29.0	n.a.	n.a.	1.32	189	1314	n.a.
	%> LOD	19.1	0.00	95.2	100	0.00	0.00	0.00	0.00	100	100	0.00	0.00	61.9	100	0.00	100	100	0.00	0.00	100	100	100	0.00
R-36	min	0.02	0.48	22.0	377	0.07	0.00	0.55	0.13	1014	7003	5.99	0.00	0.35	796	0.03	5.73	5.47	0.19	0.00	10.9	1340	10800	0.00
(N=7)	max	0.07	0.57	25.6	591	0.07	0.00	0.55	1.85	1072	8491	15.3	0.00	0.46	1009	0.06	17.2	12.2	0.19	0.00	13.5	1726	14393	0.00
	med	0.03	0.54	23.5	510	0.07	n.a.	0.55	0.26	1046	7613	10.6	n.a.	0.42	875	0.05	6.29	8.58	0.19	n.a.	12.5	1519	12600	n.a.
	mean	0.04	0.53	24.0	502	0.07	n.a	0.55	0.54	1042	7696	10.6	n.a.	0.41	908	0.05	9.55	8.51	0.19	n.a.	12.5	1520	12742	n.a.
	S.D.	0.02	0.05	1.54	72.1	n.a.	n.a.	n.a.	0.61	22.3	544	6.56	n.a.	0.04	79.3	0.01	4.73	2.49	n.a.	n.a.	0.79	115	1212	n.a.
	%> LOD	85.7	42.9	100	100	14.3	0.00	14.3	100	100	100	28.6	0.00	100	100	57.1	100	100	14.3	0.00	100	100	100	0.00
R-40	min	0.04	1.09	1.77	135	0.00	0.00	0.00	0.00	34.1	66.4	0.00	0.00	0.30	549	0.00	1.89	0.06	0.00	0.00	5.23	30.3	234	0.00
(N=44)	max	0.04	1.42	18.5	1412	0.00	0.00	0.00	0.00	426	3120	0.00	0.00	0.52	2606	0.00	4.30	1.43	0.00	0.00	9.98	690	7787	0.00
	med	0.04	1.36	6.80	309	n.a.	n.a.	n.a.	n.a.	169	1134	n.a.	n.a.	0.42	1223	n.a.	2.75	0.32	n.a.	n.a.	7.01	213	3793	n.a.
	mean	0.04	1.29	7.27	393	n.a.	n.a.	n.a.	n.a.	183	1251	n.a.	n.a.	0.42	1293	n.a.	2.85	0.50	n.a.	n.a.	7.09	252	3465	n.a.
	S.D.	0.00	0.17	3.94	284	n.a.	n.a.	n.a.	n.a.	98.2	837	n.a.	n.a.	0.06	516	n.a.	0.69	0.43	n.a.	n.a.	0.99	184	1899	n.a.
	% > LOD	9.09	6.82	100	100	0.00	0.00	0.00	0.00	100	100	0.00	0.00	50.0	100	0.00	47.7	84.1	0.00	0.00	100	100	100	0.00
R-45	min	0.07	0.41	1.06	112	0.02	0.00	0.56	0.04	86.3	69.1	3.61	0.14	0.33	430	0.00	1.12	0.29	0.00	0.00	12.0	20.1	163	0.01
(N=36)	max	0.13	0.97	18.2	1589	0.06	0.00	1.01	0.08	546	3594	5.81	0.14	0.61	1933	0.00	7.81	22.4	0.00	0.00	43.3	696	6515	0.01
	med	0.12	0.69	12.0	318	0.05	n.a.	0.61	0.05	278	1546	4.71	0.14	0.47	764	n.a.	2.86	7.48	n.a.	n.a.	16.7	246	3644	0.01
	mean	0.11	0.69	10.7	484	0.05	n.a.	0.73	0.06	275	1604	4.71	0.14	0.46	859	n.a.	3.54	9.17	n.a.	n.a.	17.1	269	3671	0.01
	S.D.	0.04	0.40	3.97	408	0.02	n.a.	0.24	0.02	91.8	629	1.56	n.a.	0.07	310	n.a.	1.95	7.35	n.a.	n.a.	5.50	120	1095	n.a.
	%> LOD	8.33	5.56	91.7	100	14.0	0.00	8.33	11.1	100	100	5.56	2.78	100	100	0.00	80.6	100	0.00	0.00	100	100	100	2.78

Table 6.4.: Minimum and maximum values of the elements, as well as median, mean, standard deviations found in the samples; additionally the percentage of values above detection limit ($\%> LOD$); n.a.=not applicable due to missing data

sample		V	Cr	Mn	Fe	Co	Ni	Cu	Ga	Ge	As	Se	Mo	Ag	Cd	In	Sn	Sb	Te	Au	Hg	Tl	Pb	Bi
R-49	min	0.00	0.93	0.69	91.3	0.00	2.06	0.00	0.16	25.4	79.4	0.00	0.00	0.42	1305	0.05	3.36	0.65	0.00	0.00	6.32	18.0	1043	0.00
(N=20)	max	0.00	1.47	30.7	982	0.00	2.06	0.00	0.23	582	4376	0.00	0.00	0.59	3293	0.06	20.2	81.6	0.00	0.00	31.7	566	9934	0.00
	med	n.a.	0.96	3.66	209	n.a.	206	n.a.	0.19	215	781	n.a.	n.a.	0.48	2389	0.06	5.27	10.7	n.a.	n.a.	8.38	118	2862	n.a.
	mean	n.a.	1.08	7.77	305	n.a.	2.06	n.a.	0.19	247	1431	n.a.	n.a.	0.48	2421	0.06	6.08	21.1	n.a.	n.a.	10.3	219	4132	n.a.
	S.D.	n.a.	0.26	8.01	256	n.a.	n.a.	n.a.	0.05	199	1376	n.a.	n.a.	0.05	633	0.01	3.43	22.9	n.a.	n.a.	5.84	204	2809	n.a.
	%> LOD	0.00	20.0	85.0	95.0	0.00	5.00	0.00	100	100	100	0.00	0.00	45.0	100	10.0	100	100	0.00	0.00	100	100	100	0.00
R-59	min	0.03	0.00	0.55	62.4	0.00	0.00	2.02	0.11	12.8	32.3	6.72	0.00	0.34	913	0.04	4.48	1.74	0.00	0.00	5.76	6.65	285	0.00
(N=54)	max	0.12	0.00	25.7	1548	0.00	0.00	78.2	0.81	459	4789	14.1	0.00	3.34	6631	0.05	7.31	705	0.00	0.00	108	773	7206	0.00
	med	0.08	n.a.	2.66	215	n.a.	n.a.	12.3	0.24	144	758	12.0	n.a.	0.51	2070	0.05	6.15	89.7	n.a.	n.a.	9.30	109	1973	n.a.
	mean	0.07	n.a.	4.83	334	n.a.	n.a.	19.5	0.30	176	1028	10.7	n.a.	0.76	2631	0.04	6.13	144	n.a.	n.a.	19.9	158	2399	n.a.
	S.D.	0.03	n.a.	4.95	310	n.a.	n.a.	17.8	0.18	150	1060	3.57	n.a.	0.55	1743	0.01	0.60	163	n.a.	n.a.	22.9	164	1680	n.a.
	% > LOD	9.26	0.00	100	100	0.00	0.00	46.3	22.2	100	100	9.26	0.00	74.1	100	5.56	100	96.3	0.00	0.00	90.7	100	100	0.00
R-63A	min	0.04	0.99	0.58	44.4	0.14	0.63	0.90	0.19	31.2	55.7	4.75	0.26	0.37	423	0.00	0.88	0.11	0.00	0.00	10.9	15.2	270	0.00
(N=29)	max	0.07	0.99	19.9	5701	0.14	0.94	0.90	1.90	1032	7329	5.74	0.26	0.55	4956	0.00	0.88	19.7	0.00	0.00	24.1	1332	14744	0.00
	med	0.06	0.99	8.38	902	0.14	0.76	0.90	0.56	459	2722	5.22	0.26	0.45	1289	n.a.	0.88	3.18	n.a.	n.a.	17.4	484	5244	n.a.
	mean	0.06	0.99	8.38	902	0.14	0.76	0.90	0.56	459	2722	5.22	0.26	0.45	1289	n.a.	0.88	3.18	n.a.	n.a.	17.4	484	5244	n.a.
	S.D.	0.02	n.a.	5.71	1451	n.a.	0.13	n.a.	0.42	305	2071	0.54	n.a.	0.05	1398	n.a.	n.a.	4.01	n.a.	n.a.	3.45	395	3442	n.a.
	% > LOD	6.90	3.45	100	100	3.45	13.8	3.45	51.7	100	100	13.8	3.45	86.2	100	0.00	3.45	100	0.00	0.00	100	100	100	93.1
R-67	min	0.03	0.00	0.78	41.7	0.00	0.83	0.00	0.00	24.7	4.49	9.36	0.00	0.32	458	0.00	5.75	0.07	0.00	0.00	6.08	1.75	62.4	0.00
(N=48)	max	0.03	0.00	21.9	1382	0.00	0.83	0.00	0.00	662	5537	15.3	0.00	0.54	2217	0.00	9.53	13.0	0.00	0.00	29.7	880	25084	0.00
	med	0.03	n.a.	3.12	343	n.a.	0.83	n.a.	n.a.	148	575	15.1	n.a.	0.43	1007	n.a.	8.09	0.37	n.a.	n.a.	13.8	95.9	1573	n.a.
	mean	0.03	n.a.	4.77	431	n.a.	0.83	n.a.	n.a.	218	1278	13.2	n.a.	0.43	1130	n.a.	7.97	1.54	n.a.	n.a.	14.0	224	2730	n.a.
	S.D.	n.a.	n.a.	4.27	327	n.a.	n.a.	n.a.	n.a.	174	1443	3.35	n.a.	0.04	490	n.a.	0.71	3.06	n.a.	n.a.	4.68	247	3896	n.a.
	% > LOD	2.08	0.00	100	97.9	0.00	2.08	0.00	0.00	100	100	6.25	0.00	97.9	100	0.00	100	85.4	0.00	0.00	95.8	100	100	0.00
RoeA	min	0.00	0.00	0.79	44.9	0.00	0.00	0.00	0.00	17.6	40.7	0.00	0.00	0.32	491	0.00	2.30	1.68	0.00	0.00	14.1	7.89	421	0.00
(N=23)	max	0.00	0.00	25.5	3986	0.00	0.00	0.00	0.00	681	5642	0.00	0.00	0.59	3989	0.00	3.70	50.7	0.00	0.00	49.4	844	10418	0.00
	med	n.a.	n.a.	6.16	267	n.a.	n.a.	n.a.	n.a.	350	870	n.a.	n.a.	0.44	1433	n.a.	2.75	5.90	n.a.	n.a.	20.3	202	3060	n.a.
	mean	n.a	n.a.	7.91	893	n.a.	n.a.	n.a.	n.a.	338	1900	n.a.	n.a.	0.45	1898	n.a.	2.91	10.4	n.a.	n.a.	22.9	284	3599	n.a.
	S.D.	n.a.	n.a.	7.86	1214	n.a.	n.a.	n.a.	n.a.	205	1906	n.a.	n.a.	0.07	1168	n.a.	0.46	11.2	n.a.	n.a.	9.92	258	2683	n.a.
	% > LOD	0.00	0.00	100	91.3	0.00	0.00	0.00	0.00	100	100	0.00	0.00	69.6	100	0.00	73.9	100	0.00	0.00	95.7	100	95.7	0.00

Table 6.5.: Minimum and maximum values of the elements, as well as median, mean, standard deviations found in the samples; additionally the percentage of values above detection limit (%> LOD); n.a.=not applicable due to missing data

6.3.1. Texture

The trace element compositions of the textural varieties of sphalerite are summarized in table 6.6. Significantly high median contents of iron, copper, germanium, arsenic, cadmium, tin, antimony, thallium and lead were marked orange, significantly low median contents of these elements were marked blue. Fern ore was not considered in this color scheme due to its small sample set (N=7).

The similarities and differences in trace element composition of the textural varieties of sphalerite can be recognized in the boxplots (figure 6.21) and the probability plots (Appendix B). Colloform sphalerite shows the highest iron content (6973 $\mu g/g$), followed by tubular sphalerite (3986$\mu g/g$), followed by agglomerated sphalerite (A: 1854 $\mu g/g$; B: 1589 $\mu g/g$) and fern sphalerite (591 $\mu g/g$). Layered sphalerite shows the lowest iron contents, with a maximum iron content of only 104$\mu g/g$. Comparing the different median values, agglomerated type A sphalerite exhibits the highest median iron (842 $\mu g/g$), followed by fern sphalerite (510$\mu g/g$). Colloform, tubular and agglomerated type B sphalerite show similar median iron contents (colloform: 258 $\mu g/g$; tubular: 287$\mu g/g$; agglomerated type B: 259 $\mu g/g$). Layered sphalerite shows the lowest median iron content (54.4 $\mu g/g$).

Colloform sphalerite shows the highest germanium content (1524 $\mu g/g$), followed by fern sphalerite (1072 $\mu g/g$). Agglomerated type B and tubular sphalerite shows similar germanium contents, with the tubular sphalerite exhibiting slightly higher values (agglomerated type B: maximum germanium content of 546$\mu g/g$; tubular: maximum germanium content of 681 $\mu g/g$). Layered sphalerite and agglomerated type A sphalerite show the lower maximum germanium contentsw (layered: 78.5 $\mu g/g$; agglomerated type A: 121$\mu g/g$). Comparing the median germanium contents, fern sphalerite shows the highest median germanium content(1046$\mu g/g$). Observing the colloform, and tubular sphalerite, relatively similar median germanium content can be seen (colloform: 168$\mu g/g$; 198$\mu g/g$). Agglomerated type B sphalerite shows a slightly higher median germanium content (244$\mu g/g$). Layered and agglomerated type A sphalerite show low median germanium contents (layered: 21.3$\mu g/g$; agglomerated type A: 83.7$\mu g/g$).

The highest amounts of arsenic were found within colloform sphalerite (10618 $\mu g/g$), followed by fern sphalerite (8491 $\mu g/g$). Tubular sphalerite shows the biggest variation in arsenic content, ranging from 4.49 to 5642 $\mu g/g$. The highest arsenic content found in agglomerated type B sphalerite is 3594 $\mu g/g$. The maximum arsenic content found in agglomerated type A sphalerite is 546$\mu g/g$. The lowest maximum arsenic content can be observed in layered sphalerite (67.6$\mu g/g$). Considering median arsenic contents, fern ore shows the highest (7613$\mu g/g$). Colloform, agglomerated type B and tubular sphalerite show more similar median arsenic content compared to fern sphalerite, layered sphalerite and agglomerated type A sphalerite (colloform: 888 $\mu g/g$; agglomerated type B: 1475 $\mu g/g$; tubular: 669$\mu g/g$). Layered sphalerite and agglomerated type A show the lower median arsenic content (layered: 67.6 $\mu g/g$; 313$\mu g/g$).

Colloform sphalerite contains the highest amount of cadmium (7640$\mu g/g$), followed by layered sphalerite (7062 $\mu g/g$). Agglomerated type A sphalerite (4247$\mu g/g$), agglomerated type B sphalerite (6656$\mu g/g$),fern sphalerite (1009 $\mu g/g$) and tubular sphalerite (3989$\mu g/g$) exhibit lower maximum cadmium contents. The highest median cadmium content can be observed in layered sphalerite (4927$\mu g/g$), followed by agglomerated type

A sphalerite ($2829\mu g/g$). Colloform sphalerite and tubular sphalerite show more similar median cadmium contents compared to the other textures (colloform: $1638\mu g/g$; tubular: $1163\mu g/g$). Fern sphalerite and agglomerated type B sphalerite exhibit the lower median cadmium content (fern: $875\mu g/g$; $699\mu g/g$).

Fern sphalerite exhibits a high maximum thallium content ($1727~\mu g/g$), as well as a high median thallium content ($1519\mu g/g$). Layered sphalerite shows the lowest thallium contents (at maximum $19.0\mu g/g$), as well as the lowest median thallium contents ($10.4\mu g/g$). Colloform and tubular sphalerite show the highest variation in thallium contents, colloform ranging from 3.72 to $2324\mu g/g$ and tubular ranging from 1.75-$880\mu g/g$. Agglomerated type A sphalerite shows a maximum thallium content of$122\mu g/g$, while agglomerated sphalerite type B shows a maximum thallium content of $696~\mu g/g$. Colloform and tubular sphalerite exhibit similar median thallium contents (colloform: $144\mu g/g$; tubular: $116\mu g/g$). The median thallium content of agglomerated sphalerite type B is slightly higher ($274\mu g/g$). The median thallium content of agglomerated sphalerite type A is low ($61.9\mu g/g$).

The highest lead content was found in colloform sphalerite ($39955\mu g/g$). This is an exceptionally high lead content, but the signal obtained from LA-ICP-MS is smooth and does not show an indication for inclusions (figure 6.20).
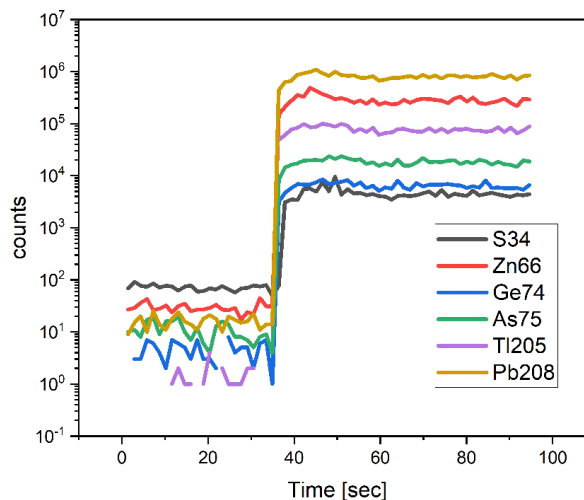
Figure 6.20.: Signal producing an exceptionally high lead content ($39955\mu g/g$), showing no sign of micro-inclusions

Tubular sphalerite and fern sphalerite also show high lead contents (tubular: $25084\mu g/g$; fern sphalerite: $14393\mu g/g$). Agglomerated type B sphalerite shows a maximum lead content of $6515\mu g/g$. Agglomerated type A sphalerite shows a lower maximum lead content ($2934\mu g/g$). Layered sphalerite has the lowest maximum lead content ($1004\mu g/g$). Considering the median lead content, fern sphalerite has the highest ($12600\mu g/g$). Colloform, agglomerated type A and B and tubular sphalerite show similar median values when compared to the other two sphalerite textural varieties (colloform: $2606\mu g/g$; agglomerated type A: $1462\mu g/g$; agglomerated type B: $3315~\mu g/g$; tubular: $1837\mu g/g$). Layered ore exhibits the lowest median lead content ($595~\mu g/g$).

All textures of sphalerite show relatively constant, low contents of vanadium, chromium, cobalt, nickel, manganese, silver. Colloform sphalerite exhibits significant contents of copper (maximum $321\mu g/g$), and gallium (maximum 89.9 $\mu g/g$), while the other textural types contain only insignificant amounts of these elements. Layered sphalerite does not exhibit selenium contents above the detection limit, the other textures show low, insignificant contents of selenium. Molybdenum was only found in colloform and agglomerated type A sphalerite, the other textures were molybdenum-free. Layered sphalerite does not show tin contents above the detection limit, whereas colloform sphalerite contains the most tin ($20.2\mu g/g$). Colloform sphalerite shows the greatest variation in antimony content, ranging from $0.06\text{-}1536\mu g/g$, followed by layered sphalerite ranging from 28.3-$230\mu g/g$ and agglomerated type B sphalerite ranging from $1.69\text{-}108\mu g/g$. Fern sphalerite, agglomerated type A and tubular sphalerite show lower antimony contents (fern sphalerite: maximum $12.1\mu g/g$; tubular sphalerite: maximum $50.7\mu g/g$; agglomerated type A sphalerite: 83.9 $\mu g/g$). Colloform sphalerite contains the most mercury (108 $\mu g/g$), while the other textures contain significantly less (below $50\mu g/g$). Indium, tellurium, gold and bismuth could not be found or were found in extremely low contents in all sphalerite textures.

texture		V	Cr	Mn	Fe	Co	Ni	Cu	Ga	Ge	As	Se	Mo	Ag	Cd	In	Sn	Sb	Te	Au	Hg	Tl	Pb	Bi
colloform	min	0.03	0.41	0.53	33.4	0.02	0.23	0.52	0.04	8.89	13.9	3.61	0.08	0.29	277	0.04	0.75	0.06	0.00	0.00	5.23	3.72	163	0.01
(N=318)	max	0.28	1.47	131	6973	16.4	2.06	321	89.9	1524	10618	14.1	0.26	6.96	7640	0.06	20.2	1536	0.00	0.00	108	2324	39955	0.05
(R-10, R-16, R-17A,	med	0.07	0.90	5.86	258	0.06	0.82	8.37	0.70	168	888	6.62	0.14	0.46	1638	0.05	5.37	14.4	n.a.	n.a.	12.0	144	2606	0.01
R-24, R-28, R-29,	mean	0.08	0.89	8.29	484	0.63	0.93	41.3	3.71	244	1476	7.17	0.17	0.73	2066	0.05	4.89	111	n.a.	n.a.	14.3	261	3561	0.02
R-32, R-40, R-45,	S.D.	0.05	0.27	12.6	759	2.98	0.45	78.1	11.5	268	1920	2.68	0.06	0.97	1388	0.01	2.31	207	n.a.	n.a.	11.0	368	4029	0.01
R-49, R-59, R-63A)	%> LOD	8.81	8.18	95.6	96.5	9.43	5.97	30.8	36.8	100	100	8.49	2.20	78.9	100	2.20	63.8	9.2	0.00	0.00	97.8	100	97.2	3.14
layered	min	0.05	0.00	0.60	45.8	0.00	0.00	1.03	0.16	6.32	9.68	0.00	0.00	0.42	3967	0.00	0.00	28.3	0.00	0.00	11.2	2.13	180	0.00
(N=14)	max	0.28	0.00	1.54	104	0.00	0.00	4.32	1.52	78.5	67.6	0.00	0.00	0.69	7062	0.00	0.00	230	0.00	0.00	33.7	19.0	1004	0.00
(R-21)	med	0.09	n.a.	1.06	54.4	n.a.	n.a.	1.91	0.49	21.3	25.8	n.a.	n.a.	0.51	4927	n.a.	n.a.	59.5	n.a.	n.a.	13.2	10.4	595	n.a.
	mean	0.12	n.a.	1.02	62.8	n.a.	n.a.	2.17	0.61	30.5	27.7	n.a.	n.a.	0.52	5222	n.a.	n.a.	104	n.a.	n.a.	16.3	10.5	584	n.a.
	S.D.	0.07	n.a.	0.27	19.0	n.a.	n.a.	1.05	0.39	25.6	16.2	n.a.	n.a.	0.08	950	n.a.	n.a.	79.1	n.a.	n.a.	6.80	4.71	300	n.a.
	% > LOD	57.1	0.00	85.7	78.6	0.00	0.00	71.4	78.6	100	100	0.00	0.00	100	100	0.00	0.00	71.4	0.00	0.00	92.9	85.7	100	0.00
agglomerated (type A)	min	3.12	0.89	3.89	337	0.06	0.77	0.94	0.23	50.0	161	3.82	0.35	0.40	2207	0.00	1.18	30.7	0.00	0.00	17.7	27.7	702	0.01
(N=14)	max	3.12	4.07	8.59	1854	0.31	4.83	8.40	1.36	121	546	7.72	3.33	0.56	4247	0.00	1.70	83.9	0.00	0.00	29.7	122	2934	0.02
(R-27)	med	3.12	1.42	6.12	842	0.16	2.90	2.87	0.37	83.7	313	5.78	1.20	0.47	2829	n.a.	1.61	46.5	n.a.	n.a.	24.0	61.9	1462	0.01
	mean	3.12	1.76	5.99	937	0.17	2.71	3.45	0.44	84.4	366	5.75	1.52	0.47	2986	n.a.	1.54	50.1	n.a.	n.a.	24.0	66.3	1543	0.01
	S.D.	n.a.	1.08	1.64	429	0.07	1.26	1.89	0.29	22.5	124	1.27	1.28	0.05	567	n.a.	0.18	15.6	n.a.	n.a.	3.96	25.4	643	0.00
	% > LOD	7.14	57.1	100	92.9	92.9	85.7	92.9	92.9	100	92.9	42.9	28.6	92.9	100	0.00	64.3	100	0.00	0.00	100	100	85.7	28.6
agglomerated (type B)	min	0.06	0.00	1.54	129	0.00	0.00	0.00	0.00	21.3	58.3	0.00	0.00	0.33	430	0.00	1.92	1.69	0	0	5.62	12.3	1036	0.00
(N=27)	max	0.22	0.00	18.2	1589	0.00	0.00	0.00	0.00	546	3594	0.00	0.00	0.61	6656	0.00	7.81	108	0.00	0.00	20.4	696	6515	0.00
(R-32, R-45)	med	0.09	n.a.	11.7	259	n.a.	n.a.	n.a.	n.a.	244	1475	n.a.	n.a.	0.48	699	n.a.	5.50	16.4	n.a.	n.a.	15.5	274	3315	n.a.
	mean	0.11	n.a.	10.2	475	n.a.	n.a.	n.a.	n.a.	253	1561	n.a.	n.a.	0.48	1389	n.a.	5.23	24.6	n.a.	n.a.	12.7	311	3274	n.a.
	S.D.	0.07	n.a.	4.53	437	n.a.	n.a.	n.a.	n.a.	118	773	n.a.	n.a.	0.07	1429	n.a.	1.39	26.0	n.a.	n.a.	5.26	160	1202	n.a.
	% > LOD	14.8	0.00	100	100	0.00	0.00	0.00	0.00	100	100	0.00	0.00	85.2	100	0.00	100	100	0.00	0.00	100	100	100	0.00
fern	min	0.02	0.48	22.0	377	0.07	0.00	0.55	0.13	1014	7003	5.99	0.00	0.35	796	0.03	5.73	5.47	0.19	0.00	10.9	1340	10800	0.00
(N=7)	max	0.07	0.57	25.6	591	0.07	0.00	0.55	1.85	1072	8491	15.3	0.00	0.46	1009	0.06	17.2	12.1	0.19	0.00	13.5	1727	14393	0.00
(R-36)	med	0.03	0.54	23.5	510	0.07	n.a.	0.55	0.26	1046	7613	10.6	n.a.	0.42	875	0.05	6.29	8.58	0.19	n.a.	12.5	1519	12600	n.a.
	mean	0.04	0.53	24.0	502	0.07	n.a.	0.55	0.54	1042	7696	10.6	n.a.	0.41	908	0.05	9.55	8.51	0.19	n.a.	12.5	1520	12742	n.a.
	S.D.	0.02	0.05	1.54	72.1	n.a.	n.a.	n.a.	0.61	22.3	544	6.56	n.a.	0.04	79.3	0.01	4.73	2.49	n.a.	n.a.	0.79	115	1212	n.a.
	%> LOD	85.7	42.9	100	100	14.3	0.00	14.3	100	100	100	28.6	0.00	100	100	57.1	100	100	14.3	0.00	100	100	100	0.00
tubular	min	0.03	0.0	0.78	41.7	0.00	0.83	0.00	0.00	17.6	4.49	9.36	0.00	0.32	458	0.00	2.30	0.07	0.00	0.00	6.08	1.75	62.4	0.00
(N=71)	max	0.03	0.00	25.5	3986	0.00	0.83	0.00	0.00	681	5642	15.3	0.00	0.59	3989	0.00	9.53	50.7	0.00	0.00	49.4	880	25084	0.00
(R-67, RoeA)	med	0.03	n.a.	3.52	287	n.a.	0.83	n.a.	n.a.	198	669	15.05	n.a.	0.43	1163	n.a.	7.66	1.16	n.a.	n.a.	15.7	116	1837	n.a.
	mean	0.03	n.a.	5.79	573	n.a.	0.83	n.a.	n.a.	257	1480	13.2	n.a.	0.43	1379	n.a.	6.65	4.72	n.a.	n.a.	16.9	243	3003	n.a.
	S.D.	n.a.	n.a.	5.82	748	n.a.	n.a.	n.a.	n.a.	192	1621	3.35	n.a.	0.05	849	n.a.	2.33	8.26	n.a.	n.a.	7.95	251	3563	n.a.
	% > LOD	1.41	0.00	100	95.8	0.00	1.41	0.00	0.00	100	100	4.23	0.00	88.7	100	0.00	91.6	90.1	0.00	0.00	95.8	100.00	98.6	0.00

Table 6.6.: Trace element content of different sphalerite textures, min=minimum, max=maximum, med=median, mean=arithmetic mean, S.D. = standard deviation, %> LOD = percentage of measurements above load of detection, n.a. = not applicable due to lack of data; numbers are given in $\mu g/g$; higher medians of important elements are marked orange, lowest medians are marked blue
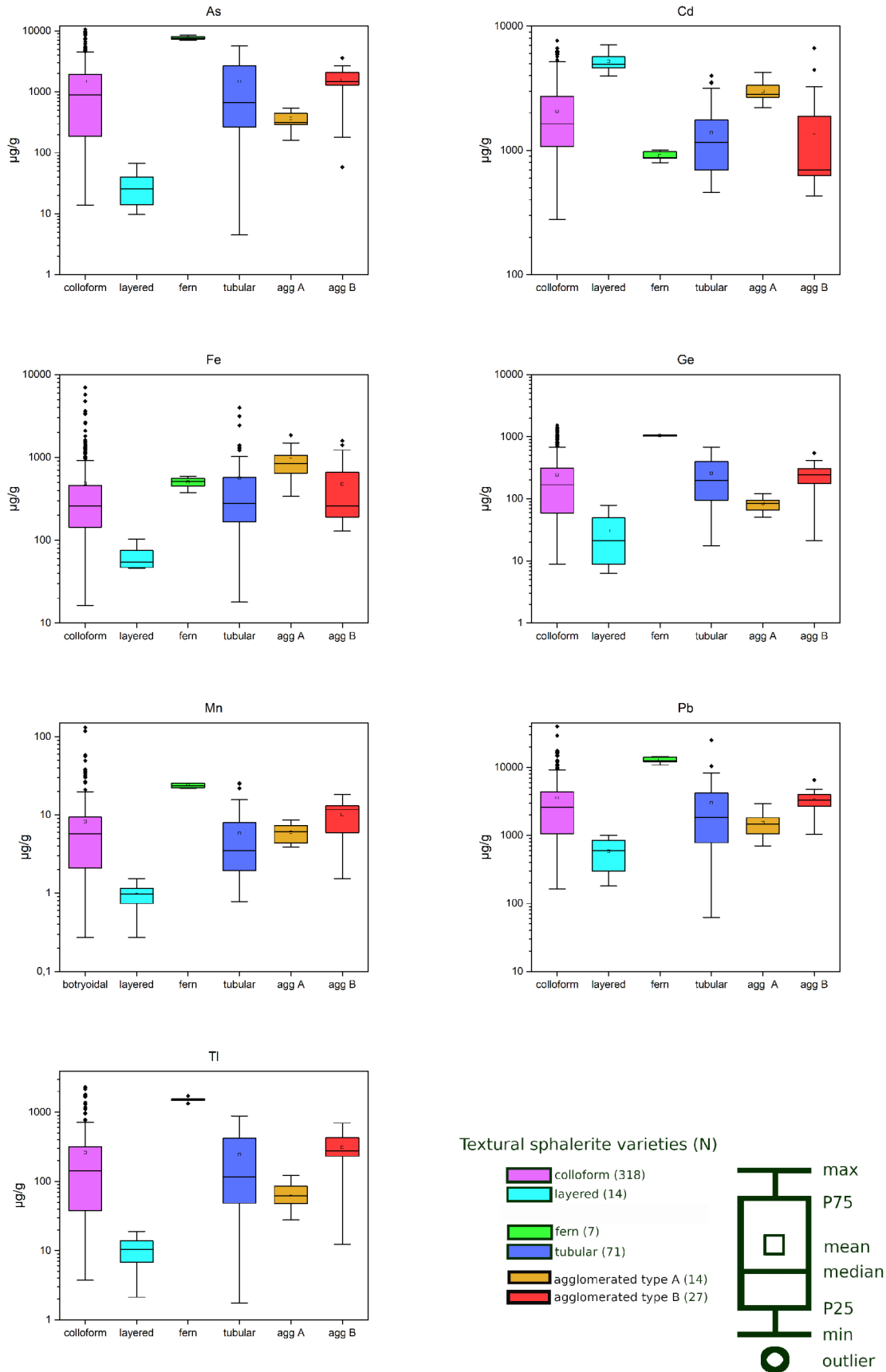
Figure 6.21.: Boxplots depicting part of the trace element composition (arsenic, cadmium, iron, germanium, manganese, lead, thallium) of sphalerite textures; agg = agglomerated

6.3.2. Colors

The trace element compositions of the color varieties of sphalerite are summarized in table 6.7. Significantly high median contents of iron, copper, germanium, arsenic, cadmium, tin, antimony, thallium and lead were marked orange, significantly low median contents of these elements were marked blue. The boxplots displaying the contents of different elements (arsenic, cadmium, iron, germanium, manganese, lead and thallium) ordered after color varieties can be seen in 6.22. The variance of trace element content can be seen in these.

Brown sphalerite shows high contents of iron (up to $6973\mu g/g$), germanium (up to 1524 $\mu g/g$), arsenic (up to $10618\mu g/g$), cadmium (up to 7062 $\mu g/g$), thallium (up to $2324\mu g/g$) and lead (up to $39955\mu g/g$). Brown sphalerite exibits the biggest variance in arsenic, cadmium, iron, germanium, lead and thallium compared to the other color varieties, which is probably caused by the large data set pertaining to the brown color variety (N=239). Looking at maximum element contents and comparing to brown sphalerite, red sphalerite contains lower amounts of iron (up to $3986\mu g/g$), germanium (up to $1032\mu g/g$), arsenic (up to $8819\mu g/g$), cadmium (up to $5182\mu g/g$), thallium (up to $1727\mu g/g$) and lead ($14744\mu g/g$). However, the median values show another story. Red sphalerite exhibits a higher median iron content (409 $\mu g/g$) compared to brown sphalerite ($285\mu g/g$). The median germanium content is similar in brown and red sphalerite (brown: 211; red: $242\mu g/g$). Brown sphalerite shows a higher median arsenic content ($1183\mu g/g$) compared to red sphalerite ($1590\mu g/g$). Red sphalerite shows a slightly higher median thallium content (brown: $214\mu g/g$; red: $293\mu g/g$) and a higher median lead content (brown: $3081\mu g/g$; red: $3412\mu g/g$).

Considering both maximum values and median values, grey sphalerite shows lower contents of iron (maximum: $1854\mu g/g$; median: $120\mu g/g$), germanium (maximum: $187\mu g/g$; median: $50.0\mu g/g$), arsenic (maximum: $663\mu g/g$; median:$149\mu g/g$), thallium (maximum: $122\mu g/g$; median: $33.5\mu g/g$) and lead (maximum: 3041; median: $758\mu g/g$). But the grey color variety of sphalerite has a significantly higher cadmium content than the other color varieties, considering the median value ($2997\mu g/g$).

Green sphalerite shows lower maximum iron content ($1287\mu g/g$) compared to brown, red and grey sphalerite, but a higher maximum iron content compared to yellow sphalerite. The green variety has the second lowest median iron content ($201\mu g/g$) with only the grey color variety exhibiting a lower median iron content. Green sphalerite can contain up to $577\mu g/g$, but considering the median germanium values, green sphalerite has the second lowest median germanium content after grey sphalerite ($113\mu g/g$). Green sphalerite shows lower arsenic contents than brown and red sphalerite, but higher arsenic contents than grey sphalerite (maximum: $4287\mu g/g$; median: $448\mu g/g$). Green sphalerite shows a greater variation in cadmium content (430-$7640\mu g/g$) than yellow sphalerite and a higher median cadmium content than the yellow color variety ($1770\mu g/g$). Green sphalerite exhibits a thallium content between 8.37 and $650\mu g/g$, with a median thallium content of $68.6\mu g/g$. Green sphalerite contains slightly more lead than yellow sphalerite (268-$6254\mu g/g$).

Yellow sphalerite shows lower iron contents than the other color varieties (maximum: $493\mu g/g$), but a higher median iron content ($264\mu g/g$) compared to grey and green spha-

lerite. Yellow sphalerite contains more germanium than the grey color variety (up to $409\mu g/g$), but this content is lower than the one found in other color varieties. The yellow color variety has a median germanium content of $128\mu g/g$. Yellow sphalerite has a lower maximum arsenic content than green sphalerite ($1996\mu g/g$), but a higher median arsenic content ($505\mu g/g$). Yellow sphalerite shows a cadmium content between 618 and $2978\mu g/g$, with a median cadmium value of $1567\mu g/g$. Yellow sphalerite exhibits a thallium content between 19.2 and $370\mu g/g$, with a median thallium content similar to green sphalerite ($81.1\mu g/g$). Yellow sphalerite contains slightly less lead than green sphalerite (234-$4542\mu g/g$), but both color varieties show similar median lead contents (green: $1826\mu g/g$; yellow: $1736\mu g/g$).

All color varieties of sphalerite show constant, low contents of vanadium, chromium and silver. Indium, tellurium, gold and bismuth are present either at a very low level or below detection level. The yellow color variety does not contain cobalt and selenium, while the other color varieties contain low levels of cobalt and selenium. The green color variety does not contain nickel, the other color varieties contain low levels of nickel. Red and green sphalerite do not contain molybdenum, while the other color varieties contain low levels of molybdenum.

Apart from some outliers in brown and red sphalerite, the color varieties show relatively constant mercury contents. If some outliers in brown sphalerite are not considered, the color varieties show relatively constant manganese and tin contents. Yellow sphalerite does not contain copper, the other color varieties show low median values, but also higher maximum values, with red and green sphalerite showing values slightly above $300\mu g/g$. While all color varieties show similar median gallium contents, brown and red sphalerite exhibit higher maximum values (brown: $89.9\mu g/g$; red: $64.7\mu g/g$), grey, green and yellow varieties show lower maximum values (grey: $7.92\mu g/g$; green: $5.84\mu g/g$; yellow: $1.10\mu g/g$). Although brown, red and green exhibit some outliers, all color varieties show similar median antimony contents.

color		V	Cr	Mn	Fe	Co	Ni	Cu	Ga	Ge	As	Se	Mo	Ag	Cd	In	Sn	Sb	Te	Au	Hg	Tl	Pb	Bi
brown	min	0.02	0.48	0.55	41.7	0.03	0.23	0.55	0.05	6.32	4.49	5.05	0.08	0.29	277	0.03	0.88	0.12	0.19	0.00	5.23	1.75	62.4	0.01
(N=239)	max	0.22	1.47	131	6973	16.4	2.06	260	89.9	1524	10618	15.3	0.21	6.96	7062	0.06	20.2	1536	0.19	0.00	108	2324	39955	0.01
(R-10, R-16, R-17A, R-21,	med	0.06	0.81	6.48	285	0.06	0.82	3.41	0.53	211	1183	7.00	0.14	0.46	1442	0.05	5.53	12.51	0.19	n.a.	12.1	214	3081	0.01
R-24, R-28, R29, R-32,	mean	0.07	0.85	9.05	561	0.85	0.96	21.8	3.98	294	1837	8.37	0.15	0.63	1988	0.05	5.17	104	0.19	n.a.	14.5	335	4357	0.01
R-36, R-40, R-45, R-49,	S.D.	0.04	0.29	12.2	850	3.56	0.50	51.4	12.2	306	2244	3.59	0.05	0.87	1518	0.01	2.68	212	n.a.	n.a.	11.9	434	4789	0.00
R-59, R-63A, R-67, RoeA)	% > LOD	14.2	9.21	96.2	97.1	8.79	6.28	25.9	32.2	100	100	6.69	2.51	79.5	100	4.60	74.1	95.8	0.42	0.00	98.3	99.6	97.9	2.51
red	min	0.03	0.41	0.78	33.4	0.02	0.83	0.52	0.04	23.9	33.6	3.61	0.00	0.35	423	0.00	0.75	0.08	0.00	0.00	5.76	13.0	163	0.01
(N=81)	max	0.10	0.41	31.9	3986	0.19	0.94	315	64.7	1032	8819	13.7	0.00	6.03	5182	0.00	9.20	470	0.00	0.00	49.4	1727	14744	0.01
(R-10, R-16, R-17A, R-24,	med	0.08	0.41	7.04	409	0.08	0.87	23.7	0.79	242	1590	6.48	n.a.	0.43	1111	n.a.	6.16	8.67	n.a.	n.a.	15.2	293	3412	0.01
R-28, R-29, R-32, R-45,	mean	0.07	0.41	8.16	645	0.10	0.88	74.0	4.43	318	2040	7.45	n.a.	0.76	1273	n.a.	5.48	66.57	n.a.	n.a.	16.3	356	3540	0.01
R-59, R-63A, R-67, RoeA)	S.D.	0.04	n.a.	6.27	713	0.06	0.05	104	14.6	233	1802	2.93	n.a.	1.00	829	n.a.	2.44	113	n.a.	n.a.	8.99	324	2686	n.a.
	% > LOD	3.70	1.23	98.8	96.3	9.88	3.70	22.2	23.5	100	100	13.6	0.00	91.4	100	0.00	70.4	95.1	0.00	0.00	95.1	100	98.8	1.23
grey	min	0.04	0.89	0.60	44.4	0.06	0.77	0.90	0.20	6.79	9.68	3.82	0.35	0.34	1714	0.00	1.18	0.39	0.00	0.00	6.76	2.13	180	0.01
(N=53)	max	3.12	4.07	8.59	1854	0.31	4.83	80.6	7.92	187	663	7.72	3.33	1.39	5247	0.00	7.44	101	0.00	0.00	33.7	122	3041	0.02
(R-10, R-17A, R-21,	med	0.17	1.21	1.98	120	0.16	2.90	2.87	0.42	50.0	149	5.71	1.20	0.47	2997	n.a.	4.24	27.49	n.a.	n.a.	18.1	33.5	758	0.01
R-27, R-29, R-32,	mean	0.74	1.69	2.88	341	0.17	2.71	10.9	1.13	61.6	208	5.64	1.52	0.53	3213	n.a.	4.14	29.3	n.a.	n.a.	17.1	39.2	1091	0.01
R-59, R-63A, RoeA)	S.D.	1.33	1.04	2.26	432	0.07	1.26	19.3	1.90	46.0	180	1.13	1.28	0.20	939	n.a.	2.23	28.0	n.a.	n.a.	7.48	29.3	788	0.00
	% > LOD	9.43	17.0	92.4	90.1	24.5	22.6	50.9	49.1	100	98.1	15.1	7.55	77.4	100	0.00	49.1	94.34	0.00	0.00	98.1	98.1	96.2	7.55
green	min	0.04	0.73	0.53	58.5	0.15	0.00	1.9	0.19	9.89	22.6	4.02	0.00	0.32	430	0.00	0.82	0.06	0.00	0.00	6.08	8.37	268	0.02
(N=65)	max	0.28	1.09	21.1	1287	0.19	0.00	321	5.84	577	4287	15.1	0.00	4.19	7640	0.00	9.53	871	0.00	0.00	38.5	650	6254	0.05
(R-10, R-16, R-17A, R-24,	med	0.07	0.77	2.71	201	0.17	n.a.	12.2	0.71	113	448	8.99	n.a.	0.46	1770	n.a.	6.93	5.57	n.a.	n.a.	12.8	68.6	1826	0.04
R-28, R-29, R-40, R-45,	mean	0.12	0.86	5.33	258	0.17	n.a.	75.6	1.56	145	727	9.35	n.a.	0.63	2213	n.a.	6.32	100	n.a.	n.a.	13.1	116	2069	0.04
R-49, R-63A, R-67)	S.D	0.11	0.20	5.24	226	0.03	n.a.	116	1.92	117	800	5.52	n.a.	0.66	1524	n.a.	2.12	202	n.a.	n.a.	5.42	127	1462	0.01
	% > LOD	18.5	6.15	100	100	10.8	7.69	29.2	27.7	100	100	4.62	13.9	87.7	100	3.08	67.7	96.9	0.00	0.00	98.5	100	100	6.15
yellow	min	0.07	0.93	1.96	87.7	0.00	0.70	0.00	0.14	25.5	66.4	0.00	0.26	0.36	618	0.00	2.24	0.14	0.00	0.00	6.85	19.2	234	0.00
(N=16)	max	0.17	0.98	30.7	493	0.00	0.77	0.00	1.10	409	1996	0.00	0.26	0.54	2978	0.00	8.43	44.2	0.00	0.00	23.8	370	4542	0.00
(R-28, R-40, R-49, R-63A)	med	0.12	0.96	7.48	264	n.a.	0.73	n.a.	0.33	128	505	n.a.	0.26	0.47	1567	n.a.	5.28	8.98	n.a.	n.a.	13.8	81.1	1736	n.a.
	mean	0.12	0.96	9.30	259	n.a.	0.73	n.a.	0.40	180	854	n.a.	0.26	0.46	1726	n.a.	5.18	16.6	n.a.	n.a.	13.9	146	1927	n.a.
	S.D	0.07	0.03	8.09	128	n.a.	0.05	n.a.	0.29	114	747	n.a.	n.a.	0.05	970	n.a.	1.87	15.6	n.a.	n.a.	5.48	131	1528	n.a.
	% > LOD	12.5	12.5	100	100	0.00	12.5	0.00	56.3	100	100	0.00	6.25	68.8	100	0.00	62.5	87.5	0.00	0.00	100	100	87.5	0.00

Table 6.7.: Trace element content of differently colored sphalerite, min=minimum, max=maximum, med=median, mean=arithmetic mean, S.D. = standard deviation, %> LOD = percentage of measurements above load of detection, n.a.=not applicable; numbers are given in $\mu g/g$; higher medians of important elements are marked orange, lowest medians are marked blue
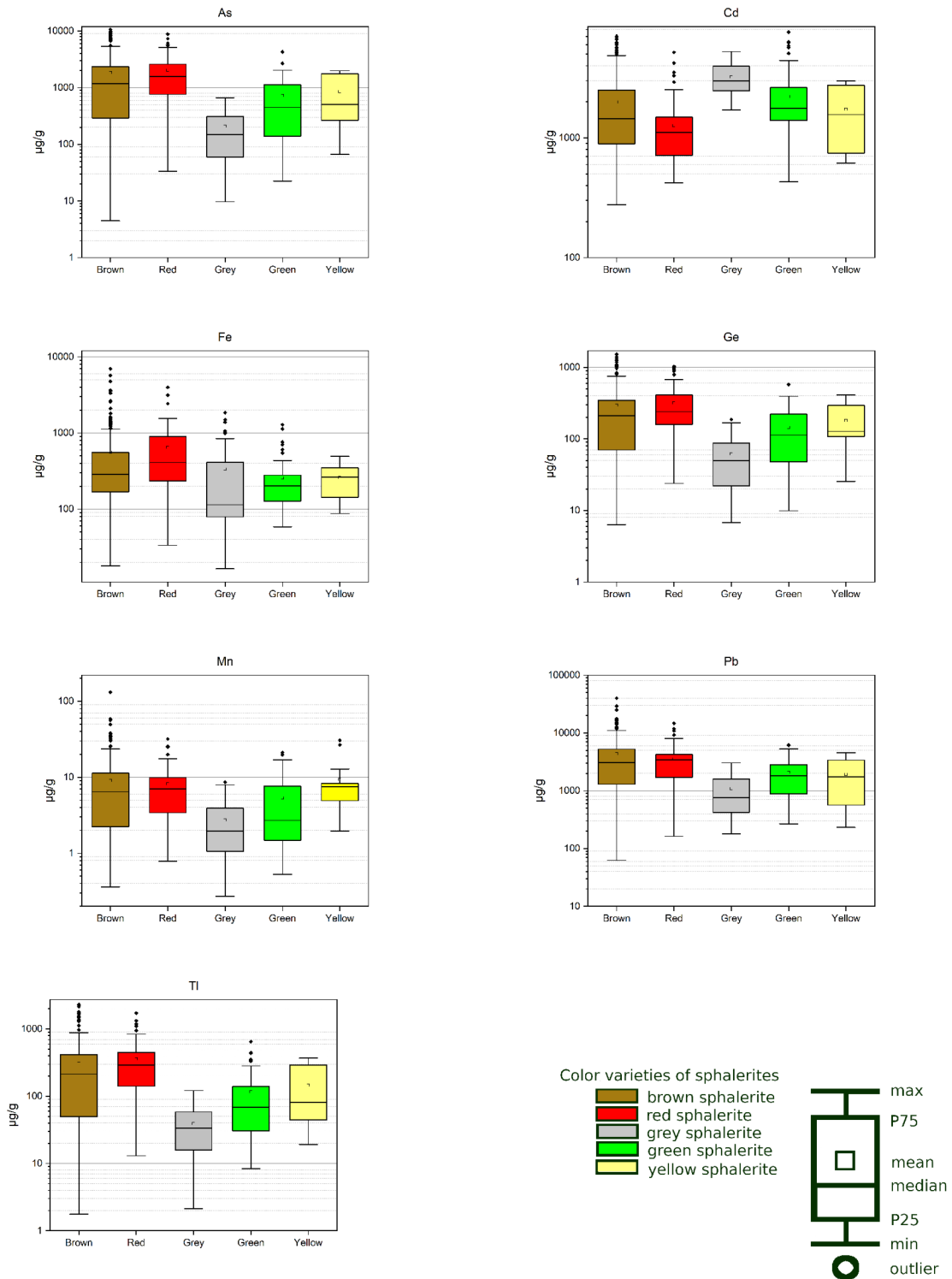
Figure 6.22.: Box-plots showing contents of arsenic, cadmium, iron, germanium, manganese, lead and thallium, sorted after color

6.3.3. Summary of the trace element composition of sphalerites

The median iron, germanium, arsenic, cadmium, thallium and lead contents of the textural and color varieties of sphalerite are summarized in table 6.8. To facilitate reading of the table, high values were colored orange, low values were colored blue and intermediate

values can be seen in yellow. Median values pertaining fern sphalerite were ignored for the color scheme, due to the problematic small data set (N=7), as this would distort the color scale.

	Fe	Ge	As	Cd	Tl	Pb
colloform	258	168	888	1638	144	2606
layered	54.4	21.3	25.8	4927	10.4	595
agglomerated type A	842	83.7	313	2829	61.9	1462
agglomerated type B	259	244	1475	699	274	3315
fern	510	1046	7613	875	1519	12600
tubular	287	198	669	1163	116	1837
brown	285	211	1183	1442	214	3081
red	409	242	1590	1111	293	3412
grey	120	50.0	149	2997	33.5	758
green	201	113	448	1770	68.6	1826
yellow	264	128	505	1567	81.1	1736

Table 6.8.: Median values of iron, germanium, arsenic, cadmium, thallium and lead of textural and color varieties; all values are given in $\mu g/g$; orange-high values, blue-low values, yellow-intermediate values

6.3.4. Element Distribution Maps

Two sets of element distribution maps, from one section of a tubular sample (RoeA) and from one section of a colloform sample (63A), were produced using LA-ICP-MS (figure 6.23 and 6.24). Both sets of element distribution maps show the compositional heterogenity of sphalerite. The banded texture of sphalerite is more intricately zoned, than can be seen under the microscope or with the naked eye. Figure 6.23 shows the element map of the tubular sample. The sulfur and the zinc map show the extent of the sphalerite, not considering any textural differences within the sphalerite. The element distribution maps of magnesium and calcium show the outline of the gangue mineral (dolomite). The maps of germanium, arsenic, thallium and lead exhibit similar patterns of bands, indicating a possible positive correlation. Manganese and iron also show similar patterns as the elements before, but not as distinctive. Antimony shows a slightly different pattern. Mercury content seems to be constant apart from the borders of the bands visible under the microscope and around cracks. Cadmium shows the opposite pattern of germanium, arsenic and thallium, indicating negative correlation.
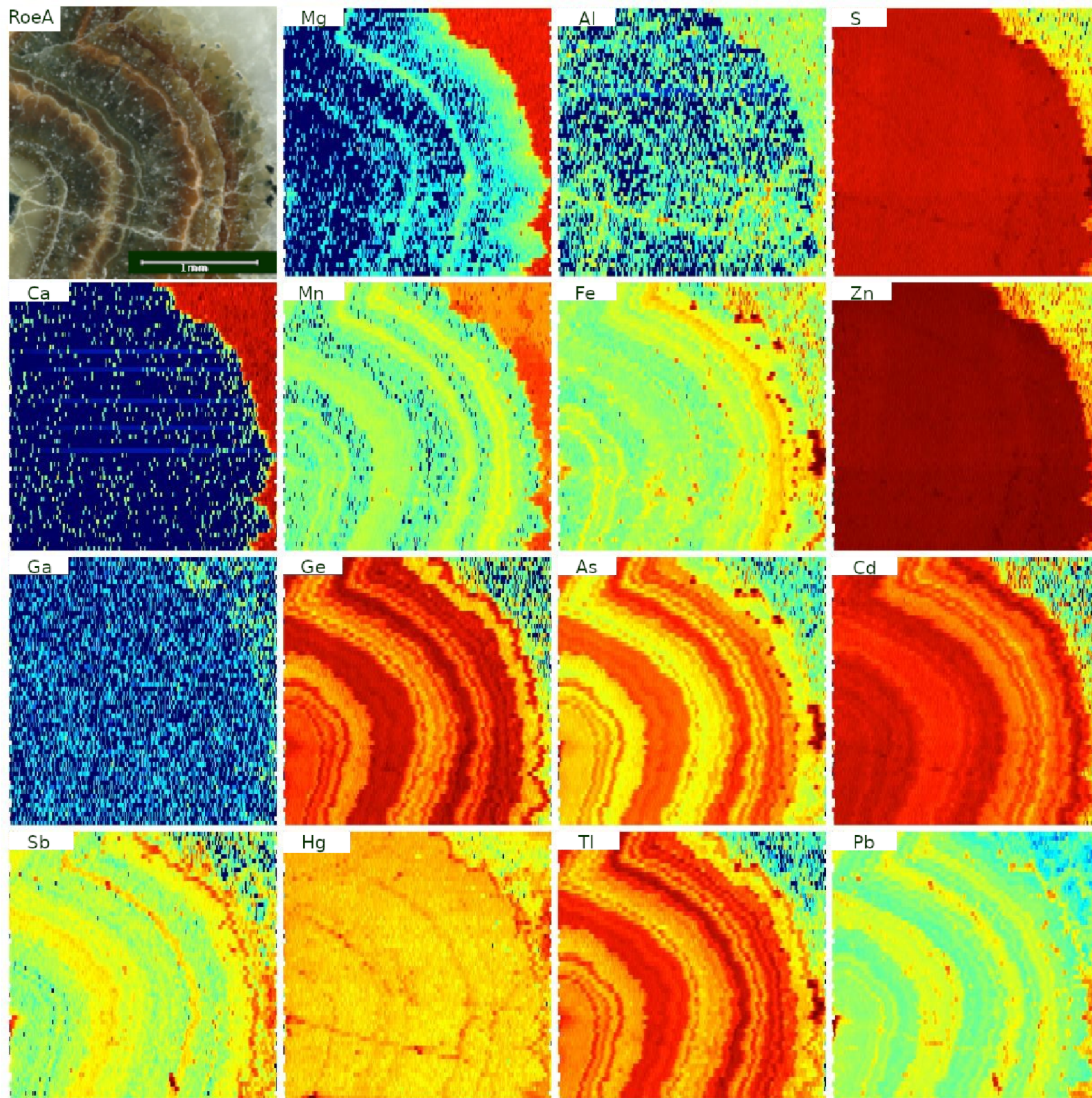
Figure 6.23.: LA-ICP-MS element distribution maps of a section of the sample RoeA (tubular ore)

Figure 6.24 shows the element distribution maps of a colloform sphalerite with pyrite as an outer rim. The extent of pyrite can be seen well in the maps illustrating the variations of sulfur and iron, but is also clearly visible as a dark rim in the arsenic map and the lead map, indicating a possible correlation of these two elements within pyrite. A significant thallium, cobalt and nickel content of pyrite is indicated by the respective element maps. Concerning the sphalerite, the same pattern of germanium, arsenic, thallium and lead can be seen in the maps, which may be a sign of positive correlation. Cadmium shows the opposite pattern compared to germanium, arsenic, thallium and lead, which may indicate a negative correlation to the aforementioned elements. Additionally, lead seems to be present in galena mobilisates, crossing the banding structure of the sphalerite. A similar pattern as these mobilisates is depicted in the element distribution map of antimony. The element distribution maps of vanadium, chromium, cobalt, nickel, copper, gallium, selenium, silver, indium, tin, tellurium, gold, mercury and bismuth do not give significant information regarding sphalerite.
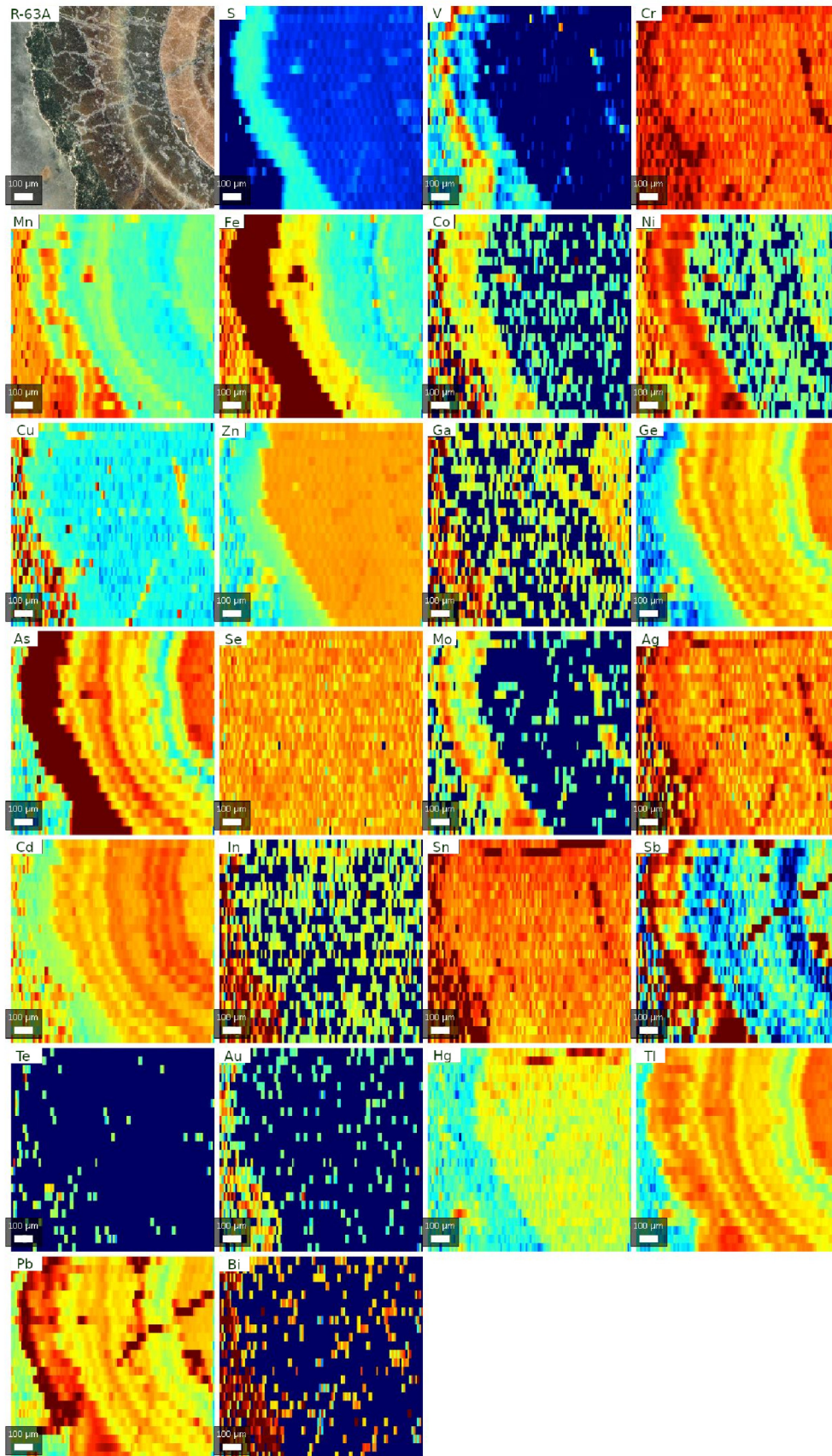
Figure 6.24.: LA-ICP-MS element distribution maps of a section of the sample 63A (collo-form sphalerite)

6.3.5. Geostatistical data evaluation

To determine, which elements correlate with each other in sphalerite in general, a correlation matrix was calculated. The complete data set was utilized according to the rules stated in section 5.6. The graphical result can be seen in figure 6.25. Blue colors show a positive correlation, red colors a negative correlation. The absolute value of the correlation coefficients is displayed graphically as the size of the squares. The numerical values of the calculated correlation matrix can be seen in the appendix under C.

Thallium, arsenic, germanium, lead, manganese and iron exhibit a significant positive correlation. Cadmium is negatively correlated to arsenic, thallium, germanium, lead and manganese. The other elements depicted in figure 6.25 show minor, not as significant, correlations.
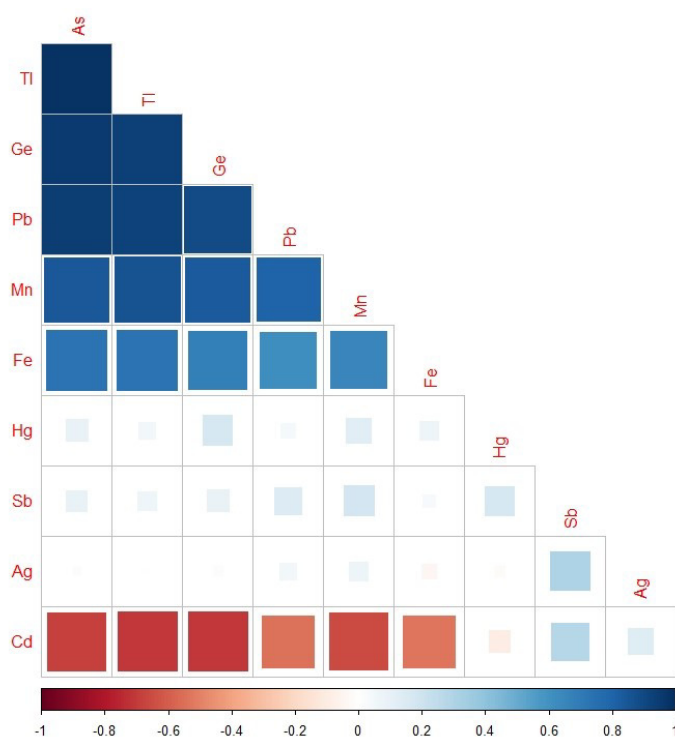
Figure 6.25.: Correlation plot of trace elements found in sphalerite in general

A principal factor analysis was used to study the interrelationships of elements within colloform sphalerite. The first factor (F1), which accounts for 52% of the the total variance, associates the elements showing a high correlation (manganese, iron, germanium, arsenic, thallium, lead and negative cadmium). Cadmium, tin and antimony are linked by the second factor (F2). Additionally, antimony and mercury constitute one factor (F3). Silver on its own forms one factor (F4) and cadmium on its own constitutes another factor (F5). The first two factors (F1 and F2) account for 68% of the total variance, the first three (F1, F2, F3) account for 79% of the total variance. All five factors account for 92% of the total variance. A plot depicting the factor loadings can be seen in figure 6.26.
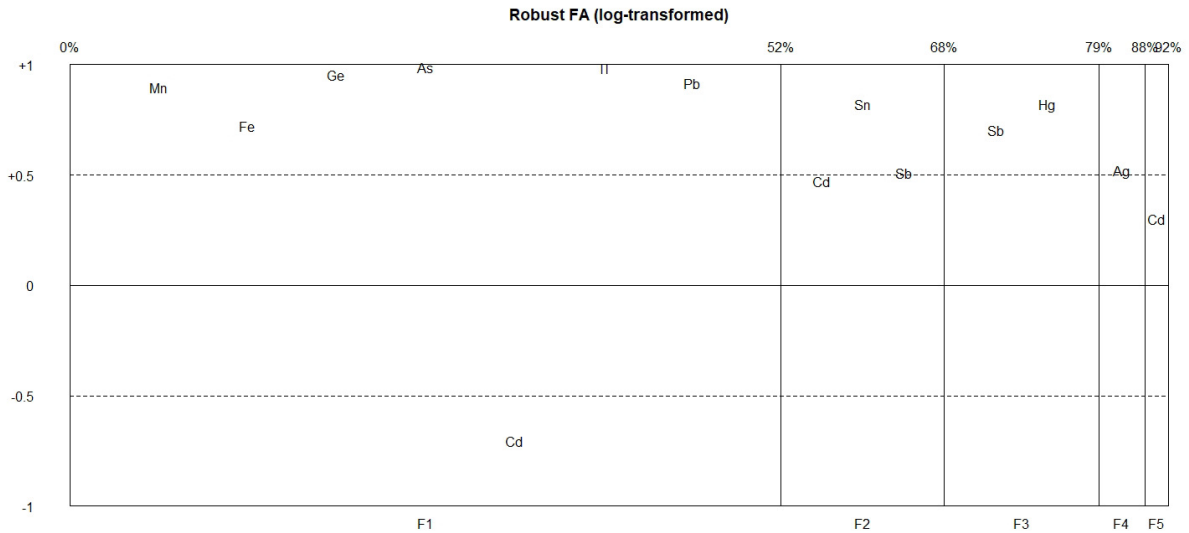
Figure 6.26.: Loading plot depicting the results of the principal factor analysis

6.4. Chemistry of pyrite from the Raibl deposit

Seven spot measurements of pyrite were carried out in the sample R-27 (agglomerated sphalerite type A). The results are presented in table 6.9. Pyrite contains remarkable amounts of arsenic, thallium and lead. Unlike sphalerite, arsenic does not correlate with thallium (D in figure 6.27) or lead (E in figure 6.27). It does, however, correlate with antimony (A in figure 6.27). Nickel does correlate with cobalt (B in figure 6.27). As in sphalerite, thallium and lead correlate well (C in figure 6.27).

spot	manganese	copper	zinc	arsenic	antimony	thallium	lead
R-27-py2	219	$< LOD$	172	7423	55.7	393	10091
R-27-py3	159	$< LOD$	n.a.	14719	27.2	199	3999
R-27-py5	74.5	1.19	n.a.	7378	20.3	905	10627
R-27-py7	132	$< LOD$	120	16079	29.9	191	3902
R-27-py9	75.1	0.97	n.a.	9590	20.5	1027	12082
R-27-py10	91.3	1.05	n.a.	7910	24.3	815	10383
R-27-py11	182	$< LOD$	295	12463	23.7	208	3230

Table 6.9.: Excerpt of LA-ICP-MS results performed on pyrites of sample R-27, numbers are given in $\mu g/g$; LOD = load of detection, n.a. = not applicable due to missing data
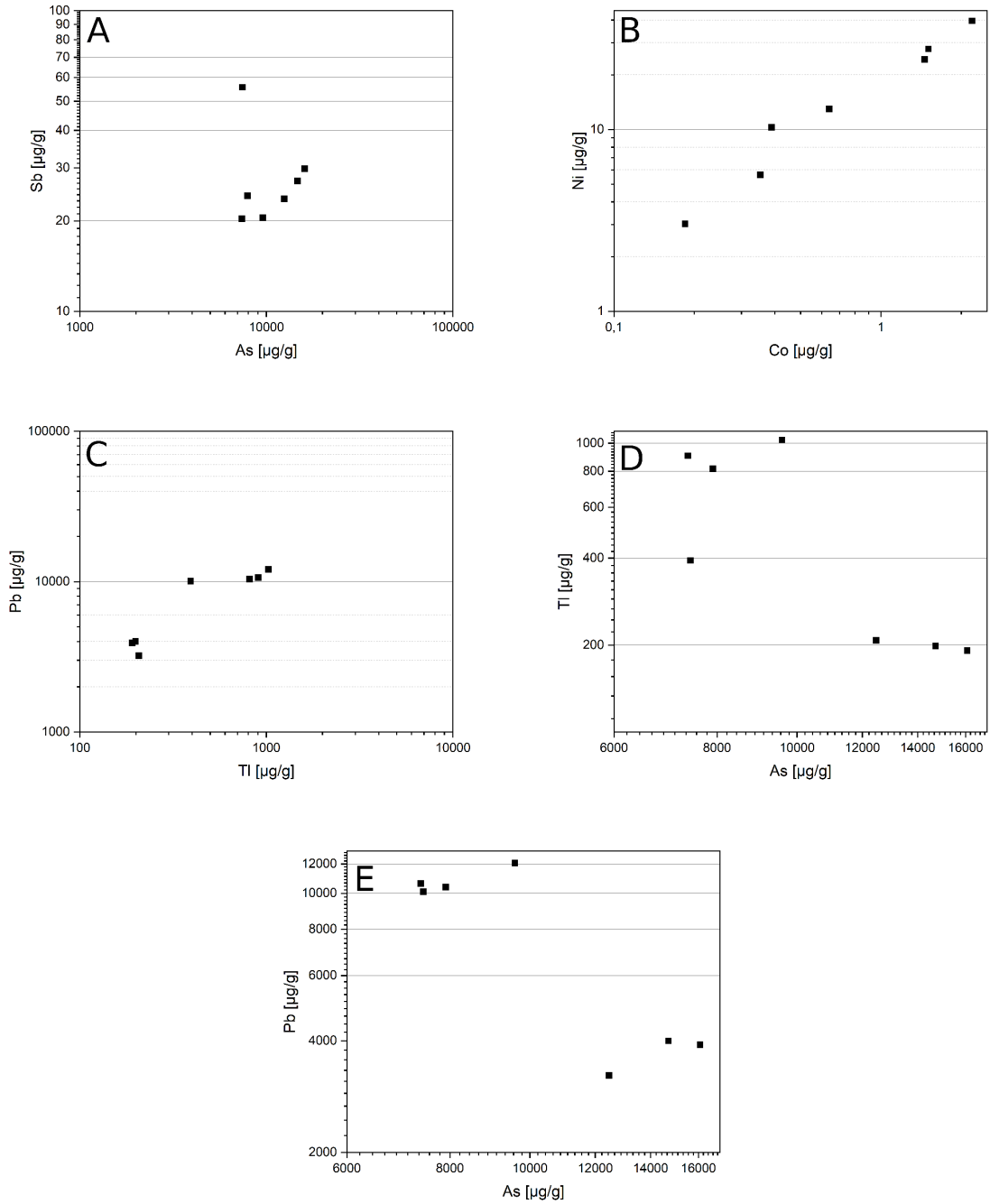
Figure 6.27.: A: Diagram of arsenic and antimony in pyrite; B: Diagram of copper and nickel in pyrite; C: Diagram of thallium and lead in pyrite; D: Diagram of arsenic and thallium in pyrite; E: Diagram of arsenic and lead in pyrite; all pyrite measurements were performed on sample R-27

6.5. Calamine stalactite

Figure 6.28.: side view of the sample

Figure 6.29.: front view of the sample

The macroscopic sample Röhrenerz, seen in figures 6.28 and 6.29, exhibits a tubular form and was classified in the archive as tubular zinc ore (calamine). Since tubular ore is defined as tubes consisting of primary ore minerals, it could be either a true tubular ore or calamine ore, which would rule out a classification as a tubular ore. The examination of a part from the outer layer by Raman spectroscopy and SEM uncovered a mineral assemblage of smithsonite and a mineral, which is likely iron-hydroxide with hemimorphite as an accessory phase. The Raman spectrum of smithsonite can be seen in figure 6.30. The iron-hydroxide is present in the sample as well-formed non-concentric rings surrounded by anhedral smithsonite and anhedral iron-hydroxide (figure 6.31). The iron-hydroxide can also show radial texture. Hemimorphite is present as approximately $10\mu m$ long tabular grains (figure 6.31). SEM revealed that smithsonite in this sample contains significant amounts of iron, while the iron-hydroxide contains significant amounts of zinc.
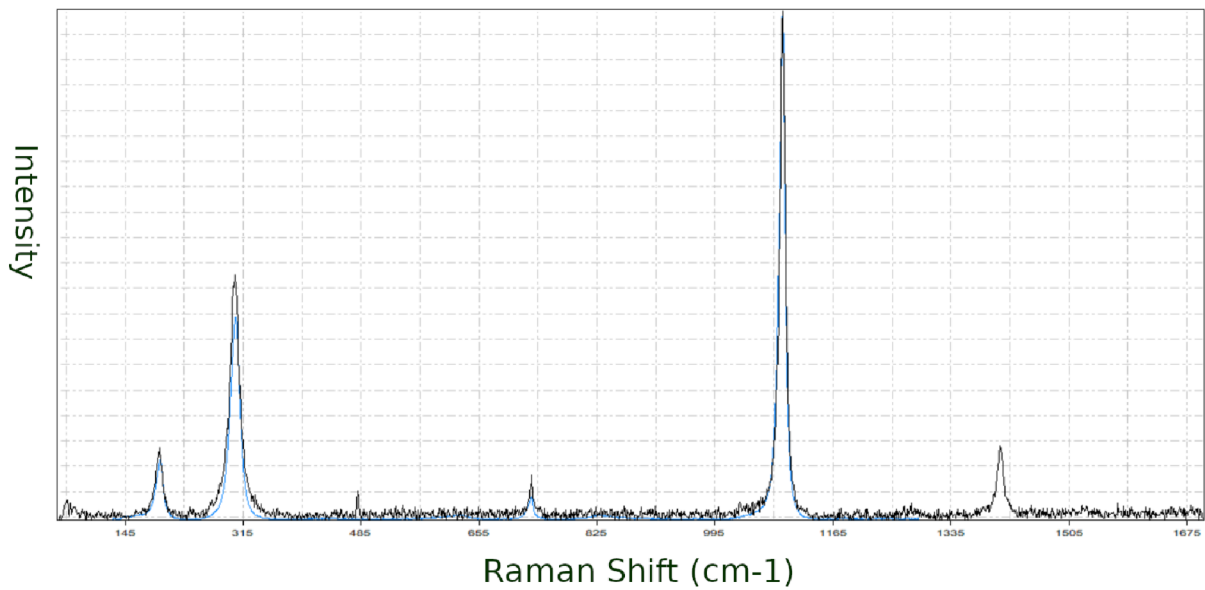
Figure 6.30.: Raman spectrum of smithsonite; in black - measured spectrum, in blue - spectrum proposed by CrystalSleuth (RRUFF identification code: R040051; calculated fit: 97%)
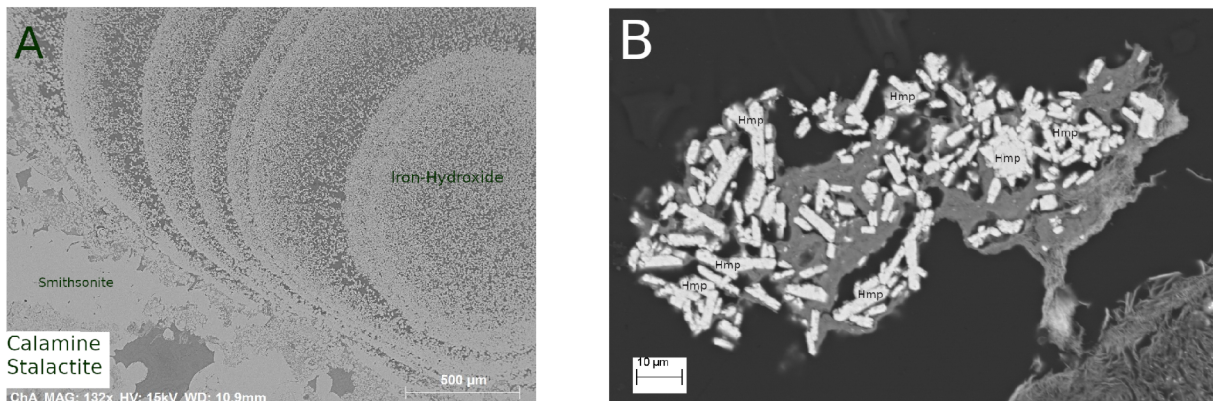
Figure 6.31.: A: Iron-hydroxide rings and smithsonite; B: Hemimorphite grains; both pictures are BSE images

The mineral assemblage proves that the sample should not be classified as a tubular ore, since tubular ore consists mainly of primary ore minerals (galena, sphalerite, pyrite), with secondary minerals only as accessories. The sample Röhrenerz should therefore be categorized as a calamine stalactite, as shown by Kraus (1913) (figure 6.32). Based on this categorization, this sample is not considered when discussing tubular ore.
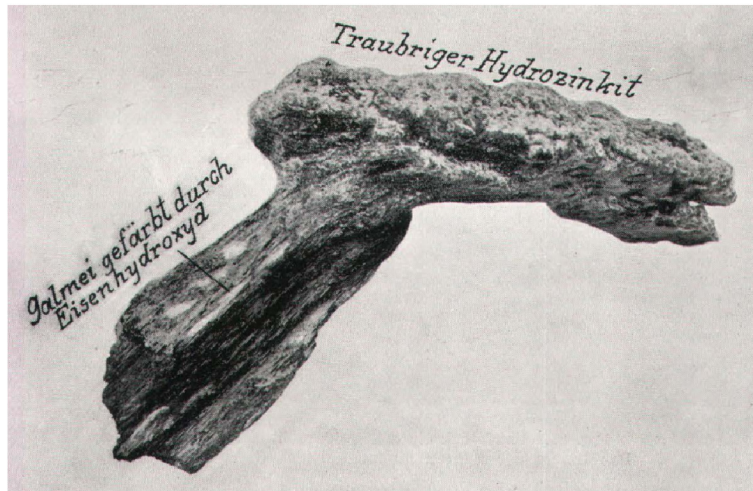
Figure 6.32.: Calamine stalactite from the western calamine deposit. Image from Kraus (1913) (Galmei gefärbt durch Eisenhydroxid = calamine colored by ironhydroxide; Traubiger Hydrozinkit = nodular hydrozincite)

7. Discussion

7.1. Succession of sphalerite types

The formation process of colloform textures is still under debate. Several hypotheses have been proposed, including mechanisms of self-organization (Fowler and L'Heureux 1996; Katsev and L'Heureux 2001; Katsev et al. 2001), mixing of high-temperature metal-bearing fluids and low-temperature, saline fluids containing bacteriogenic H_2S (Wilkinson et al. 2005), coalescence of ions to form clusters in the sphalerite lattice (Bernardini et al. 2004). There is no indication how colloform textures in Raibl were formed, however, it should be noted, that colloform, tubular and disseminate type B textures show similar mineral successions and all three exhibit some form of banding differentiated by color. This may indicate that these textures are formed by similar processes, which are still not completely understood.

Agglomerated sphalerite resembles a variety of sphalerite found in Bleiberg (*Zinkblende B/Sphalerite B*)(Schulz 1959). Both show densely packed, sometimes rounded grains. Agglomerated type B sphalerite and *Zinkblende B* exhibit color zonation disregarding grain boundaries (figure 6.11). *Zinkblende B* shows orange, yellow and red colors after excitation with UV-light, but can also not fluoresce at all. These UV-light colors can also be found in both types of agglomerated sphalerite (figure 6.10 and 6.11). *Zinkblende B* is interpreted as an intermediate texture between disseminated sphalerite and colloform sphalerite. It is more densely packed than disseminated sphalerite and in contrast to colloform sphalerite *Zinkblende B* does still show singular grains, although a color zonation disregarding grain boundaries has already started to show (Schulz 1959). If *Zinkblende B* and the agglomerated sphalerite from Raibl are comparable, the agglomerated sphalerite could be seen as a precursor to the colloform sphalerite and thus any similarities in chemical composition could be seen as a similarity in origin. It would also explain why colloform textures and agglomerated type B sphalerite can occur in such proximity and some samples exhibit a smooth transition of textures (figure 6.14).

The comparison of data linked to color is complicated due to subjectivity of color identification and a discrepancy between macroscopic and microscopic colors. Samples that seem to have a uniform color macroscopically, often reveal a variety of color variation under the microscope. A microscopic investigation should therefore be considered necessary if exact color varieties have to be distinguished. Jicha (1951) described a similar succession of generations of sphalerite and galena at Raibl, as can be seen in the samples used in this study. However neither violet-grey sphalerite nor wurtzite nor marcasite described by Jicha (1951) could be found. The lack of wurtzite could be attributed to recrystallisation to sphalerite (Fleet 1977). The lack of grey sphalerite could be attributed to the subjectivity of color perception.

Sample R-63A, which contains dendritic galena, fits the description of "Schrifterz" (Posepny

1873). Dendritic galena within colloform sphalerite, also described as skeletal galena or knitted galena (gestrickte Bleiglanze) have been found in many low-temperature lead-zinc deposits (Atanassova and Bonev 2006), e.g. in Bleiberg (Schroll 1953a). The galena was supposedly formed first in an open space, later encrusted by sphalerite bands. The galena was subsequently partially dissolved and more sphalerite was deposited in the new gaps (Atanassova and Bonev 2006). This process may play a minor role in the formation of some ores from Raibl. However, since galena in R-63A is often found crosscutting sphalerite structures, it is unlikely that the majority of Raibl ores crystallized in the order proposed by Atanassova and Bonev (2006).

The concentric rings of sphalerite alternating with either porous areas or barite, which were found in some samples, have not been sufficiently described and explained so far in literature. Similar globular structures have been found in other lead-zinc deposits, e.g. Bleiberg in Austria (Kucha et al. 2010) and Olkusz in Poland or Erma Reka in Bulgaria (Atanassova and Bonev 2006). In Bleiberg these structures were interpreted as former biogenic peloids which were transformed into microglobules of sphalerite (Kucha et al. 2010). It cannot be ascertained, if this is also the case for the Raibl samples. A more detailed study of these circular textures and a sulfur isotope study would be needed to explain the formation of these textural varieties of sphalerite.

Brecciated ore surrounded by dolomitic matrix, which has been described in Raibl before (Kraus 1913), can also be seen in three samples used in this study (R-16, R-24, R-29). Sample R-16 also fits the description of ore-grade dark breccia (Brigo and Omenetto 1978).

7.2. Origin of the fern ore

Sphalerite in the fern ore contains high amounts of trace elements (e.g. arsenic, germanium), but the contents all remain within the range of colloform sphalerite. The chemical composition and the mixture of remnant sphalerite texture and smithsonite texture, lead to the conclusion that fern ore is formed when colloform sphalerite is altered to smithsonite. Banded sphalerite surrounding galena remains with rims of altered mineral (smithsonite). The original gangue mineral (dolomite) is broken up and the clasts are surrounded by smithsonitic matrix. Fern ore should therefore be interpreted as an altered colloform sphalerite, not as a separate sphalerite texture.

Holes within the sample may have been originally occupied by an unknown mineral which was destroyed during preparation of the sample or were produced by alteration of the original mineral assemblage. An example of the holes can be seen in figure 7.1. If further investigation of the sample is needed in the future, a water-free preparation method is suggested.
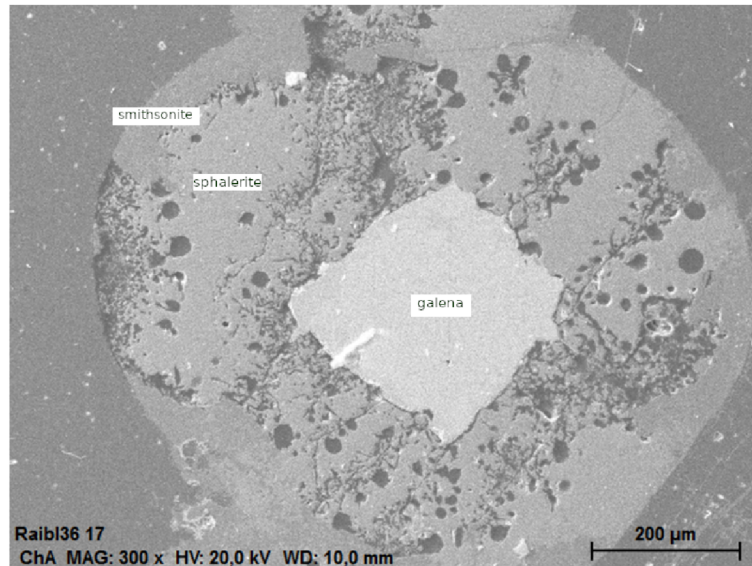
Figure 7.1.: Sphalerite shows distinctive holes, while galena and smithsonite seem untouched; sample R-36; BSE image

Dendritic galena in calamine has only been found in the western calamine deposit (*Westliches Galmeivorkommen*) (Göbl 1903), where calamine shows pseudomorphosis, resembling the banding of colloform sphalerite (Kraus 1913). The fern ore sample in this study is of unknown origin. It shows the pseudomorphosis described above, contains dendritic galena and the sample macroscopically resembles pictures from the western calamine deposit provided by Göbl (1903) (figure 4.11). Therefore it could be concluded, that the fern ore sample of this study also originated from the aforementioned part of the mine.

7.3. Tubular ore

The samples used in this study do not match perfectly with the tubular ore varieties described in literature (Posepny 1873; Pošepny 1887) (see section 4.3.1). Variety 4, which is described as having dolomite as a core, galena surrounding the dolomite and reddish-brown sphalerite as a rim, could be considered the best fit. Variety 3, which has galena as a core followed by sphalerite and grey sphalerite as a rim could be also considered. The white unknown mineral described by Posepny (1887) may be barite, light colored sphalerite or a mixture of both.

Unfortunately, the origin of sample R-67 remains unknown. However, as there are only a few places in the mine, where tubular ore was found, the original location can be narrowed down to a few options. The samples used in this study do not resemble the tubular ores of the *Grotte*, as they are completely surrounded by gangue and sphalerite and not isolated tubes described as by Göbl (1903). Since the locality within the main mineralization was found at a point in time, when the samples were probably already within the collection of the Montanuniversität Leoben, the most likely locations of origin are the *Johanni level* and *the Struggl part*, as these were already known localities for tubular ore before 1918.

In the past, the formation of tubular ore was attributed to fossils or stalactitic growths (Posepny 1873; Di Colbertaldo and Feruglio 1963). No indication was found in the sam-

ples used in this study that tubular ore is formed by sulfide following along structures of fossils (pseudomorphosis), as disscussed by Di Colbertaldo and Feruglio (1963). A stalactitic origin can neither be confirmed nor ruled out. Stalactites of different minerals have been reported for Raibl in the past, e.g. calamine stalactites (Kraus 1913). Samples used in this study included a calamine stalactite described in section 6.5. Both tubular ores and the calamine stalactite exhibit ring-like structures. However, the calamine stalactite shows clearer distinction between the rings, a more reduced mineral assemblage and a repeated pattern. It could be argued that tubular ore formed as a sphalerite stalactite first, which later experienced an overgrowth of galena.

Smoker chimneys found either as recent structures on the sea floor or as fossil chimneys in ore deposits can also exhibit tube-like structures (e.g.pictures shown by Berkenbosch et al. 2012). Low temperature white smoker chimneys contain sphalerite and pyrite among other minerals (Herzig and Hannington 1995). Chimneys can show complex replacement and recrystallization histories (Herzig and Hannington 1995). Barite can be part of the chimneys, while galena and also more complex minerals such as jordanite have been found in connection with smokers (Herzig and Hannington 1995). Jordanite has also been reported in Raibl (Brigo and Cerrato 1994), but was not found in the samples of this study.

Fossil white smoker chimneys dominated by sphalerite, pyrite, barite and quartz, also containing galena and sulfosalts, have been described in volcanogenic massive sulfide (VMS) deposits (Maslennikov et al. 2009). Compared to the samples of this study, they show some similarities in texture (e.g. ring-structures, globular colloform pyrite grains) and trace element composition. Sphalerite in the white smoker fragments shows a low copper, tin, gold, barium, vanadium, uranium content and a higher iron and cadmium content (Maslennikov et al. 2009). They do, however, contain silver, which is only present at low concentrations in samples from Raibl. The white smoker sphalerites show only low concentrations of lead and thallium contents (Maslennikov et al. 2009), which do not fit the trace element composition found in the samples from Raibl. The chimney fragment samples differ slightly in mineral assemblage, as the smoker chimney fragments can contain chalcopyrite, which was not found in Raibl, and quartz, which was not found in tubular ore samples from Raibl. The dolomite found in the Raibl samples is also missing from the chimney samples described by Maslennikov et al. 2009. Interestingly, white smoker chimney samples are linked to low temperatures of approximately 150°C (Maslennikov et al. 2009). The highest temperature calculated for tubular sphalerite from Raibl was 141°C (see discussion of temperature of ore formation ins section 7.8). Chimney structures consisting of barite, sphalerite, galena, colloform pyrite and quartz, lacking chalcopyrite have also been described for Kuroko-type deposits (Shimazaki and Horikoshi 1990).

Recent smokers may occur as zinc-rich chimneys, showing a mineral assemblage of (colloform) sphalerite, globular colloform pyrite/marcasite, barite, galena and a low amount of chalcopyrite. Other sulfide minerals, such as realgar, can also be found. Zinc-rich chimneys form at lower temperature than copper-rich chimneys (> 150 °C). The barite was deposited first, then the sulfides followed (Berkenbosch et al. 2012).

Chimney structures have also been reported for deposits classified as Irish Type Deposits (Larter et al. 1981). Their formation was linked to a temperature below 150°C. The tubes consist of pyrite, barite and in some cases the center is filled with colorless

sphalerite (Larter et al. 1981; Boyce et al. 1983). Sometimes sphalerite and pyrite form an outer rim (Boyce et al. 1983.) The chimneys are interpreted as a part of a feeder zone (Larter et al. 1981; Boyce et al. 1983). Bacterial reduction of sulfates produces the sulfur for the sulfide formation (Boyce et al. 1983).

If tubular ore from Raibl represents former smoker chimneys, it would have formed at even lower temperatures as those calculated for similar fossil examples in volcanogenic massive sulfide (VMS) deposits and measured at recent examples. The different mineralogy may be attributed to different composition of the source of the fluids forming the chimneys, which would have had to lack copper, as no copper-bearing mineral was found within the samples from Raibl and the copper content of sphalerite was found to be low. The presence of dolomite instead of quartz may be attributed to different environments and the difference in trace element composition of sphalerite may also be linked to differences in source. However, smoker chimney structures have never been described in APT deposits. The connection between tubular ore and smoker chimneys needs to be supported by additional arguments besides similarities in mineral assemblage and trace element composition.

The tubular ores from Irish type deposits offer another explanation considering tubes as parts of a feeder zone. The mineral composition of the Irish tubes is similar to the Raibl tubes, but lacks the galena, which is prominent in the tubes of Raibl. If the samples used in this present study are interpreted as feeder tubes, the genetic model of the Raibl deposit would have to be reconsidered.

Based on current knowledge, a definitive genesis of the tubular ore cannot be established. The Montanuniversität Leoben is in possession of other tubular ore samples from Raibl, which have not been included in this research, as this ore type was not the main objective of the study. Similar tubular ores have also been found in Mežica (personal communication by Dr. Aleš Šoster) and Bleiberg (Schroll 1953a). A comparative study focussing on different aspects concerning ore formation could lead to a better understanding of the minerals and genesis of this ore type in the future.

7.4. Layered ore

The samples exhibiting layered ore textures fit the description of Schiefererz (also known as Kalkschiefer) (Göbl 1903; Posepny 1873). The grey sphalerite of the layered textural variety may look similar to agglomerated sphalerite type A at first glance, since both show grey sphalerite grains and their gangue contains quartz, which is not prevalent in samples from Raibl. However, they differ significantly in trace element composition. Layered sphalerite shows low contents of iron, germanium, arsenic, thallium and lead, but high contents of cadmium. Agglomerated type A sphalerite shows also higher amounts of cadmium, but considering arsenic, germanium, lead and thallium contents, this type of sphalerite resembles more the colloform, tubular and agglomerated type B sphalerite than layered sphalerite. Agglomerated sphalerite type A also shows significantly higher median iron contents than all other textural varieties. Taking both petrography and chemical composition into consideration, layered sphalerite and agglomerated type A sphalerite probably were formed by different processes and should not be grouped together.

7.5. Trace element partitioning in sphalerite

As mentioned above, trace element composition of sphalerite from Raibl was studied looking at different aspects, i.e. regarding textures and regarding colors. Colloform, agglomerated sphalerite type B and tubular sphalerite show some similarities in color zonation, but these textures, if disregarding different types and colors, are also similar in trace element contents. These three textures exhibit similar contents of iron, germanium, arsenic, cadmium, thallium and lead. With the exception of iron and cadmium, agglomerated type B sphalerite shows the highest median values of these elements, if disregarding fern sphalerite. Colloform contains the highest contents of aforementioned elements, which may have been caused by the large size of the dataset pertaining to colloform sphalerite (N=318). As stated before, fern ore should be considered a variation of colloform ore, due to its similarities in microscopic and chemical nature. Layered ore contains significantly lower levels of iron, germanium, arsenic, thallium and lead. However its cadmium content is exceptionally high compared to the other textures. Agglomerated type A sphalerite does not fit with the layered sphalerite concerning trace element composition. It shows a higher median cadmium than colloform, tubular and agglomerated type B sphalerite and exhibits the highest median iron content of all textures. Concerning arsenic, germanium, lead and thallium agglomerated type A sphalerite shows lower median contents than colloform, tubular and agglomerated type B sphalerite, but could still be grouped together with these three textural varieties. Based on chemical composition and appearance, colloform, agglomerated type B, fern and tubular sphalerite may have had similar origins, while the layered sphalerite formed differently. Agglomerated type A sphalerite may have had similar origins as the colloform, agglomerated type B, fern and tubular sphalerite, but could have also originated from different processes. A larger sample and data set is needed to clarify this question.

In Triassic sphalerite occurences, five types of sphalerites can be distinguished based on trace element data (Schroll 1983). The characteristics of these types are summarized in table 7.1. Sphalerite of the layered ore could be attributed to sphalerite type 1, as it shows low contents of all trace elements with the exception of cadmium. Colloform sphalerite, agglomerated type B sphalerite and tubular sphalerite could be considered type 3 sphalerite due to their high contents of germanium, arsenic and thallium.

type	high content	low content	additionally considered trace elements
1	Cd	other trace elements	
2	Ge	As,Tl,Cd	high Fe-values
3	Ge,As,Tl		Mo content > V content
4	Cu	Ga	V content > Mo content
5	Cu,Ga		higher contents of Cd and Hg

Table 7.1.: Sphalerite types distinguished by trace element distribution; table compiled after Schroll (1983)

The different color varieties of sphalerite show a lesser difference in trace element composition as the textural varieties of sphalerite. Grey sphalerite shows lower contents of iron, germanium, arsenic, lead and thallium. Brown and red sphalerite show similar compositions. However, the red color variety shows a higher median value of iron, germanium,

arsenic, lead and thallium. Considering cadmium, brown sphalerite shows a higher median value. Yellow sphalerite could be interpreted as a variation of brown based on trace element composition. Green sphalerite and yellow sphalerite show similar trace element contents. Since sometimes yellow and green colors in sphalerite blend into each other, similar trace element compositions could point to a common origin of the color variety or similar formation processes.

Interelement correlations were evaluated using the whole data set. These correlations may be caused by different processes. Arsenic, thallium, germanium, lead, manganese and iron exhibit a significant positive correlation, while cadmium is negatively correlated to arsenic, thallium, germanium, lead and manganese. Figure 7.2 shows the correlation of germanium and arsenic, iron and manganese, as well as cadmium and thallium. The data plotted in the diagram depicting the correlation of germanium and arsenic could be separated into two groups, the main data set and an additional group marked by a red circle. The additional group is composed of data from layered ore (sample R-21) and a tubular ore (sample R-67). The data from R-67 is derived from light colored sphalerite in the middle of the tube. The data from R-21 comes, with one exception, from the light brown sphalerite layer. The lower arsenic contents of R-21 could be attributed to different formation of the ore texture. The lower arsenic contents of R-67 have to remain unexplained.
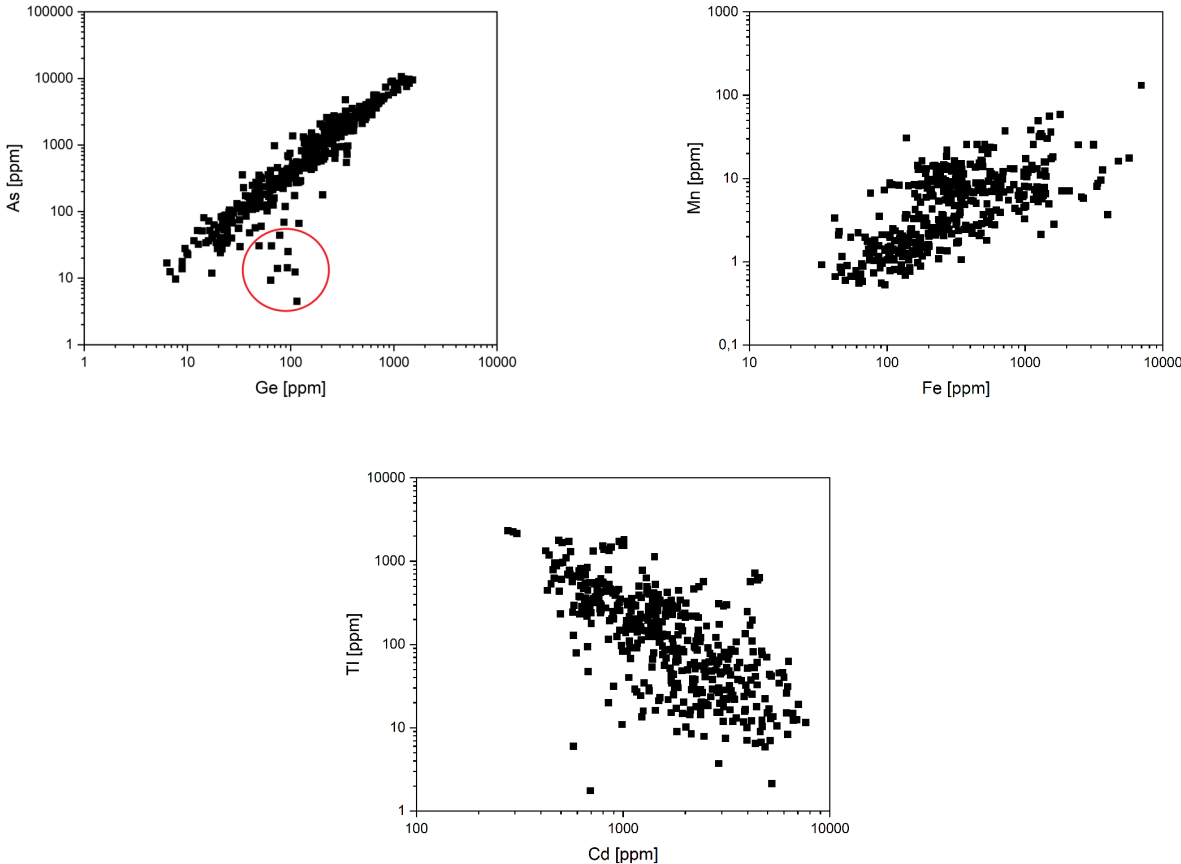
Figure 7.2.: Plots showing correlation of germanium and arsenic, iron and manganes, cadmium and thallium

Goldschmidt's rules for substitution of ions in the crystal lattice explain that ions can substitute each other, if the radii of the ions show a difference of less than 15%. Substitution also depends on the charge of the ions. Charge differences of one unit are unproblematic, as long as the electrical neutrality of the mineral is preserved. Substitution is also dependent on ionic potential (Goldschmidt 1954).

Cadmium and iron can be incorporated into sphalerite through direct substitution (Belissont et al. 2014). These substitution processes may explain the negative correlation of iron and cadmium found in sphalerite from Raibl. The substitution of iron is covered by Goldschmidt's rules (figure 7.3), as the ion radii of zinc and iron are similar. However, the direct substitution of zinc by cadmium cannot be explained by Goldschmidt's rules, as the divalent cadmium shows a significantly larger ion radius than divalent zinc (figure 7.3). Other ions, which could substitute zinc directly in the sphalerite lattice according to Goldschmidt's rules would be manganese, copper and cobalt (figure 7.3), but these were not found in higher concentrations in Raibl sphalerite.
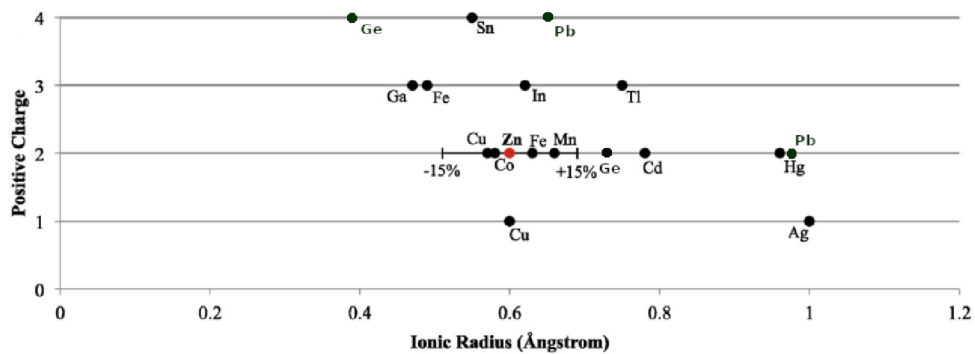
Figure 7.3.: Plot showing ionic radii of various trace element ions in tetrahedral coordination compared to Zn^{2+}; modified after George et al. (2016)

It is assumed that germanium is often present in sphalerite as divalent germanium rather than tetravalent germanium (Cook et al. 2009). Although a direct substitution of divalent zinc by divalent germanium was proposed (Bonnet et al. 2016), germanium should not substitute zinc directly according to Goldschmidt's rules, as the difference in ionic radii is too large (figure 7.3). The substitution process of germanium in sphalerite is not well established, but it is known that germanium uptake of sphalerite depends on the iron content of the mineral (Moh and Jager 1979), which could explain the positive correlation of iron and germanium found in the data set. Two coupled substitutions were proposed to explain the incorporation of germanium in sphalerite ($Ge^{4+} + M^{2+} + vacancy \leftrightarrow 3(Zn, Cd)^{2+}; Ge^{2+} + M^{2+} \leftrightarrow 2(Zn, Cd)^{2+}; M = Pb, Mn$) (Luo et al. 2022). These substitution processes could explain the positive correlation of germanium and lead, as well as germanium and manganese, in the sphalerite samples of Raibl. Additionally, the substitution $vacancy + Ge^{4+} \leftrightarrow 2Zn^{2+}$ was suggested (Bonnet et al. 2016), however, the methods used in this study are not designed to detect possible vacancies.

Neither lead nor thallium content of sphalerite can be explained by direct substitution, due to too large differences in either radius or charge(figure 7.3). Nano-inclusions of the jordanite ($Pb_{14}As_6S_{23}$)-geocronite ($Pb_{14}Sb_6S_{23}$) solid solution series within colloform sphalerite have been used in other deposits to describe elevated contents of lead, arsenic and

antimony (Pfaff et al. 2011). Thallium-rich jordanite has been found in Raibl (Brigo and Cerrato 1994) and sphalerite rich in germanium, arsenic and thallium is known to be associated with thallium-bearing lead-arsenic-sulfosalts (Schroll 1981). Since nano-inclusions cannot be unequivocally identified by LA-ICP-MS, thallium-rich jordanite nano-inclusions could contribute to the strong correlation of thallium, arsenic and lead found within the data set. Nano-inclusions of galena could explain the high lead content of some sphalerite samples. Positive correlations of arsenic and thallium were also found in samples from the Mezica deposit (Potocnik Krajnc 2021). One possible explanation offered for this correlation is a coupled substitution of monovalent thallium (Tl^+) and trivalent arsenic(As^{3+}) replacing divalent zinc (Zn^{2+})(Potocnik Krajnc 2021). If this substitution process is valid, this could also cause the positive correlation of arsenic and thallium in the sphalerite from Raibl. Some of the correlations have to remain unexplained so far, they may be caused by another set of nano-inclusions or unknown substitution mechanisms. Further research using different methods able to identify nano-inclusions is necessary to completely solve these problems.

Factor analysis revealed that manganese, iron, germanium, arsenic, cadmium, thallium and lead contents form a dominant factor. It is known that incorporation of manganese, iron, germanium and cadmium in sphalerite is dependent on temperature (Lange et al. 1985; Cook 1996; Frenzel et al. 2016; Kullerud 1953). This may also be the case in Raibl, however, this cannot be ascertained definitively.

Literature provides different opinions on color of sphalerite originating from Raibl, but also from other deposits. It has been suspected, that red sphalerite from Raibl is richer in iron than other color varieties from this deposit (Jicha 1951). In this study, the red sphalerite contains more iron than green, grey or yellow sphalerite. However, while the median iron content of red sphalerite is higher than the median iron content of brown sphalerite, some brown sphalerites contain higher levels of iron. Therefore, it cannot be concluded that red sphalerite always exhibits higher iron contents.

It has been reported in the past that green sphalerite found in other deposits receives its color from cobalt substituting for zinc ions in the lattice. Even small amounts of cobalt, such as 80ppm, suffice (Rager et al. 1996). However, this does not apply for sphalerite from Raibl, since the cobalt content does not reach this threshold, as the maximum cobalt content found in green sphalerite was 0.19ppm. Therefore, the color has to be caused by other aspects of the crystal lattice.

Darker and lighter shades of color in sphalerite have been linked to varying iron and germanium contents (Hill et al. 1985; Cugerone et al. 2018; Carrillo-Rosúa et al. 2008; Cugerone et al. 2020). Brown sphalerite from Raibl often shows slightly higher iron and germanium contents, if it exhibits darker brown colors (figure 7.4).

Sample R-16 was chosen to exemplify the dependency of color shade, iron and germanium content. This sample, a brecciated colloform sphalerite, consists of clasts of ore (colloform sphalerite, galena and pyrite) and clasts of host rock (fluorite, fluorapatite, sphalerite, pyrite, barite, dolomite) embedded in a matrix containing dolomite, barite and calcite. The brown colloform sphalerite of the largest clast is separated into ten color zones, most of them exhibit dark brown colors, whereas three (4,6 and 10) show lighter

shades of brown (figure 7.5). Color zone 4 and 6 show only slightly lighter colors than the zones deemed dark brown. Color zone 4 exhibits lower germanium contents, but shows a similar iron content as the dark brown zones. Color zone 6 shows distinctively reduced iron and germanium contents compared to the other zones. Color zone 10, which shows a remarkably lighter brown color than the rest of the color zones, also contains the smallest amounts of iron and germanium (figure 7.5).
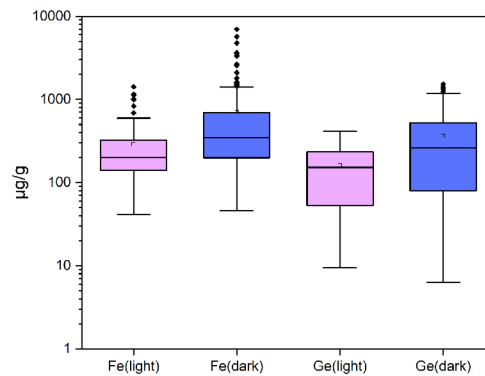
Figure 7.4.: Iron and germanium contents of light brown and dark brown sphalerite
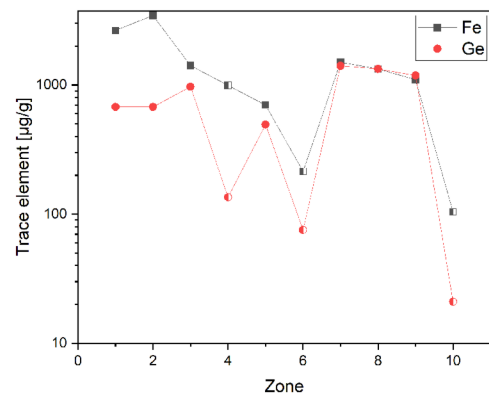
Figure 7.5.: Different color zones of sphalerite in sample R-16 (on the left side) and their respective median contents of iron and germanium (on the right side); lighter color zones are marked by a half-filled symbol

Older literature stated, that the trace element composition of sphalerite from Raibl shows remarkable contents of manganese, iron, germanium, arsenic, cadmium, thallium and other elements (e.g. Schroll 1953a; Schroll 1954; Hegemann 1960; Cerny 1989b) (see also section 4.3.4). However, there are significant differences in the absolute values given by other authors and the data of this study.

Germanium contents between 400 and 450 ppm of germanium were found in sphalerite during ore processing in the Gailitz plant (Arnoldstein in Carinthia). The red colloform

93

sphalerite was reported to contain between 400 and 1000 ppm germanium (Cerny 1989b). In this study, germanium contents between 6.32 and 1524 ppm were found looking at all sphalerites measured. Red colloform sphalerite exhibited between 23.9 and 1032 ppm germanium. The difference between the older results and the results of this study could be due to a smaller sample set in this study compared to the samples used at the processing facility. The difference in germanium contents could also be caused by different analytical methods. Unfortunately, Cerny (1989b) does not give the method of analysis that was used to determine the germanium content.

Brigo and Cerrato (1994) performed a chemical analysis of sample from Raibl consisting of unspecified methods, inductively coupled plasma and atomic absorption spectrometry. It used the whole rock, not differentiating between sulfidic ore minerals (sphalerite, pyrite, galena) and gangue minerals (Brigo and Cerrato 1994). However, since significant amounts of germanium and cadmium can only be found in sphalerite (Brigo and Cerrato 1994), these two elements can be compared to data of the present study (figure 7.6). The data reported in 1994 differs significantly from the data of the study. This may be caused by the fact that the study of Brigo and Cerrato (1994) had to use a combination to methods to measure all the relevant elements, but not LA-ICP-MS as in this study. The study of 1994 analyzed the whole rock sample, while the present study utilized in-situ point measurements, which only represent the chemical composition of a single spot, not the whole crystal. Another aspect is the difference in sample selection. Brigo and Cerrato (1994) used 111 samples from different locations of the mine, whereas this study only uses 19 samples, which may explain the difference in trace element content.

Brigo and Cerrato (1994) describe a positive correlation of germanium, arsenic and thallium, as well as the negative correlation of cadmium to the aforementioned elements. This can be also seen in the data of this study (see section 6.3.5).
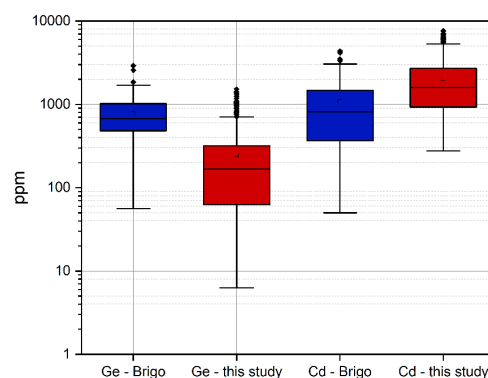
Figure 7.6.: Germanium and cadmium contents found by Brigo and Cerrato (1994) compared to the results of this study

Older literature also provides trace element data typical of sphalerite from Raibl (Schroll 1953b; Schroll 1954; Hegemann 1960; Schroll 1996). The sphalerite was analyzed using a semi-quantitative spectrochemical method. Samples were evaporated on copper

electrodes and the measurements were conducted using a quartz-spectrograph (Zeiss-Quarzspektrograph Q24). Concentrations were estimated visually with an error of ±50%. The resulting trace element compositions are similar to data of this study concerning germanium, arsenic, thallium and cadmium contents (figure 7.7). However, most of the data from the older literature differs completely concerning iron and manganese contents (figure 7.7).This may be caused by contamination of the the sphalerite by pyrite or marcasite.
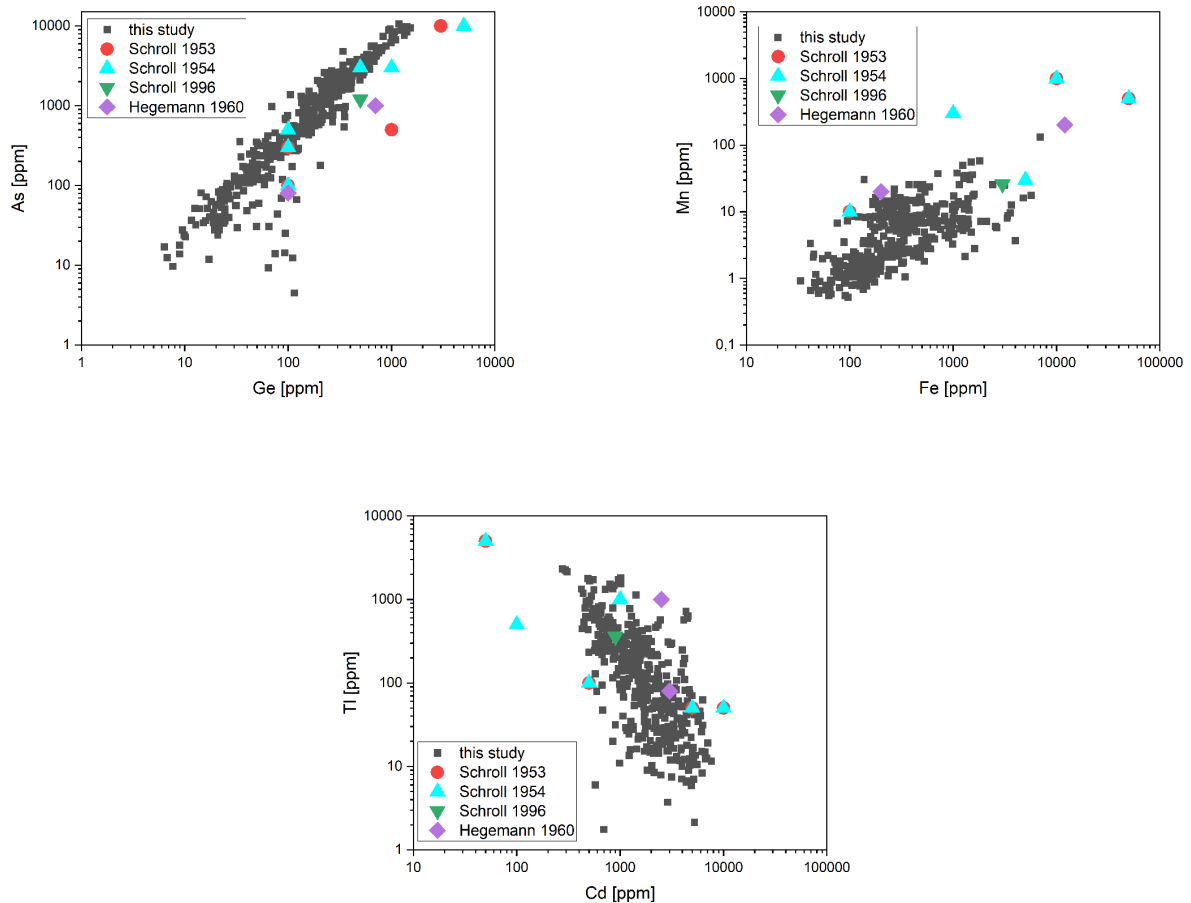
Figure 7.7.: Trace element content (arsenic, germanium, iron, manganese, cadmium and thallium) of sphalerite from the present study compared to data from Schroll (1953b), Schroll (1954), Schroll (1996) and Hegemann (1960)

Additionally, Schroll (1953b) and Schroll (1954) provide higher nickel, silver and tin contents than found in this study. However, the articles state significantly lower antimony contents. Hegemann (1960) also gives higher nickel and silver contents than this study found, while the tin and gallium content reported fit with the results of this study. Schroll (1996) found no silver in sphalerite from Raibl, which fits the data of this study, since the highest silver content found were 7ppm. The low indium, gallium, antimony and mercury contents of the present study also fit with the data provided by Schroll (1996). Schroll (1996) gives for sphalerite from Raibl two element ratios, the ratio of germanium to gallium and the ratio of arsenic to thallium. The ratio of germanium to gallium is given as 50. Since lower contents of gallium were analyzed in this study, a median ratio of 198 was calculated. The ratios of arsenic to thallium are more similar to each other.

Schroll 1996 reported this ratio as 3, while this study found a ratio of 5. The difference in the trace element data found in older literature and the present study may be caused by different sample selection and different methods. The difference in the sample composition may also be important, since the method performed in the present study looks at in-situ compositions, whereas older methods used bulk compositions.

Secondary ion mass spectrometry was used in 1985 to analyze trace element composition of sphalerite from Raibl (Pimminger et al. 1985). A positive correlation of iron, germanium, arsenic and thallium, as well as a negative correlation of cadmium to the aforementioned elements, were found. A similar trend could also be reported for samples from Bleiberg (Pimminger et al. 1985). These correlations were also discovered in the present study (see section 6.3.5).

Statistical data of trace element compositions from 21 analyses of 1 sphalerite sample from Raibl provided by Henjes-Kunst (2014), which were obtained by electron microprobe analyses (EPMA), can be seen in table 7.2. Median contents of iron, germanium, arsenic, cadmium and lead differ from the median contents found in this study. Regarding minimum and maximum contents of these elements, data from Henjes-Kunst (2014) fits in the range of contents found in this study. With the exception of cadmium, Henjes-Kunst (2014) shows higher minimum contents, however, it should be noted that the minimum values of Henjes-Kunst (2014) probably represent the detection limits of the EPMA. All the elements investigated by Henjes-Kunst (2014) show lower maximum contents compared to this study. The differences in trace element composition could be linked to differences in detection limits of EPMA and LA-ICP-MS and the small sample set used by Henjes-Kunst (2014).

	parameter	Fe	Ge	As	Cd	Pb
	min	33.4	6.32	4.49	277	62
present study	max	6973	1524	10618	7640	39955
	median	267	168	799	1593	2477
	min	130	140	20	50	280
Henjes-Kunst (2014)	max	1200	1200	2900	6500	11800
	median	680	690	1800	310	7600

Table 7.2.: Comparison of data from the present study and Henjes-Kunst (2014), min=minimum, max=maximum; all data is given in $\mu g/g$

A smaller sample set of sphalerites from Raibl (8 sample from one sphalerite-bearing hand specimen, 224 spot measurements) was investigated by LA-ICP-MS and the same standards used in this study in 2018 (Onuk 2018). However, the sphalerite samples were classified neither by texture nor by color. Data obtained from Onuk (2018) is plotted in figure 7.8 and is compared to data from this study. Using the same methods and standards should yield similar trace element compositions in sphalerite samples from the same deposit. This is the case for arsenic, thallium and lead (figure 7.8). Iron, germanium and cadmium show significant differences, which may be due to the fact that the trace element compositions presented by Onuk (2018) were derived from one single hand specimen. This study clearly demonstrates that sphalerite trace element composition differ greatly between different textural varieties, which was not taken in consideration

by Onuk (2018), since sphalerites from Raibl were not the main focus of the study. Thus, differences between the datasets are to be expected.
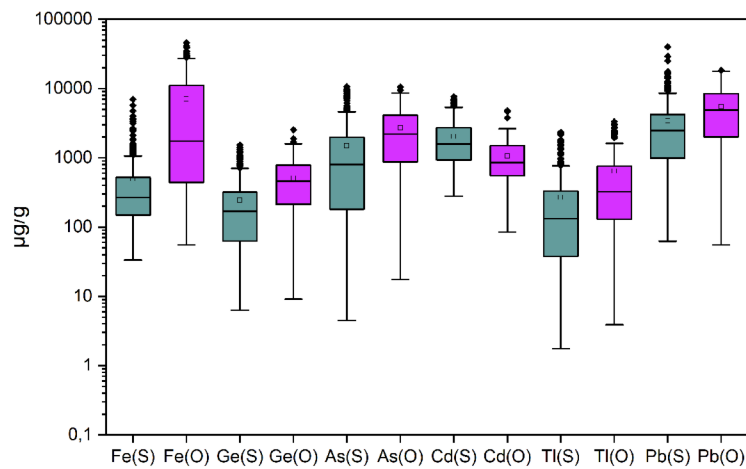
Figure 7.8.: Trace element composition derived from this study (S) compared to data from Onuk (2018) (O)

Liu et al. (2022) proposed several diagrams to distinguish deposit types by using trace element data obtained from several publications concerning sphalerite (Cook et al. 2009; Ye et al. 2011; Ye et al. 2016; George et al. 2015; George et al. 2016; Yuan et al. 2018; Zhuang et al. 2019; Li et al. 2020). Sphalerites from Raibl fit in the MVT section of two of these plots (figure 7.9 and 7.10).
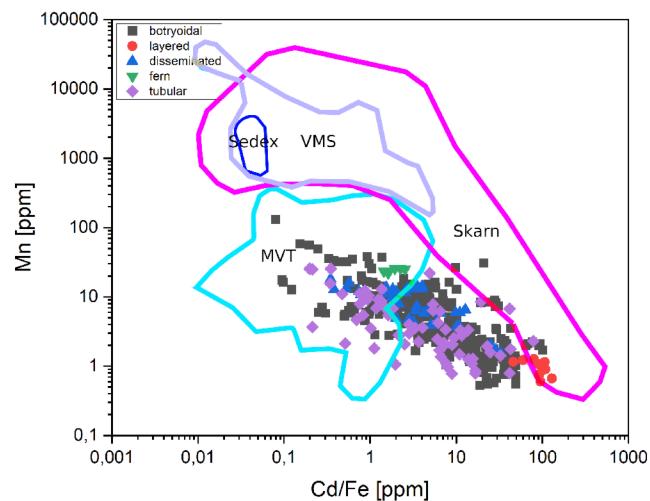
Figure 7.9.: Distinction of deposit type by using the cadmium-iron ratio and the manganese content of sphalerite, modified after Liu et al. (2022)
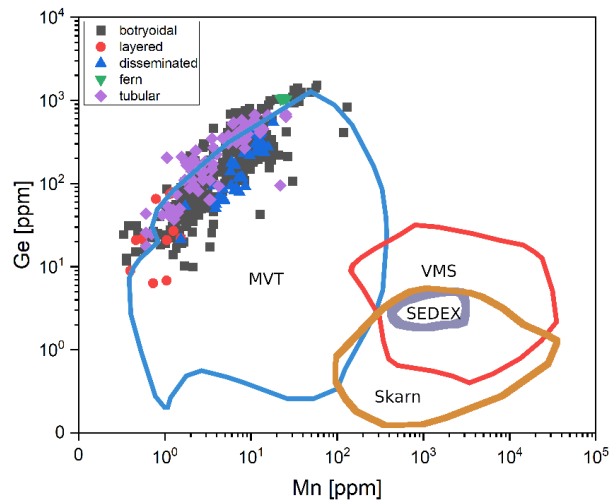
Figure 7.10.: Distinction of deposit type by using the manganese and germanium content of sphalerite, modified after Liu et al. (2022)

7.6. Distribution of sphalerite types and variation of composition throughout the mine

Tubular ore was found in the deeper sections of the *Struggl part*, at the *Johanni level* (figure 7.11), in the *"Grotte"* and an undefined place within the main mineralization (Posepny 1873; Pošepny 1887; Göbl 1903; Di Colbertaldo and Feruglio 1963). The origin of the tubular ore sample RoeA fits with this description, as it supposedly originated from the *Frauen-Johanni level* (figure 7.11). The possible origins of the other tubular ore sample R-67 were discussed above (see section 7.3).

Fern ore may originate from the western calamine deposit (*Westliches Galmeivorkommen*) (figure 7.11), as discussed above in section 7.2. The origin of sample R-10 (*Danieli-Bau, Morgenblatt*) could not be found on a map of the mine or literature pertaining to the Raibl mine. Since *Morgenblatt* generally refers to the eastern faults of the main mineralization, the sample could origin from this part of the mine. The origin of sample R-27, which shows the texture of agglomerated type A texture , is unfortunately unknown.

Colloform sphalerite samples and samples showing a similar agglomerated texture (agglomerated sphalerite type B) that were used in the present study originated from the *Sebastiani level*, the *Johanni level*, the *Franz level* and the *Frauen-Johanni level* (figure 7.11). These samples show interesting differences depending on origin. Samples from the *Sebastiani level* show lower median contents of iron, germanium, arsenic, thallium and lead. The sample from the *Frauen-Johanni level* shows the highest median contents of iron, germanium, arsenic, thallium and lead. The samples from the *Franz level* and the *Johanni level* are between these two extremes. The samples from the *Sebastiani level* show the higher median contents of cadmium. The *Sebastiani level* is in the south of the main mineralization, while the *Frauen-Johanni level* is further in the north of the main mineralization (figure 7.11). The results of the present study fit with the trend reported

by Brigo and Cerrato (1994), who found that the northern part of the mine was enriched in germanium, thallium and arsenic, while the contents of these elements decreased in the southern part of the mine and the cadmium content increased.

Sample R-16 is a breccia containing dark clasts of ore (colloform sphalerite, galena, pyrite), as well as dark clasts consisting of fluorite, fluorapatite, sphalerite, pyrite, barite, dolomite in a white matrix containing dolomite, barite and calcite. According to records, this sample comes from the contact of the ore-bearing dolomite and the Raibl Group. This sample fits the description of ore-grade dark breccia (Brigo and Omenetto 1978) both in texture and location.

The origin of the layered ore was given as *Kalkschieferzone, Südschlagmittel*. Unfortunately, the location of *Südschlagmittel* could not be identified within maps or literature.

Since several colors can be identified within one sphalerite sample, e.g. by normal light microscopy, a correlation of color varieties of sphalerite and location of origin could not be identified. An overall macroscopic descriptions may lead to a different conclusion, a larger sample set would be required for this task. In the past, this has already been attempted, red sphalerite was predominantly found in the north, yellow sphalerite in the south (Di Colbertaldo 1950; Cerny 1989b).
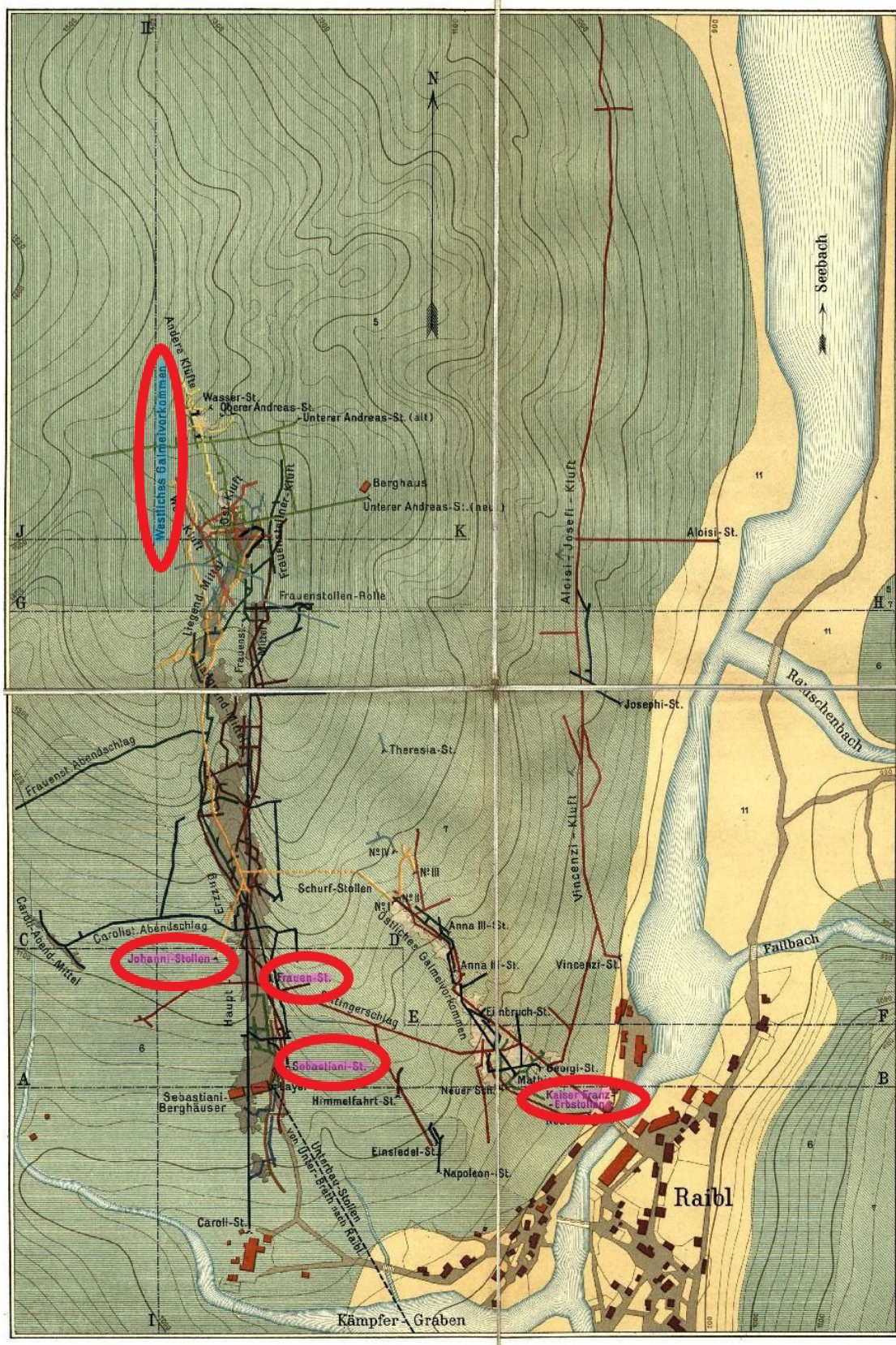
Figure 7.11.: Map of the Raibl mine in 1903, modified after Göbl (1903), known places of origin of the samples used in the study have been marked pink, if present in the map; suspected places of origin have been marked blue

Trace Element	Sebastiani level	Frauen-Johanni level	Franz level	Johanni level
Fe	201	346	241	309
Ge	83.2	332	229	169
As	318	1996	1321	1134
Cd	1830	650	1434	1223
Tl	78.2	354	205	213
Pb	1138	4542	3135	3793

Table 7.3.: Median values of iron, germanium, arsenic, cadmium, thallium, lead in colloform and agglomerated type B sphalerite; sorted after origin of the sample

7.7. Pyrite

It has been stated in the past that pyrite from Raibl contains arsenic (Tornquist 1931). This has been also found in this study (see table 6.9). Pyrite does not contain significant amounts of germanium and cadmium, as stated by Brigo and Cerrato (1994). The germanium content ranges from 0.76ppm to below detection limit, while the cadmium content ranges from 4.07ppm to below detection limit.

Pyrite of Raibl shows higher contents of manganese and arsenic than sphalerite of Raibl. Arsenic can substitute sulfur in the crystal lattice of pyrite (Abraitis et al. 2004). Goldschmidt's rules for substitution state that ions can substitute each other, if the radii of the ions do not differ more than 15%. Substitution also depends on the charge of the ions. Charge differences of one unit are not a problem, as long as electrical neutrality of the mineral is maintained. Ionic potential also influences substitution (Goldschmidt 1954). Divalent manganese in octahedral coordination has a ionic radius of 0.83 Ångstrom and divalent iron of the same coordination a ionic radius of 0,78 Ångstrom (figure 7.12). The difference of these radii is small enough, that according to Goldschmidt's rules manganese could substitute iron in the pyrite. This would explain the significant amounts of manganese found in pyrite from Raibl.

Both pyrite and sphalerite show low nickel, cobalt, copper and indium contents. Copper is known to occur in pyrite within inclusions of other phases (Huston et al. 1995). Nickel and cobalt directly substitute iron in the crystal lattice ($Fe^{2+} \leftrightarrow (Ni^{2+}, Co^{2+})$) (Abraitis et al. 2004), which fits with Goldschmidt's rules, as the differences in the radii of iron, nickel and copper are smaller than 15% (figure 7.12).

Indium is generally not found in pyrite (Cook et al. 2011). Sphalerite shows higher antimony, thallium and lead contents than pyrite. Reasons for the trace element composition of sphalerite are discussed above. Lead is thought to occur in pyrite rather as inclusions than as part of the crystal lattice. Thallium may be part of a coupled substitution, in which Tl^{3+} substitutes Fe^{2+}, whereas $[AsS]^{2-}$ replaces $[S_2]^{2-}$ in the pyrite lattice (Cook and Chryssoulis 1990; Huston et al. 1995). However, it should be noted that in the pyrite of Raibl arsenic and thallium do not correlate. Antimony is present in pyrite as part of other phases occurring as inclusions in pyrite (Huston et al. 1995).
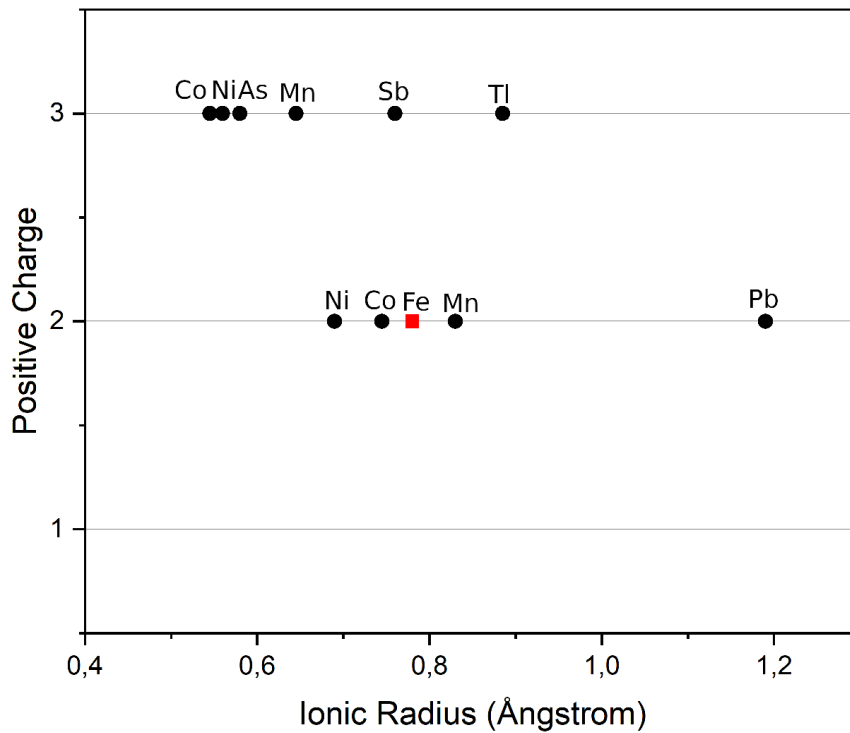
Figure 7.12.: Plot showing ionic radii of various trace element ions in octahedral coordination compared to Fe^{2+}; compiled after Shannon 1976

The pyrites from Raibl are plotted in the binary diagram of Co/Sb in pyrite versus Se/As in pyrite (figure 7.13), which gives possible provenance of pyrites based on their content of cobalt, antimony, selenium and arsenic (Duran et al. 2015). The Raibl pyrites are located outside of the VHMS field, distinctively distant from the magmatic section of the diagram. Given that these pyrites originate from a low-temperature MVT or APT deposit not linked to any magmatism, their position in this diagram fits the formation conditions of the deposit.
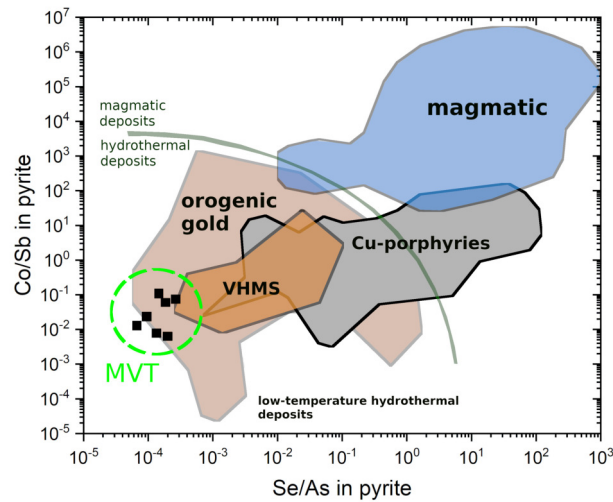
Figure 7.13.: Binary diagram of Co/Sb in pyrite versus Se/As in pyrite with data from Raibl (black squares); redrawn after Duran et al. (2015)

Petrini et al. (2016) suggested that mostly oxidation of pyrite, not sphalerite, was the cause for elevated thallium contents of the water found near the Raibl mine, as the lowest thallium contents were found in water samples with the highest zinc content. Petrini et al. (2016) also found tens of ppm of thallium in pyrite from Raibl. As seen in chapter 6.3, both pyrite and sphalerite from Raibl show significant contents of thallium. Pyrite exhibits higher contents of thallium than given by Petrini et al. (2016). The reason for the chemical composition of the water samples found by Petrini et al. (2016) may lie in the oxidation and alteration of the sulfidic ore. Pyrite disappears during calamine formation (e.g. Kraus 1913) and no pyrite can be found in the calamine section, only small amounts of iron-oxides, limonite and an ochre containing iron are present. Zinc remains largely within the deposits as part of the calamine ore, smithsonite and hydrozincite (see 4.3.2). These minerals can also be precipitated and do not have to occur in-situ (Barago et al. 2022). It has been speculated that the main source for zinc-ions in the water near the Raibl mine are secondary zinc minerals, not sphalerite (Barago et al. 2022). This could account for the low zinc contents found in water, accompanied by high thallium contents from completely decayed pyrite, while the thallium found in sphalerite may remain in the calamine ore. For a better understanding of the connection between primary ore, secondary ore, alteration and resulting mine drainage more detailed investigations are needed.

7.8. Temperature of ore formation

The GGIMFis (Ga, Ge, In, Mn, Fe in sphalerite) geothermometer was proposed by Frenzel et al. (2016). It estimates temperature of formation of sphalerite assuming that all elements used are incorporated in the crystal lattice and are not present as inclusions (Frenzel et al. 2016). The geothermometer yielded a median formation temperature of 88 ± 6 °C for the Raibl sphalerite in general. This temperature interval fits well with the classification of Raibl as a low-temperature APT deposit, as this type does not exceed formation temperatures of 200°C (Schroll 1996) and similar deposits also yielded low for-

mation temperature. Sphalerite from Mezica produced a median formation temperature of 100°C using the same geothermometer (Potocnik Krajnc 2021).

Regarding the formation temperatures obtained for individual textures and colors (see table 7.4), a similar picture as in the geochemical composition can be seen. Colloform sphalerite, agglomerated sphalerite type A and B, as well as tubular sphalerite, which are mostly rich in iron, germanium, arsenic, thallium and lead, produce similar formation temperatures. Meanwhile the layered sphalerite, the cadmium-rich texture, shows a significantly lower formation temperature. Since geochemical data of fern sphalerite encompasses a very low number of data sets, it was not considered in the calculations obtaining formation temperatures of individual textures.

Brown, green and yellow sphalerite, which show similar trace element composition (high in iron, germanium, arsenic, thallium and lead), also show a similar formation temperature. Red sphalerite, which shows higher median values in the trace elements, has a slightly higher formation temperature. The cadmium-rich grey sphalerite has a lower formation temperature compared to the other color varieties.

sphalerite	median formation temperature
whole data set	88 ± 6
colloform sphalerite	90 ± 6
layered sphalerite	59 ± 10
agglomerated sphalerite type A	107 ± 4
agglomerated sphalerite type B	104 ± 4
tubular sphalerite	99 ± 5
brown sphalerite	87 ± 6
red sphalerite	98 ± 5
grey sphalerite	83 ± 7
green sphalerite	89 ± 6
yellow sphalerite	88 ± 6

Table 7.4.: Median formation temperatures of different sphalerite textures and color variety, as well as the whole data set; all values are given in °C

To see if there was a temperature trend based on location of origin of the sphalerite, the formation temperatures of different color varieties of colloform sphalerite and agglomerated sphalerite (type B) were calculated (table 7.5). Sphalerites from the *Sebastiani level* in the south of the main mineralization yield lower formation temperatures compared to sphalerites originating from the more northern *Johanni level* and the more distant *Franz level*. However, the sphalerites coming from the northern *Frauen-Johanni level* show also low formation temperatures. With the exception of the sphalerites from the *Franz level*, the early sphalerite (light brown, yellow and grey) show the lowest formation temperatures. The second generation of sphalerite (dark brown and red) shows the highest formation temperature in samples from *Sebastiani level* and *Johanni level*. The last generation of sphalerite (green) shows lower temperatures or intermediate temperatures compared to the other sphalerite generations.

The formation temperatures do not show a distinctive trend based on location. This may be due to the fact that the calculations were based on data from only 8 samples and the description of the origin of the samples is not precise. To reach a better understanding of the variance in formation temperature within the Raibl mine, larger sample sets and data sets, combined with a more exact description of sample origin, would be required.

sphalerite origin	sphalerite color	median formation temperature
Sebastiani level	light brown, yellow, grey	84 ± 7
	dark brown and red	92 ± 6
	green	86 ± 6
Johanni level	light brown, yellow, grey	100 ± 4
	dark brown and red	105 ± 4
	green	93 ± 5
Franz level	light brown, yellow, grey	110 ± 14
	dark brown and red	107 ± 15
	green	103 ± 15
Frauen-Johanni level	light brown, yellow, grey	72 ± 8
	dark brown and red	75 ± 8
	green	81 ± 7

Table 7.5.: Median formation temperatures of colloform and agglomerated type (B) sphalerite; sorted after origin and color; all values are given in °C

For sphalerite in Mezica it has been discovered, that sphalerite types rich in manganese, iron and germanium exhibit higher formation temperatures than sphalerite types rich in cadmium and copper (Potocnik Krajnc 2021). This pattern can also be seen in the temperature results of this study. However, these results should be observed with caution. The geothermometer is based upon trace element compositions and trace elements can be remobilized after formation of the sphalerite (Wagner and Cook 1998). This could lead to different formation temperatures, i.e. this could mean that the GGIMFis geothermometer yields wrong results for the sphalerite types from Raibl that are poorer in trace elements.

8. Conclusions

Sphalerite from the Alpine carbonate-hosted lead-zinc deposit Raibl was investigated by microscopy, photography under UV-light, Raman spectroscopy, SEM and LA-ICP-MS. The results provide new data that link textural and color varieties of sphalerites with trace element compositions. For the first time a tubular ore sample was investigated by LA-ICP-MS.

Sphalerite, galena and pyrite are the primary ore minerals found within the sample. No wurtzite or marcasite could be identified. The gangue minerals consist mainly of dolomite, which is often accompanied by barite. In some cases quartz could be found in the gangue. Calcite is rare. Secondary minerals detected are smithsonite, anglesite and cerussite.

Sphalerite occurs as five color varieties (brown, red, grey, green, yellow). For this study, the sphalerites were divided into five textures (colloform, layered, agglomerated, fern and tubular sphalerite). The agglomerated texture was further divided into a type A and a type B. All textures can be considered epigenetic textures.

Colloform sphalerite, agglomerated type B sphalerite and tubular sphalerite show some forms of banding and a similar mineral succession. Early lighter colored sphalerite is followed by darker colored sphalerite. Both phases of sphalerite are partially replaced galena and associated green sphalerite. Colloform sphalerite, agglomerated type B sphalerite and tubular sphalerite show similarities in color zonation and trace element composition. Fern ore should be considered an altered variation of colloform sphalerite based on similarities in texture and trace element composition. Therefore, colloform sphalerite, agglomerated type B sphalerite, tubular sphalerite and fern ore may have been formed by similar processes. Over time several formation processes of tubular and colloform sphalerite were proposed. This study did not come to a conclusive answer regarding formation. Further study of samples from Raibl and similar deposits would be required to reach a satisfying conclusion.

Layered ore is composed of several layers containing ore minerals and gangue minerals. Agglomerated type A sphalerite is composed of distinct grains showing a uniform grey color. Layered ore and agglomerated type A sphalerite are both distinctively different in trace element composition compared to each other and the other textural varieties of sphalerites. Layered sphalerite weas probably formed by different processes than colloform sphalerite, agglomerated type B sphalerite, tubular sphalerite and fern ore. It remains unclear if agglomerated type A sphalerite should be grouped with colloform sphalerite, agglomerated type B sphalerite, tubular sphalerite and fern ore or if it indicates a separate formation process.

The color varieties of sphalerite are not as distinctively different in trace element composition as textural varieties. Brown and red show similar compositions. Darker and lighter

shades in brown sphalerites are linked to varying iron and germanium contents. The hypothesis that red sphalerite contains significantly more iron than all other color varieties of sphalerite could not satisfyingly confirmed. Yellow and green sphalerite show similar trace element compositions. Grey sphalerite shows lower contents of trace elements compared to other color varieties. Possible processes of trace element incorporation in sphalerite were discussed, but additional studies are required to explain the trace element content of sphalerite sufficiently.

The overall trace element compositions of sphalerite of Raibl fit well with previous studies (e.g. Henjes-Kunst 2014). Layered sphalerite matches the description of type 1 sphalerite, the other sphalerite textures the description of type 3 sphalerite of Schroll (1983). The change in trace element composition based on location in the Raibl mine described by Brigo and Cerrato (1994) was also found in the samples of this study which could be linked to a documented original location in the mine.

The trace element compositions of sphalerite of Raibl were plotted in the MVT field in diagrams provided by Liu et al. (2022). This fits with the known classification of Raibl as a MVT deposit.

Arsenic, thallium, germanium, lead, manganese and iron exhibit significant positive correlation. Cadmium is negatively correlated to arsenic, thallium, germanium, lead and manganese. Factor analysis revealed that manganese, iron, germanium, arsenic, cadmium, thallium and lead contents in sphalerite form a dominant factor.

Two sets of element distribution maps were produced with the help of LA-ICP-MS. They revealed, that the distribution of trace elements in sphalerite is more intricately zoned than indicated by differences in color and texture. The aforementioned correlations of trace elements can also be seen in the element distribution maps.

The GGIMFis geothermometer yielded a formation temperature of 88 ± 6 °C. This temperature is in accordance with the classification of Raibl as a low-temperature deposit and is similar to formation temperatures calculated for comparable deposits. Colloform, agglomerated and tubular sphalerite show higher formation temperatures than layered sphalerite. Brown, yellow and green sphalerite show similar formation temperature. Red sphalerite has a slightly higher formation temperature and grey sphalerite exhibits a lower formation temperature.

For comparison purposes, an additional sample originally classified as tubular ore was investigated by microscopy, SEM and Raman spectroscopy. Based on mineral assemblage (smithsonite, iron-hydroxide and hemimorphite) the sample was reclassified as calamine stalactite.

Additionally to sphalerite, pyrite from one sample (R-27) was investigated by LA-ICP-MS. Pyrite contains remarkable amounts of arsenic, thallium and lead. Very low contents of germanium and cadmium was detected in pyrite. Possible processes of trace element incorporation in pyrite were discussed, but additional studies are required to explain the trace element content of pyrite sufficiently. Thallium found in pyrite may be the source of the thallium contamination found in the surroundings of the mine, as described by Petrini

et al. (2016).

Bibliography

Abraitis, P. K., R. A. D. Pattrick, and D. J. Vaughan (2004). "Variations in the compositional, textural and electrical properties of natural pyrite: a review". In: *International Journal of Mineral Processing* 74.1-4, pp. 41–59.

Álvarez-Ayuso, E., V. Otones, A. Murciego, A. García-Sánchez, and I. Santa Regina (2013). "Zinc, cadmium and thallium distribution in soils and plants of an area impacted by sphalerite-bearing mine wastes". In: *Geoderma* 207, pp. 25–34.

Anderson, G. M. and R. W. Macqueen (1982). "Ore deposit models-6. Mississippi Valley-type lead-zinc deposits". In: *Geoscience Canada*, pp. 108–117.

Andreatta, C. (1930). "Bianchite, nuovo minerale". In: *Atti della Accademia nazionale dei Lincei Serie VI* 41, pp. 760–769.

Anonymus (1910). "Die Einsturzkatastrophe in Raibl". In: *Österreichische Zeitschrift für Berg- und Hüttenwesen* 58, pp. 31–32.

Anthony, J. W., R. A. Bideaux, K. W. Bladh, and M. C. Nichols (1990). *Handbook of Mineralogy*. Tucson Arizona, USA: Mineral Data Publishing.

Assereto, R., A. Desio, D. Di Colbertaldo, and L. D. Passeri (1968). *Note illustrative della Carta Geologica d'Italia. Foglio 14 A Tarvisio*. Rome: Servizio Geologico d'Italia.

Atanassova, Radostina and Ivan K. Bonev (2006). "Two crystallographically different types of skeletal galena associated with colloform sphalerite". In: *Mineral. Petrol* 44, pp. 1–18.

Baker, A., R. Brooks, and R. Reeves (1988). "Growing for gold... and copper... and zinc". In: *New Scientist*, pp. 44–48.

Bao, Zhongwen, Tom Al, Jeff Bain, Heather K. Shrimpton, Y. Zou Finfrock, Carol J. Ptacek, and David W. Blowes (2022). "Sphalerite weathering and controls on Zn and Cd migration in mine waste rock: An integrated study from the molecular scale to the field scale". In: *Geochimica et Cosmochimica Acta* 318, pp. 1–18.

Barago, Nicolò, Stefano Covelli, Mara Mauri, Sara Oberti di Valnera, and Emanuele Forte (2021). "Prediction of Trace Metal Distribution in a Tailings Impoundment Using an Integrated Geophysical and Geochemical Approach (Raibl Mine, Pb-Zn Alpine District, Northern Italy)". In: *International Journal of Environmental Research and Public Health* 18.1157, p. 1157. ISSN: 1661-7827. DOI: 10.3390/ijerph18031157. URL: https://www.mdpi.com/1660-4601/18/3/1157.

Barago, Nicolò, Elena Pavoni, Federico Floreani, Matteo Crosera, Gianpiero Adami, Davide Lenaz, and Stefano Covelli (2022). "Hydrogeochemistry of thallium and other potentially toxic elements in neutral mine drainage at the decommissioned PbZn Raibl mine (Eastern Alps, Italy)". In: *Journal of Geochemical Exploration*, p. 107129.

Bauer, Matthias E., Mathias Burisch, Jörg Ostendorf, Joachim Krause, Max Frenzel, Thomas Seifert, and Jens Gutzmer (2019). "Trace element geochemistry of sphalerite in contrasting hydrothermal fluid systems of the Freiberg district, Germany: insights from LA-ICP-MS analysis, near-infrared light microthermometry of sphalerite-hosted fluid inclusions, and sulfur isotope geochemistry". In: *Mineralium Deposita* 54.2, pp. 237–262.

Belissont, Rémi, Marie-Christine Boiron, Béatrice Luais, and Michel Cathelineau (2014). "LA-ICP-MS analyses of minor and trace elements and bulk Ge isotopes in zoned Ge-rich sphalerites from the Noailhac-Saint-Salvy deposit (France): Insights into incorporation mechanisms and ore deposition processes". In: *Geochimica et Cosmochimica Acta* 126, pp. 518–540.

Berkenbosch, H. A., C. E. J. De Ronde, J. B. Gemmell, A. W. McNeill, and K. Goemann (2012). "Mineralogy and formation of black smoker chimneys from Brothers submarine volcano, Kermadec arc". In: *Economic Geology* 107.8, pp. 1613–1633.

Bernardini, G. P., M. Borgheresi, C. Cipriani, F. Di Benedetto, and M. Romanelli (2004). "Mn distribution in sphalerite: an EPR study". In: *Physics and chemistry of minerals* 31, pp. 80–84.

Bonnet, Julien, Régine Mosser-Ruck, Marie-Camille Caumon, Olivier Rouer, Anne-Sylvie Andre-Mayer, Jean Cauzid, and Chantal Peiffert (2016). "Trace element distribution (Cu, Ga, Ge, Cd, and Fe) in sphalerite from the Tennessee MVT deposits, USA, by combined EMPA, LA-ICP-MS, Raman Spectroscopy, and crystallography". In: *The Canadian Mineralogist* 54.5, pp. 1261–1284.

Boulton, Adrian, Daniel Fornasiero, and J. Ralston (2005). "Effect of iron content in sphalerite on flotation". In: *Minerals engineering* 18.11, pp. 1120–1122.

Boyce, Adrian Joseph, Max L. Coleman, and Michael J. Russell (1983). "Formation of fossil hydrothermal chimneys and mounds from Silvermines, Ireland". In: *Nature* 306, pp. 545–550.

Bragg, W. (1913). "The Structure of the Diamond". In: *Nature* 91, p. 557.

Brigo, L. and P. Cerrato (1994). "Trace element distribution of Middle-Upper Triassic carbonate-hosted lead-zinc mineralizations: the example of the Raibl deposit (Eastern Alps, Italy)". In: *Sediment-hosted Zn-Pb ores*. Springer, pp. 179–197.

Brigo, L., L. Kostelka, P. Omenetto, H.-J. Schneider, E. Schroll, O. Schulz, and I. Štrucl (1977). "Comparative reflections on four Alpine Pb-Zn deposits". In: *Time-and stratabound ore deposits*. Springer, pp. 273–293.

Brigo, L. and P. Omenetto (1978). "The lead and zinc ores of the Raibl (Cave del Predil-northern Italy) Zone: new metallogenic data". In: *Ergebnisse der österreichischen Projekte des Internationalen Geologischen Korrelationsprogramms (IGCP) bis 1976/Scientific Results of the Austrian Projects of the International Geological Correlation Programme (IGCP) Until 1976*. Springer, pp. 103–110.

Brusca, C., Maurizio Gaetani, Flavio Jadoul, and G. Viel (1981). "Paleogeografia ladino-carnica e matallogenesi del Sudalpino". In: *Memorie della Societa Geologica Italiana* 22, pp. 65–82.

Calligaris, Chiara, Glenda Nicola, Giacomo Casagrande, Luca Zini, and Franco Cucchi (2017). "Debris Flow Hazard Assessment (Cave del Predil—NE Italy)". In: *Workshop on World Landslide Forum*. Springer, pp. 369–376.

Carrillo-Rosúa, Javier, Salvador Morales-Ruano, and Purificación Fenoll Hach-Alí (2008). "Textural and chemical features of sphalerite from the Palai-Islica deposit (SE Spain): implications for ore genesis and color". In: *Neues Jahrbuch für Mineralogie - Abhandlungen* 185.1, pp. 63–78. DOI: 10.1127/0077-7757/2008/0109. URL: http://dx.doi.org/10.1127/0077-7757/2008/0109.

Carulli, G. B. (2006). "Carta geologica del Friuli Venezia Giulia, scala 1: 150.000". In: *Regione Autonoma Friuli Venezia Giulia, Direzione Regionale Ambiente e Lavori Pubblici, Servizio Geologico Regionale*.

Castellarin, A., Ll Cantelli, A. M. Fesce, J. L. Mercier, V. Picotti, Gian Andrea Pini, G. Prosser, and L. Selli (1992). "Alpine compressional tectonics in the Southern Alps. Relationships with the N-Apennines". In: *Annales tectonicae*. Vol. 6. 1, pp. 62–94.

Cerny, I. (1989a). "Current prospecting strategy for carbonate-hosted Pb-Zn mineralizations at Bleiberg-Kreuth (Austria)". In: *Economic Geology* 84, pp. 1430–1435. DOI: 10.2113/gsecongeo.84.5.1430.

Cerny, I. (1989b). "Die karbonatgebundenen Blei-Zink-Lagerstätten des alpinen und ausseralpinen Mesozoikums: Die Bedeutung ihrer Geologie, Stratigraphie und Faziesgebundenheit für Prospektion und Bewertung". In: *Archiv für Lagerstättenforschung der Geologischen Bundesanstalt* 11, pp. 5–125.

Cook, N. J. (1996). "Mineralogy of the sulphide deposits at Sulitjelma, northern Norway". In: *Ore Geology Reviews* 11.5, pp. 303–338.

Cook, N. J. and Stephen L. Chryssoulis (1990). "Concentrations of invisible gold in the common sulfides". In: *The Canadian Mineralogist* 28.1, pp. 1–16.

Cook, N. J., Cristiana L. Ciobanu, Joël Brugger, Barbara Etschmann, Daryl L. Howard, Martin D. de Jonge, Chris Ryan, and David Paterson (2012). "Determination of the oxidation state of Cu in substituted Cu-In-Fe-bearing sphalerite via μ-XANES spectroscopy". In: *American Mineralogist* 97.2-3, pp. 476–479.

Cook, N. J., Cristiana L. Ciobanu, A. Pring, W. Skinner, M. Shimizu, L. Danyushevsky, B. Saini-Eidukat, and F. Melcher (2009). "Trace and minor elements in sphalerite: A LA-ICPMS study". In: *Geochimica et Cosmochimica Acta* 73.16, pp. 4761–4791.

Cook, N. J., Cristiana L. Ciobanu, and Timothy Williams (2011). "The mineralogy and mineral chemistry of indium in sulphide deposits and implications for mineral processing". In: *Hydrometallurgy* 108.3-4, pp. 226–228.

Cook, N. J., Barbara Etschmann, Cristiana L. Ciobanu, Kalotina Geraki, Daryl L. Howard, Timothy Williams, Nick Rae, Allan Pring, Guorong Chen, Bernt Johannessen, et al. (2015). "Distribution and substitution mechanism of Ge in a Ge-(Fe)-bearing sphalerite". In: *Minerals* 5.2, pp. 117–132.

Cotta, B. v. (1863). "Ueber die Blei- und Zinkerzlagerstätten Kärnthens". In: *Berg- und Hüttenmännische Zeitung* 22, 9-12 and 33-35 and 41-44 and 53–55.

Craig, James R., David J. Vaughan, and Richard D. Hagni (1981). *Ore microscopy and ore petrography*. Vol. 406. Wiley New York.

Cugerone, Alexandre, Bénédicte Cenki-Tok, Alain Chauvet, Elisabeth Le Goff, Laurent Bailly, Olivier Alard, and Mael Allard (2018). "Relationships between the occurrence of accessory Ge-minerals and sphalerite in Variscan Pb-Zn deposits of the Bossost anticlinorium, French Pyrenean Axial Zone: Chemistry, microstructures and ore-deposit setting". In: *Ore Geology Reviews* 95, pp. 1–19.

Cugerone, Alexandre, Bénédicte Cenki-Tok, Emilien Oliot, Manuel Munoz, Fabrice Barou, Vincent Motto-Ros, and Elisabeth Le Goff (2020). "Redistribution of germanium during dynamic recrystallization of sphalerite". In: *Geology* 48.3, pp. 236–241.

De Marco, Stefano, Roberto Fantoni, Maurizio Ponton, and Paolo Scotti (2000). "Cave del Predil: la successione di Raibl". In: *Guida alle escursioni – Società Geologica Italiana. 80˚ Riunione Estiva, Trieste, 6-8 settembre 2000*. Ed. by G. B. Carulli. Edizioni Università di Trieste, pp. 102–111.

De Zanche, Vittorio, Piero Gianolla, and Guido Roghi (2000). "Carnian stratigraphy in the Raibl/Cave del Predil area (Julian Alps, Italy)". In: *Eclogae geol. Helv.* 93, pp. 331–347.

Di Benedetto, F., G. P. Bernardini, P. Costagliola, D. Plant, and D. J. Vaughan (2005). "Compositional zoning in sphalerite crystals". In: *American Mineralogist* 90.8-9, pp. 1384–1392.

Di Colbertaldo, D. (1948a). "Il giacimento piombo-zincifero di Raibl in Friuli (Italia)". In: *Mem. presented 18th Sess. Int. Geol. Congr., London*, pp. 103–112.

— (1948b). "Il giacimento piombo-zincifero di Raibl in Friuli (Italia)". In: *Mem. presented 18th Sess. Int. Geol. Congr., London*, pp. 1–149.

— (1950). "The lead and zinc deposits at Raibl in Friuli–The geology, paragenesis, and reservesof lead and zinc". In: *Rept. 18th Session,Inter. Geol. Cong., pt. VII, sect. F*. Ed. by K. C. Dunham, pp. 277–288.

— (1951). "Illustrazione del giacimento di Raibl". In: *Rendiconti della Società Mineralogica Italiana* 7, pp. 23–25.

— (1954). "Marcasite idiomorfa nel giacimento di Raibl". In: *Rendiconti della Società Mineralogica Italiana* 10, pp. 369–371.

Di Colbertaldo, D. and G. Feruglio (1963). "I minerali tubolari di Raibl". In: *Atti della Soc. Italiana de Scienze Naturalie del Museo Civico in Milano* 102, pp. 53–73.

Doglioni, Carlo (1988). "Examples of strike-slip tectonics on platform-basin margins". In: *Tectonophysics* 156.3-4, pp. 293–302.

Dolenec, Tadej, Janez Kušej, and Jože Pezdič (1983). "The isotopic composition of oxygen and carbon in lead and zinc deposits from northern Karavanke". In: *Mineral Deposits of the Alps and of the Alpine Epoch in Europe*. Springer, pp. 176–188.

Duran, Charley J., S.-J. Barnes, and John T. Corkery (2015). "Chalcophile and platinum-group element distribution in pyrites from the sulfide-rich pods of the Lac des Iles Pd deposits, Western Ontario, Canada: Implications for post-cumulus re-equilibration of the ore and the use of pyrite compositions in exploration". In: *Journal of Geochemical Exploration* 158, pp. 223–242.

Ebner, F., I. Cerny, R. Eichhorn, M. Gotzinger, Werner Paar, Walter Prochaska, and L. Weber (1999). "Mineral resources in the Eastern Alps and adjoining areas". In: *Mitteilungen Der Österreichischen Geologischen Gesellschaft* 92, pp. 157–184.

European Commission (2020). "Study on the EU's list of Critical Raw Materials – Final Report". In.

Fellet, Guido, Luca Marchiol, Gemini Delle Vedove, and Alessandro Peressotti (2011). "Application of biochar on mine tailings: Effects and perspectives for land reclamation". In: *Chemosphere* 83, pp. 1262–7. DOI: 10.1016/j.chemosphere.2011.03.053.

Fellet, Guido, Filip Pošćić, V. Casolo, and Luca Marchiol (2012). "Metallophytes and thallium hyperaccumulation at the former Raibl lead/zinc mining site (Julian Alps, Italy)". In: *Plant Biosystems - An International Journal Dealing with all Aspects of Plant Biology* 146, pp. 1–14. DOI: 10.1080/11263504.2012.703250.

Fleet, M. E. (1977). "Structural transformations in natural ZnS". In: *American Mineralogist* 62.5-6, pp. 540–546.

— (2006). "Phase equilibria at high temperatures". In: *Reviews in Mineralogy and Geochemistry* 61.1, pp. 365–419.

Fornaro, Mauro (1985). "Die Gebirgsschlagbekämpfung im Bergwerk Raibl: Die durchgeführten Untersuchungen, die gesammelten Befahrungen und die heutigen Studien". In: *Geotechnik und Sicherheit im Bergbau - Bergschlagforschung: Seminar in Bad Bleiberg am 7. und 8. Juni 1984*, pp. 59–82.

Fowler, Anthony D. and Ivan L'Heureux (1996). "Self-organized banded sphalerite and branching galena in the Pine Point ore deposit, Northwest Territories". In: *The Canadian Mineralogist* 34.6, pp. 1211–1222.

Frangipani, E. (2013). "La miniera di Raibl e le ultime fasi del processo idrotermale". In: *Atti Mus. Civ. St. Nat. Trieste* 7-15.

Frenzel, Max, Tamino Hirsch, and Jens Gutzmer (2016). "Gallium, germanium, indium, and other trace and minor elements in sphalerite as a function of deposit type—A meta-analysis". In: *Ore Geology Reviews* 76, pp. 52–78.

— (2017). "Corrigendum to "Gallium, germanium, indium and other trace and minor elements in sphalerite as a function of deposit type–A meta-analysis"[Ore Geol. Rev. 76 (2016) 52–78]". In: *Ore Geology Reviews* 1.81, p. 400.

Froitzheim, Nikolaus, Dušan Plašienka, and Ralf Schuster (2008). "The Geology of Central Europe". In: ed. by Tom McCann. London: Geological Society. Chap. Alpine tectonics of the Alps and Western Carpathians, pp. 1141–1232.

George, Luke L., N. J. Cook, and Cristiana L. Ciobanu (2016). "Partitioning of trace elements in co-crystallized sphalerite–galena–chalcopyrite hydrothermal ores". In: *Ore Geology Reviews* 77, pp. 97–116.

George, Luke L., N. J. Cook, Cristiana L. Ciobanu, and Benjamin P. Wade (2015). "Trace and minor elements in galena: A reconnaissance LA-ICP-MS study". In: *American Mineralogist* 100.2-3, pp. 548–569.

Göbl, W. (1903). *Geologisch-bergmännische Karten Mit Profilen Von Raibl Nebst Bildern Von Den Blei- Und Zinklagerstätten In Raibl*. K.K.Ackerbauministerium.

Goldschmidt, Victor Moritz (1954). *Geochemistry*. Vol. 78. 2. LWW.

Goni, J. and G. Rémond (1969). "Localization and distribution of impurities in blende by cathodoluminescence". In: *Mineralogical Magazine* 37.286, pp. 153–155.

Gunn, Gus (2014). *Critical metals handbook*. John Wiley & Sons.

Hegemann, F. (1960). "Über extrusiv-sedimentäre Erzlagerstätten der Ostalpen, II. Teil: Blei-Zink-Lagerstätten". In: *Erzmetall, 12*, pp. 122–127.

Hein, U. F. and H.-J. Schneider (1983). "Fluorine anomalies accompanying the alpine Pb-Zn deposits compared to the geochemistry of their fluorites". In: *Mineral Deposits of the Alps and of the Alpine Epoch in Europe*. Springer, pp. 198–212.

Henjes-Kunst, Elisabeth (2014). "The Pb-Zn deposits in the Drau Range (Eastern Alps, Austria/Slovenia): a multi-analytical research approach for investigation of the ore-forming mechanisms". PhD thesis. University of Leoben.

Herzig, Peter M. and Mark D. Hannington (1995). "Polymetallic massive sulfides at the modern seafloor a review". In: *Ore Geology Reviews* 10.2, pp. 95–115.

Hill, Gregg S., Neil Rowlands, and James Finch (1985). "Correlation between color and iron content in Pine Point sphalerites". In: *Economic Geology* 80.7, pp. 2035–2037.

Höll, R., M. Kling, and E. Schroll (2007). "Metallogenesis of germanium—A review". In: *Ore Geology Reviews* 30.3-4, pp. 145–180.

Hu, Yusi, Chen Wei, Lin Ye, Zhilong Huang, Leonid Danyushevsky, and Haoyu Wang (2021). "LA-ICP-MS sphalerite and galena trace element chemistry and mineralization-style fingerprinting for carbonate-hosted Pb-Zn deposits: Perspective from early Devonian Huodehong deposit in Yunnan, South China". In: *Ore Geology Reviews* 136, p. 104253.

Huston, David L., Soey H. Sie, Gary F. Suter, David R. Cooke, and Ross A. Both (1995). "Trace elements in sulfide minerals from eastern Australian volcanic-hosted massive sulfide deposits; Part I, Proton microprobe analyses of pyrite, chalcopyrite, and spha-

lerite, and Part II, Selenium levels in pyrite; comparison with delta 34 S values and implications for the source of sulfur in volcanogenic hydrothermal systems". In: *Economic Geology* 90.5, pp. 1167–1196.

Jadoul, Flavio, Alda Nicora, Andrea Ortenzi, and Claudio Pohar (2002). "Ladinian stratigraphy and paleogeography of the Southern Val Canale (Pontebbano-Tarvisiano, Julian Alps, Italy)". In: *Memorie della Societa Geologica Italiana* 57.1, pp. 29–43.

Jicha, H. L. (1951). "Alpine lead-zinc ores of Europe". In: *Economic Geology* 46.7, pp. 707–730.

Johan, Z. (1988). "Indium and germanium in the structure of sphalerite: an example of coupled substitution with copper". In: *Mineralogy and Petrology* 39.3, pp. 211–229.

Katsev, Sergei and Ivan L'Heureux (2001). "Two-dimensional model of banding pattern formation in minerals by means of coarsening waves: Mississippi Valley-type sphalerite". In: *Physics Letters A* 292.1-2, pp. 66–74.

Katsev, Sergei, Ivan L'Heureux, and Anthony D. Fowler (2001). "Mechanism and duration of banding in Mississippi Valley-type sphalerite". In: *Geophysical Research Letters* 28.24, pp. 4643–4646.

Kojima, Shoji and Asahiko Sugaki (1984). "Phase relations in the central portion of the Cu-Fe-Zn-S system between 800° and 500° C". In: *Mineralogical Journal* 12.1, pp. 15–28.

Köppel, Viktor (1983). "Summary of lead isotope data from ore deposits of the Eastern and Southern Alps: some metallogenetic and geotectonic implications". In: *Mineral deposits of the Alps and of the Alpine Epoch in Europe.* Springer, pp. 162–168.

Köppel, Viktor and E. Schroll (1985). "Herkunft des Pb der triassischen Pb-Zn-Vererzungen in den Ost-und Südalpen, Resultate bleiisotopengeochemischer Untersuchungen". In: *Archiv für Lagerstättenforschung der Geologischen Bundesanstalt* 6, pp. 215–22.

Kossmat, F. (1903). "Umgebung von Raibl (Kärnten)". In: *Montan-Zeitung für Österreich-Ungarn, die Balkanländer und das Deutsche Reich* 11, pp. 355–358.

Kraus, M. (1913). *Das staatliche Blei-Zinkerz-Bergbauterrain bei Raibl in Kärnten.* Special. Vol. LXI. Berg-und Hüttenmännischen Jahrbuch 1 and 2. Wien: Manzsche k.u.k. Hof Verlags und Universitäts Buchhandlung.

Kubo, Tomohiro, Takayuki Nakato, and Etsuo Uchida (1992). "An experimental study on partitioning of Zn, Fe, Mn and Cd between sphalerite and aqueous chloride solution". In: *Shigen-Chishitsu* 42.235, pp. 301–309.

Kucha, H., E. Schroll, Johann G. Raith, and Stan Halas (2010). "Microbial sphalerite formation in carbonate-hosted Zn-Pb ores, Bleiberg, Austria: micro-to nanotextural and sulfur isotope evidence". In: *Economic Geology* 105.5, pp. 1005–1023.

Kucha, H., E. Schroll, and E. F. Stumpfl (2001). "Direct evidence for bacterial sulphur reduction in Bleiberg-type deposits". In: *Mineral Deposits at the Beginning of the 21st Century.* CRC Press, pp. 149–152.

Kuhlemann, Joachim and S. Zeeh (1995). "Sphalerite stratigraphy and trace element composition of east Alpine Pb-Zn deposits (Drau Range, Austria-Slovenia)". In: *Economic Geology* 90.7, pp. 2073–2080.

Kullerud, Gunnar (1953). "The FeS-ZnS system, a geological thermometer". In: *Norsk Geologisk Tidsskrift* 32, pp. 61–147.

Laetsch, T. and R. Downs (2006). *Software For Identification and Refinement of Cell Parameters From Powder Diffraction Data of Minerals Using the RRUFF Project and American Mineralogist Crystal Structure Databases.* Abstracts from the 19th General Meeting of the International Mineralogical Association, Kobe, Japan. Software.

Lange, Ian M., Warren J. Nokleberg, Joseph T. Plahuta, H. Roy Krouse, and Bruce R. Doe (1985). "Geologic setting, petrology, and geochemistry of stratiform sphalerite-galena-barite deposits, Red Dog Creek and Drenchwater Creek areas, northwestern Brooks Range, Alaska". In: *Economic Geology* 80.7, pp. 1896–1926.

Larter, R. C. L., A. J. Boyce, and M. J. Russell (1981). "Hydrothermal pyrite chimneys from the Ballynoe baryte deposit, Silvermines, County Tipperary, Ireland". In: *Mineralium Deposita* 16, pp. 309–317.

Lausi, D. and T. Cusma Velari (1986). "Caryological and morphological investigations on a new zinc violet (Cave del Predil, Western Julian Alps, NE-Italy)". In: *Studia Geobotanica* 6, pp. 123–129.

Leach, D. L., T. Bechstädt, M. Boni, and S. Zeeh (2003). "Europe's major base metal deposits". In: ed. by J. G. Kelly, C. J. Andrew, J. H. Ashton, M. B. Boland, G. Earls, and L. Fusciardi. Dublin: Irish Association for Economic Geology. Chap. Triassic-hosted MVT Zn-Pb ores of Poland, Austria, Slovenia and Italy, pp. 169–213.

Leach, D. L., Dwight Bradley, Michael T. Lewchuk, David T. Symons, Ghislain de Marsily, and Joyce Brannon (2001). "Mississippi Valley-type lead–zinc deposits through geological time: implications from recent age-dating research". In: *Mineralium Deposita* 36.8, pp. 711–740.

Leach, D. L., Dwight C. Bradley, David Huston, Sergei A. Pisarevsky, Ryan D. Taylor, and Steven J. Gardoll (2010a). "Sediment-hosted lead-zinc deposits in Earth history". In: *Economic Geology* 105.3, pp. 593–625.

Leach, D. L. and D. F. Sangster (1993). "Mineral Deposit Modeling". In: ed. by Sinclair W. D. Thorp R. I. Kirkham R.V. and J. M. Duke. Special Paper 40. Geological Association of Canada. Chap. Mississippi Valley-type lead-zinc deposits, pp. 289–314.

Leach, D. L. and Ryan D. Taylor (2009). "Mississippi Valley-type lead-zinc deposit model". In: *US Geological Survey Open-File Report* 1213.5.

Leach, D. L., Ryan D. Taylor, David L. Fey, Sharon F. Diehl, and Richard W. Saltus (2010b). "A deposit model for Mississippi Valley-type lead-zinc ores, chapter A". In: *Mineral deposit models for resource assessment: USGS, Scientific Investigations Report 2010–5070–A.*

Leach, D. L., John B. Viets, Nora Foley-Ayuso, and Douglas P. Klein (1995). "Mississippi Valley-Type Pb-Zn deposits (Models 32a, b; Briskey, 1986 a, b)". In: *Preliminary compilation of descriptive geoenvironmental mineral deposit models: US Government Consulting Group, open file report*, pp. 95–831.

Li, Zhenli, Lin Ye, Yusi Hu, Chen Wei, Zhilong Huang, Yulong Yang, and Leonid Danyushevsky (2020). "Trace elements in sulfides from the Maozu Pb-Zn deposit, Yunnan Province, China: Implications for trace-element incorporation mechanisms and ore genesis". In: *American Mineralogist* 105.11, pp. 1734–1751.

Licht, C., L. T. Peiró, and G. Villalba (2015). "Global substance flow analysis of gallium, germanium, and indium: quantification of extraction, uses, and dissipative losses within their anthropogenic cycles". In: *Journal of Industrial Ecology* 19.5, pp. 890–903.

Lieberman, Henry M. (1978). "Das Raibler Becken: eine paläogeographische Rekonstruktion aus dem südalpinen Karn von Raibl (Cave del Predil, Italien)". In: *Geologisch Paläontologische Mitteilungen Innsbruck* 7.4, pp. 7–20.

Liu, Shan, Yu Zhang, Guoliang Ai, Xilin Xue, Hongbin Li, Sajjad Ahmad Shah, Naihui Wang, and Xi Chen (2022). "LA-ICP-MS trace element geochemistry of sphalerite:

Metallogenic constraints on the Qingshuitang Pb–Zn deposit in the Qinhang Ore Belt, South China". In: *Ore Geology Reviews* 141, p. 104659.

Luo, Kai, Alexandre Cugerone, Mei-Fu Zhou, Jia-Xi Zhou, Guo-Tao Sun, Jing Xu, Kang-Jian He, and Mao-Da Lu (2022). "Germanium enrichment in sphalerite with acicular and euhedral textures: an example from the Zhulingou carbonate-hosted Zn (-Ge) deposit, South China". In: *Mineralium Deposita* 57.8, pp. 1343–1365.

Maslennikov, V. V., S. P. Maslennikova, R. R. Large, and L. V. Danyushevsky (2009). "Study of trace element zonation in vent chimneys from the Silurian Yaman-Kasy volcanic-hosted massive sulfide deposit (Southern Urals, Russia) using laser ablation-inductively coupled plasma mass spectrometry (LA-ICPMS)". In: *Economic Geology* 104.8, pp. 1111–1141.

Melcher, F. and P. Onuk (2019). "Potential of critical high-technology metals in eastern alpine base metal sulfide ores". In: *BHM Berg-und Hüttenmännische Monatshefte* 164.2, pp. 71–76.

Moh, Günter H. and Anton Jager (1979). "Phasengleichgewichte des Systems Ge-Pb-Zn-S in Relation zu Germaniumgehalten alpiner Pb-Zn-Lagerstätten". In: *Verhandlungen der Geologischen Bundesanstalt* 3, pp. 437–440.

Möller, Peter (1987). "Correlation of homogenization temperatures of accessory minerals from sphalerite-bearing deposits and Ga/Ge model temperatures". In: *Chemical Geology* 61.1-4, pp. 153–159.

Morlot, Adolphe Charles (1850). "Ueber die geologischen Verhältnisse von Raibl". In: *Jahrbuch der k.k. Geologischen Reichsanstalt* 1, pp. 255–267.

Muchez, Philippe, Wouter Heijlen, David Banks, Derek Blundell, Maria Boni, and Fidel Grandia (2005). "7: Extensional tectonics and the timing and formation of basin-hosted deposits in Europe". In: *Ore Geology Reviews* 27.1-4, pp. 241–267.

Omenetto, P. (1980). "Significant ore fabric relationships in the lead, zinc, fluorite and barite deposits of the Triassic province (Italian Southern Alps)". In: *Annales de la Société géologique de Belgique*.

Onuk, P. (2018). "High-tech metal potential of sphalerite from Eastern Alpine lead-zinc deposits and development of a matrix-matched sphalerite (ZnS) calibration material (MUL-ZnS-1) for calibration of in situ trace element measurements by laser ablation inductively coupled plasma mass spectrometry (LA-ICP-MS)". PhD thesis. University of Leoben.

Onuk, P., Frank Melcher, Regina Mertz-Kraus, Hans-Eike Gäbler, and Simon Goldmann (2017). "Development of a matrix-matched sphalerite reference material (MUL-ZnS-1) for calibration of in situ trace element measurements by laser ablation-inductively coupled plasma-mass spectrometry". In: *Geostandards and Geoanalytical Research* 41.2, pp. 263–272.

Paradis, S. (2015). "Indium, germanium and gallium in volcanic- and sediment-hosted base-metal sulphide deposits". In: *Symposium on Strategic and Critical Materials Proceedings, November 13-14, 2015, Victoria, British Columbia*. Ed. by G. J. Simandl and M. Neetz. British Columbia Geological Survey Paper 2015 3. British Columbia Ministry of Energy and Mines, pp. 23–29.

Paradis, S., P. Hannigan, and K. Dewing (2007a). "Mississipi valley-type lead-zinc deposits (MVT)". In: *Mineral deposits of Canada, Geological Survey of Canada*, pp. 1–15.

Paradis, S., Peter Hannigan, and Keith Dewing (2007b). "Mississippi Valley-type lead-zinc deposits". In: *Mineral deposits of Canada: A synthesis of major deposit-types, district metallogeny, the evolution of geological provinces, and exploration methods:*

Geological Association of Canada, Mineral Deposits Division, Special Publication 5, pp. 185–203.

Patel, Madhav and Athanasios K. Karamalidis (2021). "Germanium: A review of its US demand, uses, resources, chemistry, and separation technologies". In: *Separation and Purification Technology* 275, p. 118981.

Paton, Chad, John Hellstrom, Bence Paul, Jon Woodhead, and Janet Hergt (2011). "Iolite: Freeware for the visualisation and processing of mass spectrometric data". In: *Journal of Analytical Atomic Spectrometry* 26.12, pp. 2508–2518.

Petrini, Riccardo, Rosa Cidu, and Francesca F. Slejko (2016). "Thallium Contamination in the Raibl Mine Site Stream Drainage System (Eastern Alps, Italy)". In: *Mine Water and the Environment* 35.1, pp. 55–63. ISSN: 1025-9112. DOI: 10.1007/s10230-015-0346-4.

Pfaff, Katharina, Alan Koenig, Thomas Wenzel, Ian Ridley, Ludwig H. Hildebrandt, D. L. Leach, and Gregor Markl (2011). "Trace and minor element variations and sulfur isotopes in crystalline and colloform ZnS: Incorporation mechanisms and implications for their genesis". In: *Chemical Geology* 286.3-4, pp. 118–134.

Pimminger, M., M. Grasserbauer, E. Schroll, and I. Cerny (1985). "Anwendung der Ionenstrahlmikroanalyse zur geochemischen Charakterisierung von Zinkblenden". In: *Arch Lagerstättenforsch Geol Bundesanst Wien* 6, pp. 209–214.

Posepny, F. (1873). "Die Blei- und Galmei-Erzlagerstätten von Raibl in Kärnten". In: *Jahrbuch der k.k. Geologischen Reichsanstalt* 23, pp. 317–424.

— (1875). "Zur Entwicklungsgeschichte des Raibler Bergbaues". In: *Österreichische Zeitschrift für Berg- und Hüttenwesen* 23, p. 306.

Pošepny, F. (1887). "Die sogenannten Röhrenerze von Raibl". In: *Verh. Geol. Reichanstalt* 5, pp. 84–87.

Potocnik Krajnc, Barbara (2021). "Trace element composition of sphalerite from the Mezica Pb-Zn mine". MA thesis. University of Ljubljana.

Pring, Allan, Benjamin Wade, Aoife McFadden, Claire E. Lenehan, and N. J. Cook (2020). "Coupled substitutions of minor and trace elements in co-existing sphalerite and wurtzite". In: *Minerals* 10.2, p. 147.

Pucher, Richard Oskar Friedrich (2016). "Die 25. Abteilung des k.u.k. Kriegsministeriums und die ihr unterstehenden kriegswirtschaftlichen Berg- und Hüttenwerke". PhD thesis. Historisch-Kulturwissenschaftliche Fakultät , Universität Wien.

Rager, Helmut, Georg Amthauer, Manfred Bernroider, and Kay Schurmann (1996). "Colour, crystal chemistry, and mineral association of a green sphalerite from Steinperf, Dill Syncline, FRG". In: *European Journal of Mineralogy* 8.5, pp. 1191–1198.

Sangster, D. F. (1996). "Mississippi Valley-type lead-zinc". In: ed. by O. R. Eckstrand, W. D. Sinclair, and R. I. Thorpe. 8. Geological Survey of Canada. Chap. Geology of Canada, pp. 253–261.

Schirmer, Thomas, Wilfried Ließmann, Chandra Macauley, and Peter Felfer (2020). "Indium and antimony distribution in a sphalerite from the "burgstaetter gangzug" of the upper harz mountains Pb-Zn mineralization". In: *Minerals* 10.9, p. 791.

Schmid, S. M., H. R. Aebli, F. Heller, and A. Zingg (1989). "The role of the Periadriatic Line in the tectonic evolution of the Alps". In: *Geological Society, London, Special Publications* 45.1, pp. 153–171.

Schmid, S. M., Daniel Bernoulli, Bernhard Fügenschuh, Liviu Matenco, Senecio Schefer, Ralf Schuster, Matthias Tischler, and Kamil Ustaszewski (2008). "The Alpine-Carpathian-

Dinaridic orogenic system: correlation and evolution of tectonic units". In: *Swiss Journal of Geosciences* 101.1, pp. 139–183.

Schmid, S. M., Bernhard Fügenschuh, Eduard Kissling, and Ralf Schuster (2004). "Tectonic map and overall architecture of the Alpine orogen". In: *Eclogae Geologicae Helvetiae* 97.1, pp. 93–117.

Schmid, S. M., Bernhard Fügenschuh, Alexandre Kounov, Liviu Maţenco, Peter Nievergelt, Roland Oberhänsli, Jan Pleuger, Senecio Schefer, Ralf Schuster, Bruno Tomljenović, Kamil Ustaszewski, and Douwe J. J. van Hinsbergen (2020). "Tectonic units of the Alpine collision zone between Eastern Alps and western Turkey". In: *Gondwana Research* 78, pp. 308–374.

Schroll, E. (1953a). *Über Minerale und Spurenelemente, Vererzung und Entstehung der Blei-Zink-Lagerstätte Bleiberg-Kreuth/Kärnten in Österreich*. Special. Vol. 2. Östereichische Mineralogische Gesellschaft.

— (1953b). "Über Unterschiede im Spurengehalt bei Wurtziten, Schalenblenden und Zinkblenden". In: *Sitzungsberichte der Akademie der Wissenschaften mathematisch-naturwissenschaftliche Klasse*. Vol. 162. Verlag der Österreichischen Akademie der Wissenschaften, Wien, pp. 305–332.

— (1954). *Ein Beitrag zur geochemischen Analyse ostalpiner Blei-Zink-Erze: Teil 1*. Sonderheft. Vol. 3. Mitt. Österr. Min. Ges. Wien: Östereichische Mineralogische Gesellschaft.

— (1955). "Über das Vorkommen einiger Spurenmetalle in Blei-Zink-Erzen der ostalpinen Metallprovinz". In: *Tschermaks mineralogische und petrographische Mitteilungen* 5.3, pp. 183–208.

— (1981). "REM-Untersuchungen an Schalenblenden: ein Beitrag zur As-und Tl-Führung von Sphaleriten". In: *Fortschritte der Mineralogie* 59.I-II, pp. 178–179.

— (1983). "Geochemical characterization of the Bleiberg type and other carbonate hosted lead-zinc mineralizations". In: *Mineral Deposits of the Alps and of the Alpine Epoch in Europe: Proceedings of the IV. ISMIDA Berchtesgaden, October 4–10, 1981*. Springer, pp. 189–197.

— (1996). "The Triassic Carbonate-Hosted Pb-Zn Mineralization in the Alps (Europe): The Genetic Position of Bleiberg Type Deposits". In: *Carbonate-Hosted Lead-Zinc Deposits: 75th Anniversary Volume*. Ed. by D. F. Sangster. Society of Economic Geologists, pp. 182–194. ISBN: 9781629490281. DOI: 10.5382/SP.04.11. URL: https://doi.org/10.5382/SP.04.11.

Schroll, E. (2005). "Alpine type Pb-Zn-deposits (APT) hosted by Triassic carbonates". In: *Mineral Deposit Research: Meeting the Global Challenge*. Springer, pp. 175–178.

Schroll, E. and W. Prochaska (2004). "Contribution to ore fluid chemistry of Bleiberg Pb-Zn deposit (Austria) and affilated deposits". In: *GEOCHIMICA ET COSMOCHIMICA ACTA* 68.11, A306.

Schroll, E. and Gerd Rantitsch (2005). "Sulphur isotope patterns from the Bleiberg deposit (Eastern Alps) and their implications for genetically affiliated lead–zinc deposits". In: *Mineralogy and Petrology* 84.1, pp. 1–18.

Schulz, O. (1959). "Studien an Zinkblenden im Bereich der erzführenden Raibler Schichten der Grube Max, Kreuth (Kärnten)". In: *Berg-u. Hüttenm. Mh., Jg. 104, H. 9*. Springer-Verlag Wien.

— (1964). "Mechanische Erzanlagerungsgefüge in den Pb-Zn-Lagerstätten Mezica - Mies (Jugoslawien) und Cave del Predil - Raibl (Italien)". In: *Berg- und Hüttenmännische Monatshefte* 109, pp. 385–389.

— (1970). "Vergleichende petrographische Untersuchungen an Karnischen Sedimenten der Julischen Alpen, Gailtaler Alpen und des Karwendels". In: *Verh Geol Bundesanst* 1970, pp. 165–229.

Schwartz, Michael O. (2000). "Cadmium in zinc deposits: economic geology of a polluting element". In: *International Geology Review* 42.5, pp. 445–469.

Shannon, Robert D. (1976). "Revised effective ionic radii and systematic studies of interatomic distances in halides and chalcogenides". In: *Acta crystallographica section A: crystal physics, diffraction, theoretical and general crystallography* 32.5, pp. 751–767.

Shimazaki, Hidehiko and Ei Horikoshi (1990). "Black ore chimney from the Hanaoka Kuroko deposits, Japan". In: *Mining Geology* 40.223, pp. 313–321.

Stoiber, Richard Edwin (1940). "Minor elements in sphalerite". In: *Economic Geology* 35.4, pp. 501–519.

Sverjensky, Dimitri A. (1986). "Genesis of Mississippi Valley-type lead-zinc deposits". In: *Annual Review of Earth and Planetary Sciences* 14, p. 177.

Tintori, Andrea (1992). "Fish taphonomy and Triassic anoxic basins from the Alps: a case history". In: *Rivista italiana di paleontologia e stratigrafia* 97.3-4, pp. 393–408.

Tornquist, Alexander (1931). "Die Vererzung der Zink-Bleierz-Lagerstätte von Raibl (Cave del Predil)". In: *Jahrbuch der Geologischen Bundesanstalt* 81, pp. 143–175.

Wagner, Thomas and N. J. Cook (1998). "Sphalerite remobilization during multistage hydrothermal mineralization events—examples from siderite-Pb-Zn-Cu-Sb veins, Rheinisches Schiefergebirge, Germany". In: *Mineralogy and Petrology* 63.3, pp. 223–241.

Wei, Chen, Lin Ye, Yusi Hu, Leonid Danyushevskiy, Zhenli Li, and Zhilong Huang (2019). "Distribution and occurrence of Ge and related trace elements in sphalerite from the Lehong carbonate-hosted Zn-Pb deposit, northeastern Yunnan, China: Insights from SEM and LA-ICP-MS studies". In: *Ore Geology Reviews* 115, p. 103175.

Wei, Taiyun and Viliam Simko (2021). *R package 'corrplot': Visualization of a Correlation Matrix.* (Version 0.92). URL: https://github.com/taiyun/corrplot.

Wilkinson, J. J., S. L. Eyre, and A. J. Boyce (2005). "Ore-forming processes in Irish-type carbonate-hosted Zn-Pb deposits: Evidence from mineralogy, chemistry, and isotopic composition of sulfides at the Lisheen mine". In: *Economic Geology* 100.1, pp. 63–86.

Wilson, S. A., W. I. Ridley, and A. E. Koenig (2002). "Development of sulfide calibration standards for the laser ablation inductively-coupled plasma mass spectrometry technique". In: *Journal of Analytical Atomic Spectrometry* 17.4, pp. 406–409.

Wright, Kate (2009). "The incorporation of cadmium, manganese and ferrous iron in sphalerite: insights from computer simulations". In: *The Canadian Mineralogist* 47.3, pp. 615–623.

Wright, Kate and Julian D. Gale (2010). "A first principles study of the distribution of iron in sphalerite". In: *Geochimica et Cosmochimica Acta* 74.12, pp. 3514–3520.

Ye, Lin, N. J. Cook, Cristiana L. Ciobanu, Liu Yuping, Zhang Qian, Liu Tiegeng, Gao Wei, Yang Yulong, and Leonid Danyushevskiy (2011). "Trace and minor elements in sphalerite from base metal deposits in South China: A LA-ICPMS study". In: *Ore Geology Reviews* 39.4, pp. 188–217.

Ye, Lin, ZhenLi Li, YuSi Hu, ZhiLong Huang, JiaXi Zhou, HaiFeng Fan, and Leonid Danyushevskiy (2016). "Trace elements in sulfide from the Tianbaoshan Pb-Zn deposit, Sichuan Province, China: A LA-ICPMS study". In: *Acta Petrologica Sinica* 32.11, pp. 3377–3393.

Yuan, Bo, Changqing Zhang, Hongjun Yu, Yaomin Yang, Yuexia Zhao, Chaocheng Zhu, Qingfeng Ding, Yubin Zhou, Jichao Yang, and Yue Xu (2018). "Element enrichment

characteristics: Insights from element geochemistry of sphalerite in Daliangzi Pb–Zn deposit, Sichuan, Southwest China". In: *Journal of Geochemical Exploration* 186, pp. 187–201.

Zeeh, S. and T. Bechstädt (1994). "Carbonate-hosted Pb-Zn mineralization at Bleiberg-Kreuth (Austria): Compilation of data and new aspects". In: *Sediment-Hosted Zn-Pb Ores*. Springer, pp. 271–296.

Zeeh, S., Joachim Kuhlemann, and Thilo Bechstädt (1998). "The classical Pb-Zn deposits of the Eastern Alps (Austria/Slovenia) revisited: MVT deposits resulting from gravity driven fluid flow in the Alpine realm". In: *Geologija* 41.1, pp. 257–273.

Zhuang, Liangliang, Yucai Song, Yingchao Liu, Mahmoud Fard, and Zengqian Hou (2019). "Major and trace elements and sulfur isotopes in two stages of sphalerite from the world-class Angouran Zn–Pb deposit, Iran: Implications for mineralization conditions and type". In: *Ore Geology Reviews* 109, pp. 184–200.

A. Mineral formulas

name	composition	abbreviation
anglesite	$PbSO_4$	Ang
anhydrite	$CaSO_4$	Anh
arsenopyrite	FeAsS	Apy
barite	$BaSO_4$	Brt
bianchite	$Zn(SO_4) \cdot 6H_2O$	
bornite	Cu_5FeS_4	Bn
calamine	smithsonite+hydrozincite+hemimorphite	
calcite	$CaCO_3$	Cal
celestine	$SrSO_4$	Clt
cerussite	$PbCO_3$	Cer
chalcopyrite	$CuFeS_2$	Cct
crocoite	$PbCr^{6+}O_4$	
dolomite	$CaMg(CO_3)_2$	Dol
fluorite	CaF_2	Fl
fluorapatite	$Ca_5[F|(PO_4)_3]$	
galena	PbS	Gn
geocronite	$Pb_{14}Sb_6S_{23}$	
goslarite	$ZnSO_4 \cdot 7H_2O$	
gypsum	$CaSO_4 \cdot 2H_2O$	Gp
hydrozincite	$Zn_5(CO_3)_2(OH)_6$	
hemimorphite	$Zn_4Si_2O_7(OH)_2 \cdot H_2O$	Hmp
jordanite	$Pb_{14}As_6S_{23}$	
limonite	mixture of iron-hydroxides and iron-oxides	Lm
malachite	$Cu_2(CO_3)(OH)_2$	Mlc
marcasite	FeS_2(orthorombic)	Mrc
melanterite	$Fe^{2+}(H_2O)6SO_4 \cdot H_2O$	
melnikovite	mixture of pyrite and marcasite	
pyrite	FeS_2(cubic)	Py
pyrrhotite	$Fe_{1-x}S$	Po
quartz	SiO_2	Qtz
smithsonite	$ZnCO_3$	Smt
sphalerite	ZnS	Sph
willemite	Zn_2SiO_4	
wulfenite	$Pb(MoO_4)$	

Table A.1.: Minerals mentioned in this study and their chemical formulas

B. Probability plots

B.1. Iron
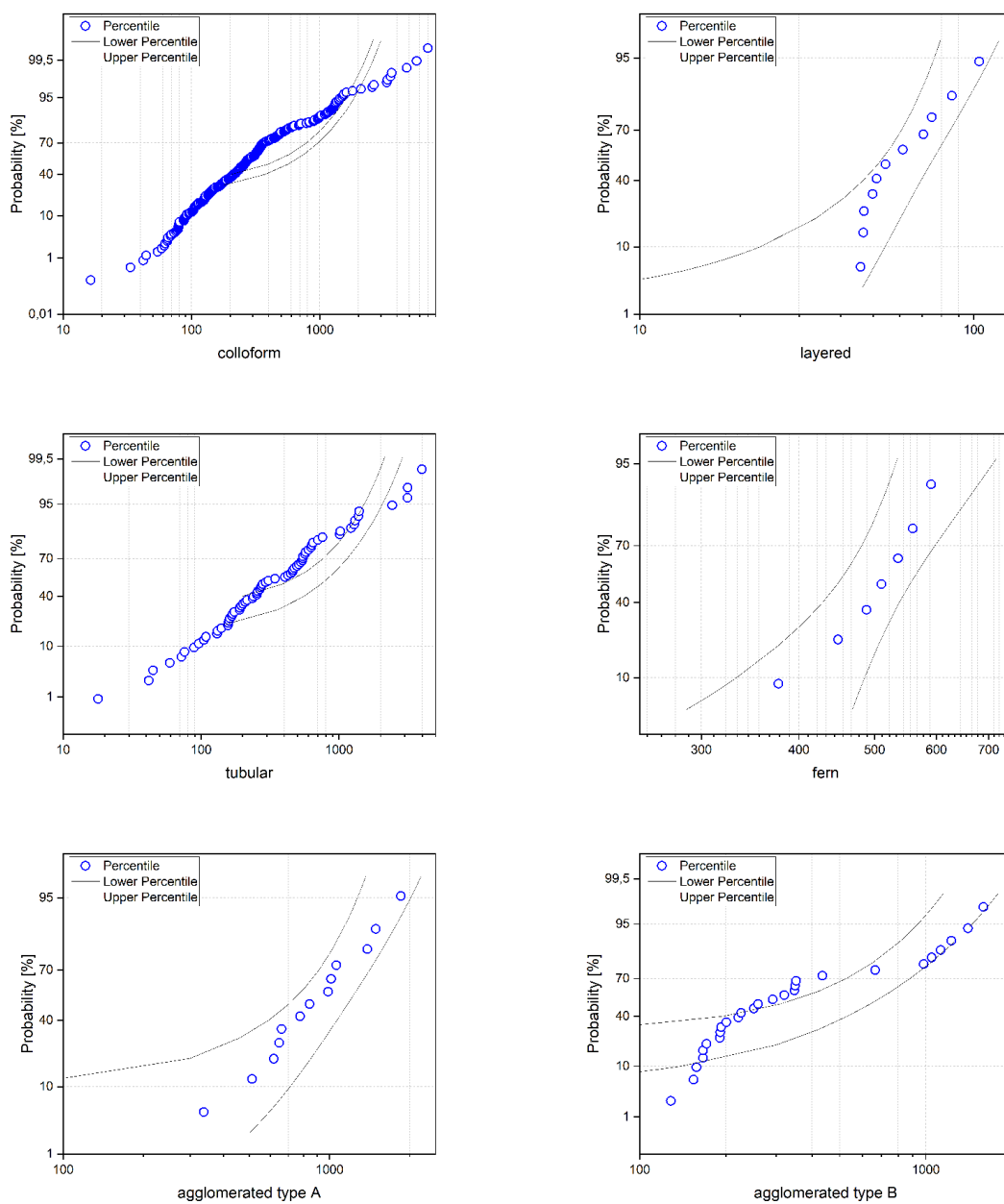
Figure B.1.: Probability plots for iron concentrations in sphalerite of different textural varieties; all values are given in $\mu g/g$

B.2. Germanium
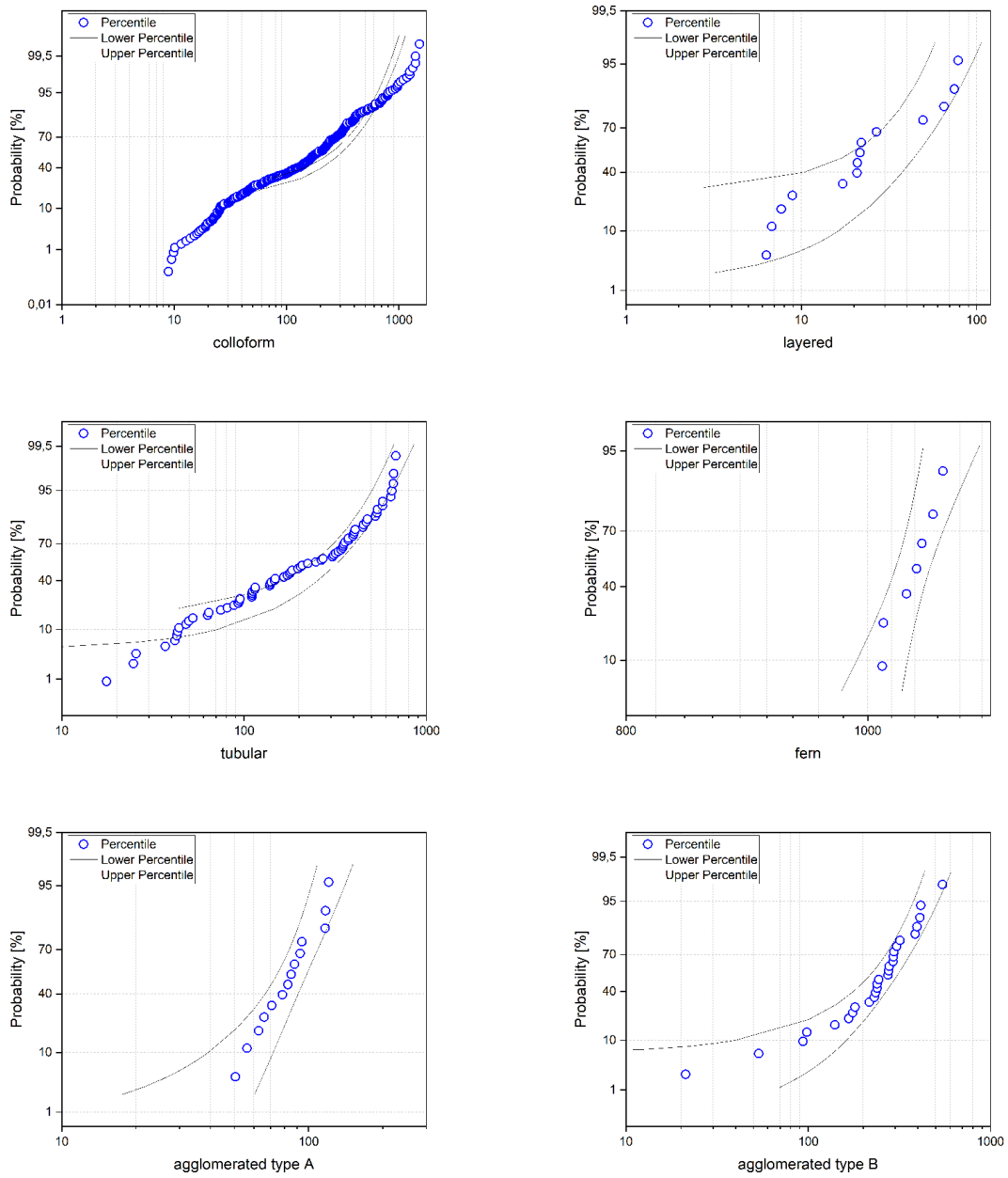
Figure B.2.: Probability plots for germanium concentrations in sphalerite of different textural varieties; all values are given in $\mu g/g$

B.3. Arsenic
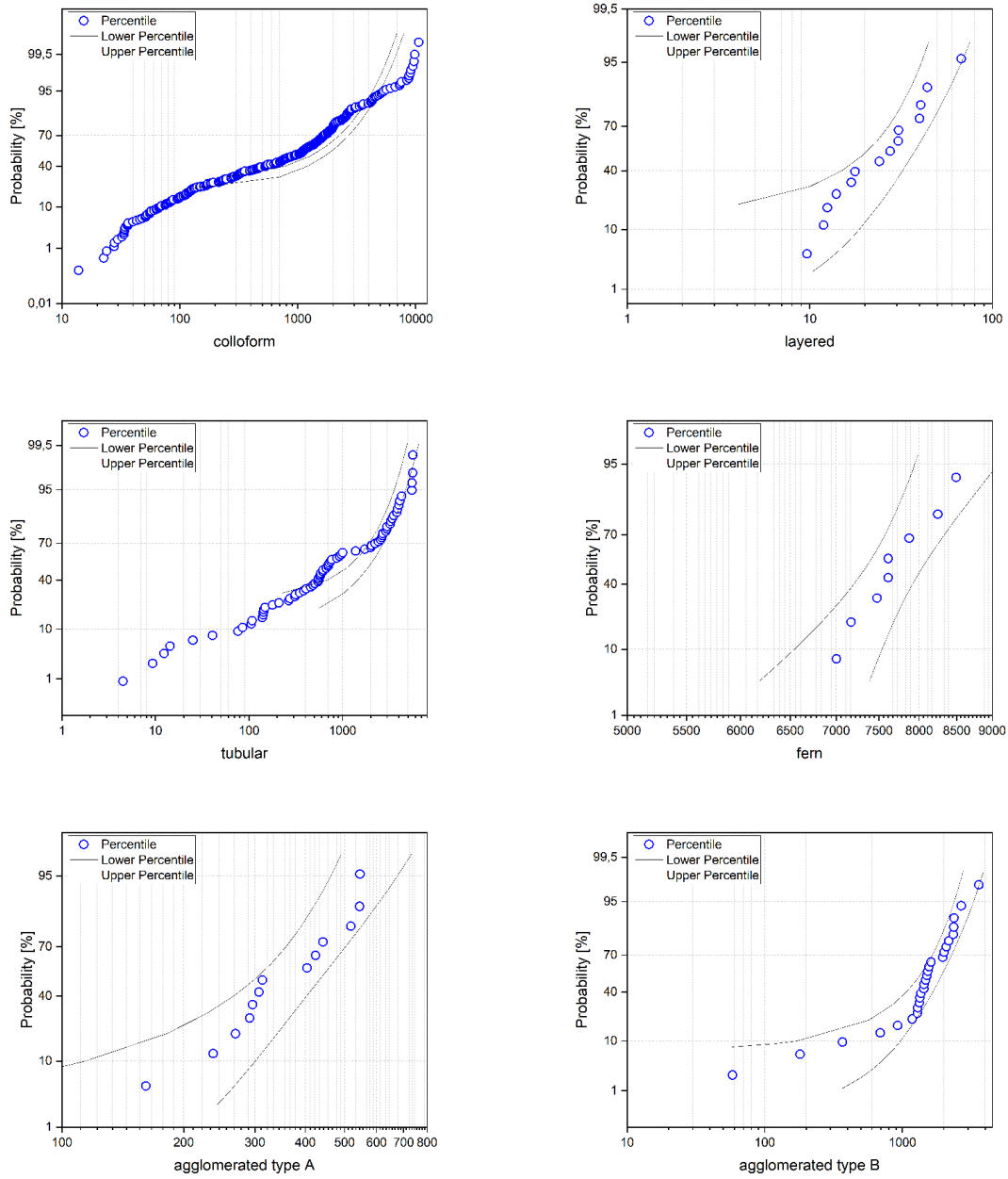
Figure B.3.: Probability plots for arsenic concentrations in sphalerite of different textural varieties; all values are given in $\mu g/g$

124
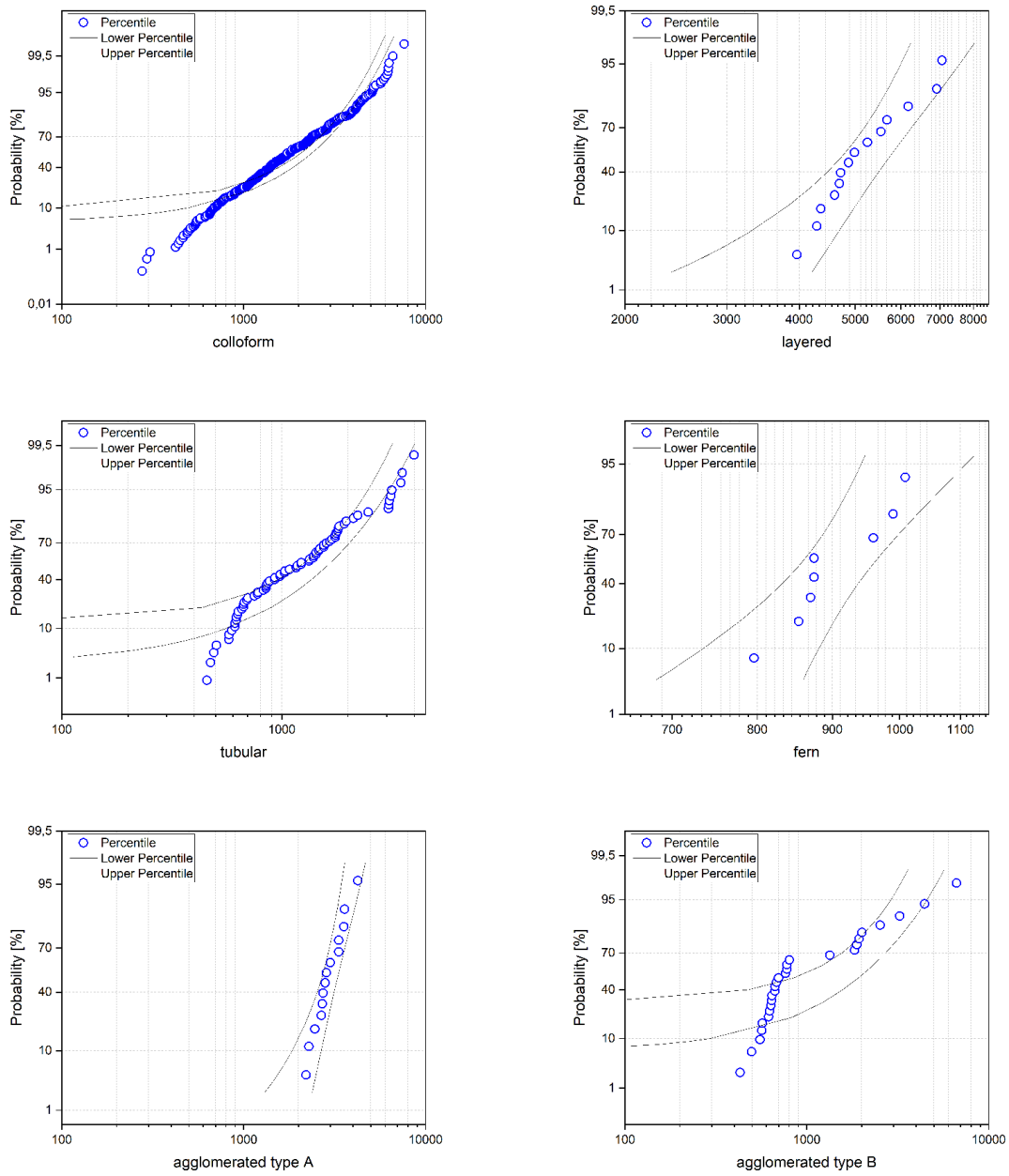
B.4. Cadmium

Figure B.4.: Probability plots for cadmium concentrations in sphalerite of different textural varieties; all values are given in $\mu g/g$

125
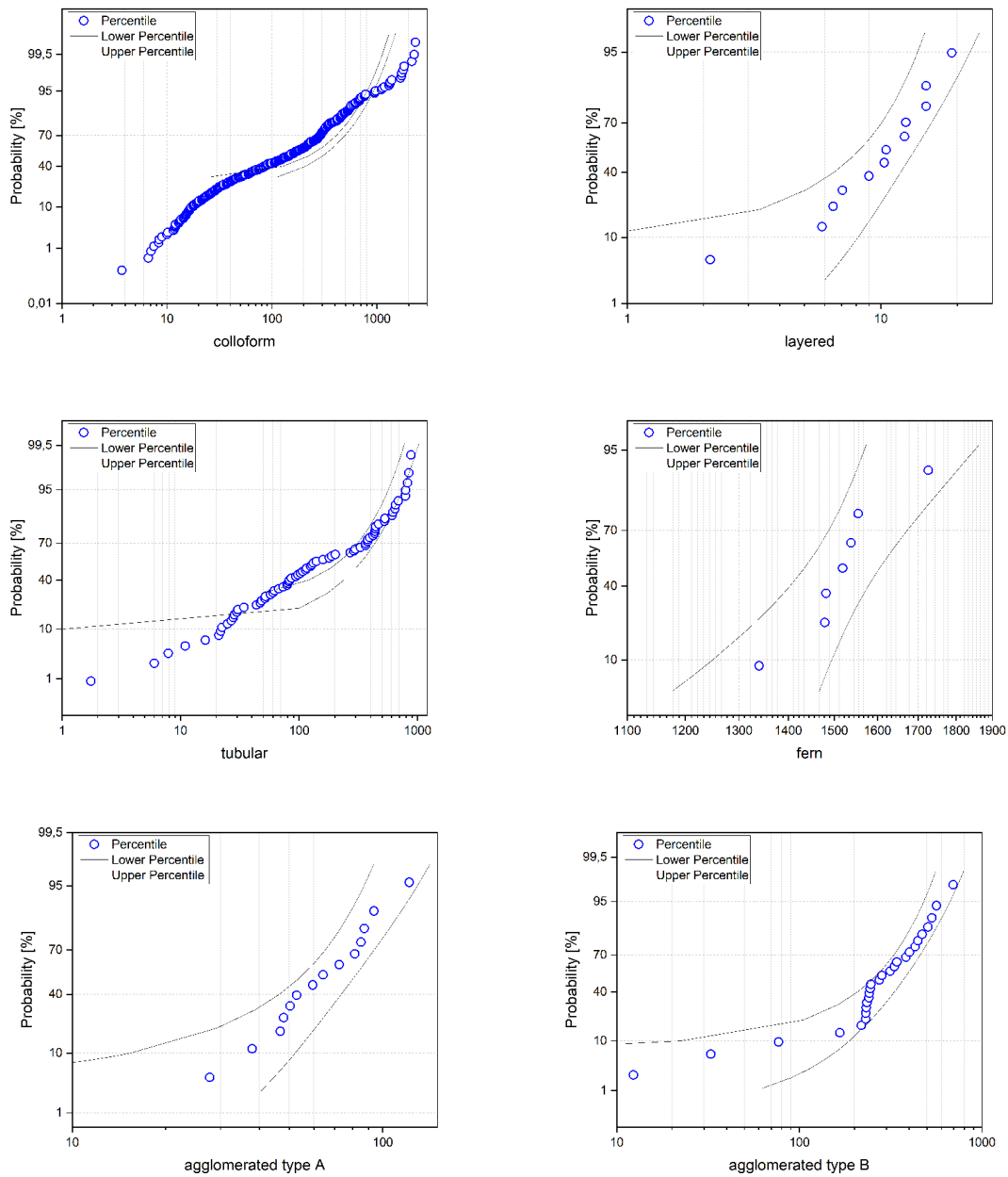
B.5. Thallium

Figure B.5.: Probability plots for thallium concentrations in sphalerite of different textural varieties; all values are given in $\mu g/g$

B.6. Lead
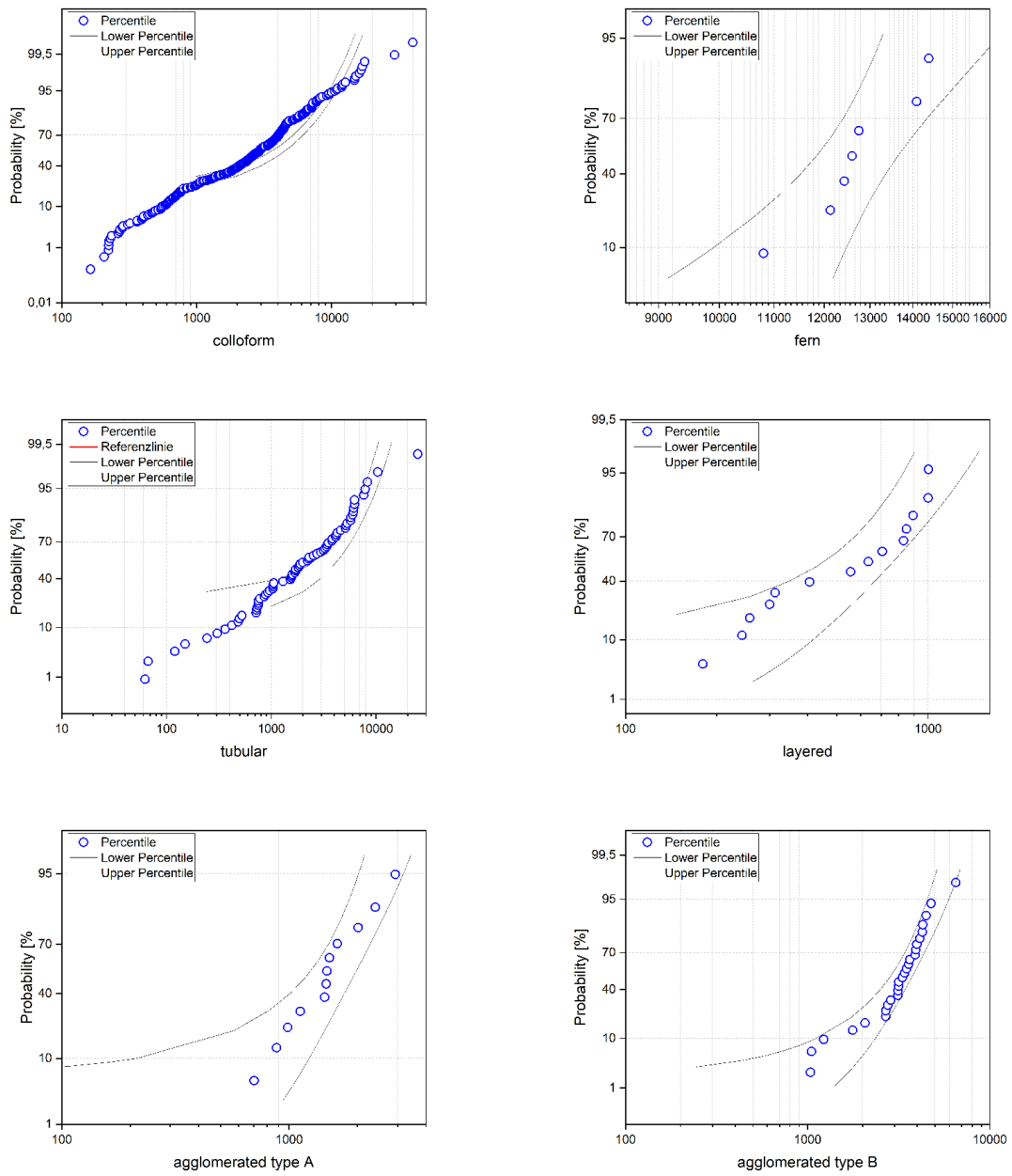
Figure B.6.: Probability plots for lead concentrations in sphalerite of different textural varieties; all values are given in $\mu g/g$

C. Correlation matrix

	Mn	Fe	Ge	As	Ag	Cd	Sb	Hg	Tl	Pb
Mn	1.00	0.65	0.84	0.85	0.07	-0.66	0.18	0.13	0.86	0.81
Fe	0.65	1.00	0.69	0.73	-0.04	-0.54	0.03	0.07	0.73	0.62
Ge	0.84	0.69	1.00	0.95	0.02	-0.70	0.10	0.18	0.94	0.90
As	0.85	0.73	0.95	1.00	0.01	-0.68	0.09	0.09	0.98	0.94
Ag	0.07	-0.04	0.02	0.01	1.00	0.13	0.30	-0.02	-0.01	0.05
Cd	-0.66	-0.54	-0.70	-0.68	0.13	1.00	0.28	-0.09	-0.70	-0.55
Sb	0.18	0.03	0.10	0.09	0.30	0.28	1.00	0.18	0.07	0.15
Hg	0.13	0.07	0.18	0.09	-0.02	-0.09	0.18	1.00	0.06	0.04
Tl	0.86	0.73	0.94	0.98	-0.01	-0.70	0.07	0.06	1.00	0.92
Pb	0.81	0.62	0.90	0.94	0.05	-0.55	0.15	0.04	0.92	1.00

Table C.1.: Correlation matrix